Studies on Thin Films of Carbon Based Nanomaterials

THESIS

Submitted in partial fulfilment

of the requirements for the degree of

DOCTOR OF PHILOSOPHY

by

MONIKA POONIA

Under the supervision of

Prof. R. K. Gupta

BITS Pilani

Pilani | Dubai | Goa | Hyderabad

BIRLA INSTITUTE OF TECHNOLOGY & SCIENCE, PILANI

2016

BIRLA INSTITUTE OF TECHNOLOGY &
SCIENCE, PILANI – 333 031 (RAJASTHAN)
INDIA

CERTIFICATE

This is to certify that the work reported in the Ph.D. thesis entitled as **"Studies on Thin Films of Carbon Based Nanomaterials"**, submitted by **Monika Poonia**, ID.No. **2011PHXF028P** at Physics Department, BITS–Pilani, Pilani Campus for the award of the degree of Doctor of Philosophy (Ph.D.), is a bonafide record of her original work carried out under my supervision. This work has not been submitted elsewhere for any other degree or diploma.

Signature: ....

Dr. R. K. Gupta

Associate Professor,
Department of Physics,
BITS–Pilani, Pilani Campus

Date: ....

Dedicated to My Parents

Acknowledgements

Firstly, I would like to express my sincere gratitude to my supervisor Prof. R K Gupta for his continuous support during my research work. His guidance helped me in all the time of research and writing of this thesis. I have been continually inspired by his deep knowledge and understanding of physics. Moreover, I deeply appreciate the encouragement I have received during the past five years. I could not have imagined having a better mentor for my Ph.D. work. I am also grateful to Prof. V. Manjuladevi for her invaluable guidance, her constant support and motivation throughout my Ph.D. work.

I deeply acknowledge the members of my Doctoral Advisory Committee, Prof. Debashis Bandhyopadhyay and Prof. V. Manjuladevi for their invaluable support, critical reviews and insightful comments and encouragement during my research work. I sincerely thank Prof. Anshuman Dalvi, Head of Department and Dr. Navin Singh, DRC Convener for their persistent support. Also, I wish to express my gratitude to Prof. D. D. Pant, Prof. Rakesh Choubisa and all the other faculty members of physics department for their kind support.

I would humbly express my regards to the Vice–Chancellor, Director, Deans, Associate Deans and Unit Chiefs of Birla Institute of Technology & Science (BITS), Pilani for providing me the opportunity to pursue my doctoral studies by providing necessary facilities and financial support. I express my gratitude to Prof. S K Verma (Dean, ARD) and Prof. Hemant Jadhav (Associate Dean, ARD), for their constant official support in organizing my research work. All other staff members of ARD, Mr. Raghuveer and Mr. Mahipal are also gratefully thanked for their help.

I wish to place on record my special thanks to Raman Research Institute (RRI) Bengaluru, CSIR–CEERI (SNTG group), Pilani, Material Research Center, MNIT Jaipur and department of chemical engineering, BITS Pilani for providing the experimental facilities for my research work. These were the most important inputs for my present research study.

One of the wonderful aspects of doing Ph.D. is going through it together with other lab members. I was lucky enough to work with a phenomenal batch in the surface science laboratory. I want to thank C. Karthik, Keerti Naresh Choudhary, Jitendra Kumar and Devanarayanan V. P. for their refreshing company and continuous support. I would

also like to offer my special thanks to Hitesh Agarwal for his continuos support in some aspect of research work. I would like to thank all my seniors, in particular, Sunita Joshi and Munesh Rathore for their support and motivation in all my endeavours. I would like to extend my warm thanks to all my friends in physics department as well as in other departments for their moral support, diversified help and several light–hearted moments which will always be remembered. The technical staff of the department, Mr. Rajeev Gaur, Mr. Srikant Sharma and Mr. Kundan Singh are also gratefully thanked for their help.

Special thanks go to my parents for their constant love and encouragement. My parents have shaped who I am today and supported me through every endeavor. A big thanks go to my brothers Vivek and Vikas, my sister Sapana and sister–in–law Parvin for supporting me spiritually throughout writing this thesis. I also thank my parents–in–law for sharing their wisdom and support.

The greatest thing about my time in BITS Pilani was meeting my husband, Amar. I am blessed to have met him and consider him to be my greatest discovery while at BITS Pilani. He is a great source of inspiration to me. More importantly, I have greatly appreciated his kind words when I need them most. I look forward to exploring the next chapter of our lives together.

There is an active and passive role of many people who helped me to arrive at this milestone. I may have forgotten to mention their names, but the help they offered has certainly made a home in my heart. I am reminded that the completion of this thesis represents the closing of one memorable phase of my life, but a new and more rewarding phase awaits.

Monika Poonia

Abstract

Thin films science and technology is one of the important fields of research and development. The reduction in the dimension of bulk material and approaching to a limit of 2–dimensional (2D) system by fabricating ultrathin films of the material provides a remarkable increase in surface–to–volume ratio as compared to the bulk material. Such huge increase in surface–to–volume ratio increases the activities of the material enormously and thereby the material properties. Such changes in the material properties in the state of ultrathin films promises a wide range of applications starting from the basic science research to various device fabrication. In this thesis, we have discussed the fabrication of the ultrathin films of carbon based nanomaterials through Langmuir monolayer, Langmuir–Blodgett (LB), self assembly, spin coating and drop casting techniques. In LB technique, the films are fabricated by arranging the molecules in the defined molecular states in a single layer onto some substrates.

The main aim of the work involves the development and characterization of ultrathin films of single–walled carbon nanotubes (SWCNTs) possessing different functional groups as well as functionalized graphene at air–water (A/W) and air–solid (A/S) interfaces. We have studied their interaction with different molecular species and found that the LB films can potentially be employed for sensing applications.

The Langmuir film (LF) of pristine SWCNTs is found to be stable at the A/W interface. The ultrathin films of the SWCNTs are transferred to solid substrates by LB technique. The films shows the dependence of SWCNTs alignment on solid support as a function of target surface pressure (π_t) during LB deposition. The films are characterized using Atomic Force Microscopy (AFM). The films deposited at surface pressures $\geq$2 mN/m shows SWCNTs forming a supramolecular donut structure. The ultrathin LB films of pristine SWCNTs are employed for methane (CH_4) gas sensing at the room temperature, and the sensing performance is compared with that of the film fabricated by the drop cast method. We found that the LB films are very sensitive to a change in the concentration of the CH_4 molecules in the ambient. The sensing performance improves due to presence of humidity in the ambient.

The functionalized SWCNTs offers not only the ease of thin films processability but also functional layer for attracting specific analytes in the sensing application. The LB films of octadecylamine functionalized SWCNTs (ODA–SWCNTs) are fabricated onto functionalized quartz crystal wafers of a QCM and are employed for sensing

the biological analytes *viz.* L–aspartic (L–asp) acid and bovine serum albumin (BSA) protein. The sensing performance of the LB films of ODA–SWCNTs is compared with that of thin film of randomly oriented ODA–SWCNTs obtained through spin coating technique. The highly oriented ODA–SWCNTs in the LB films may create large surface density of adsorption sites which support the further growth of the nucleation sites into bigger domains. This in turn yield better performance and high sensitivity of the analytes by the LB films of ODA–SWCNTs.

We have studied the Langmuir monolayer (LM) and LB films of the cationic surfactants. We formed the LB films of dioctadecyl ammonium bromide (DOAB) and studied the DNA sensing application. The lowest detectable concentration of DNA in the liquid is found to be 20 fM. The effect of polyethylene glycol functionalized SWCNTs (PEG–SWCNTs) in the aqueous subphase on the LM of dioctadecylamine (DODA) is also studied. We formed the LB films of DODA and DODA/PEG–SWCNTs at π_t = 10 mN/m from the ultrapure water subphase and characterized them using field emission scanning electron microscopy (FESEM). The FESEM image clearly shows the formation of liquid condensed domains in form of small domains and big dendritic domains. The LB film of DODA/PEG–SWCNTs also reveals the presence of nanotubes on the monolayer matrix of DODA. The DNA sensing studies of LB films of DODA/PEG–SWCNTs indicate that the lowest detectable concentration of DNA in aqueous medium is $\sim$3 fM which is far lower than that of the LB film of DOAB.

The carboxylic group functionalized graphene (G–COOH) is one of the important chemically modified graphene which has a potential for chemical and biological sensing. The LF of G–COOH at the A/W interface is found to be very stable and reversible. The functional layers of G–COOH were formed over the gold–coated quartz crystals by LB and spin coating techniques, and employed for sensing of urea in aqueous medium. The response is found to be linear in the given concentration range. The sensing performance of LB film of G–COOH is found to be better than that of spin coated film of G–COOH. The detection of urea in milk sample using the functional layers of G–COOH is also studied. The study on sensing of urea in milk sample indicate that the LB film of G–COOH can be employed for sensing urea even in the presence of differnt other species in the aqueous medium.

The ultrathin films of carbon based nanomaterials on solid substrates exhibit remarkable properties. Such properties can potentially be employed for device fabrication.

Contents

List of Figures

List of Tables

Abbreviations

AAs	Amino acids
AFM	Atomic force microscopy
ATR	Attenuated total reflectance
BSA	Bovine serum albumin
CAC	Critical aggregation concentration
CC	Constant current
CH	Constant height
CIP	Current–in–plane
CNTs	Carbon nanotubes
CNTFET	Carbon nanotube field effect transistor
CPD	Contact potential difference
CVD	Chemical vapour deposition
DMF	Dimethylformamide
DNA	Deoxyribonucleic acid
DOAB	Dioctadecyl ammonium bromide
DODA	Dioctadecylamine
ECG	Edge–carboxylated graphene
EHT	Extra high tension
ESP	Equilibrium spreading pressure
FE	Field emission
FESEM	Field emission scanning electron microscopy
FTIR	Fourier transform infrared spectroscopy
GO	Graphene oxide

G–COOH	Carboxylic acid functionalized graphene
HMDS	Hexamethyldisilazane
HPB	Hydrophobic
HPL	Hydrophilic
HPLC	High performance liquid chromatography
HOPG	Highly ordered pyrolytic graphite
IDE	Interdigitated electrodes
IP	Isoelectric point
ITO	Indium tin oxide
KP	Kelvin Probe
L–asp	L–aspartic
LB	Langmuir–Blodgett
LC	Liquid–condensed
LE	Liquid–expanded
LF	Langmuir film
LM	Langmuir monolayer
LS	Langmuir Schaefer
MFC	Mass flow controller
MOF	Metal organic frameworks
MUA	11–Mercaptoundecanoic Acid
MWCNTs	Multi–walled carbon nanotubes
NPs	Nanoparticles
ODA	Octadecylamine
ODA–SWCNTs	Octadecylamine functionalized SWCNTs
ODT	Octadecanethiol
PBS	Phosphate buffered saline
PEG	Polyethylene glycol
PEG–SWCNTs	Polyethylene glycol functionalized SWCNTs
PVD	Physical vapour deposition
P–F	Poole–Frankel
QCM	Quartz crystal microbalance

QDs	Quantum dots
RBM	Radial breathing mode
RO	Reverse osmosis
SA	Stearic acid
SAM	Self assembled monolayer
SEM	Scanning electron microscopy
SPR	Surface plasmon resonance
SPM	Scanning probe microscopy
SRI	Spreading resistance imaging
STM	Scanning tunneling microscopy
SWCNTs	Single–walled carbon nanotubes
TR	Transfer ratio
XRD	X–ray diffraction
0D	0–dimensional
1D	1–dimensional
2D	2–dimensional
3D	3–dimensional

Symbols

A	Area
A_i	Lift–off area
A_L	Area of monolayer from water
A_m	Area per molecule
A_o	Limiting area per molecule
A_S	Area of the substrate covered with monolayer
A_w	Area per μg
A/S	Air–solid
A/W	Air–water
a.u.	Arbitrary unit
$\mathrm{C_f}$	Sensitivity factor of quartz crystal
d	Diameter of carbon nanotube
dI/dV, σ	Differential conductance
E	Elastic modolus
E	Electric field
fM	Femto molar
G	Gas
H_2SO_4	Sulfuric acid
I	Current
I_t	Tunneling current
I_{PF}	Poole–Frankel current
k_B	Boltzmann constant
L	Liquid

L_1	Liquid expanded or low density liquid phase
L_2	Liquid condensed or high density liquid phase
M	Molar
nM	Nano molar
NH_4OH	Ammonia solution
pM	Pico molar
S	Solid
Si	Silicon
SiO_2	Silicon dioxide
V	Volt
$\triangle$f	Change in frequency
$\triangle$m	Change in mass
ϵ_r	Relative permittivity
ϵ_0	Permittivity of the free space
γ_0	Surface tension of water without monolayer
γ	Surface tension of water with monolayer
λ	Wavelength
μM	Micro molar
ω_r	Radial breathing mode frequency
π	Surface pressure
π_t	Target surface pressure
π_c	Collapse surface pressure
ρ	Surface density
τ	Time constant

Chapter 1

Introduction

1.1 Introduction

A thin film is a layer of material whose thickness ranges from a fraction of nanometer to several micrometers. The surface–to–volume ratio of a material when spread on to a substrate to form a thin film increases enormously. Therefore, the sensitivity and efficiency of thin film devices increase manifold. The physicochemical properties of the thin film may depend on the nature of molecular aggregation onto the substrate. The structures of the thin films on a surface can lead to the growth of bulk material, and hence the material properties can be controlled by manipulating the structures of the thin films. The form of such structures depends on the molecule–substrate and intermolecular interactions [1, 2]. Thin films find applications in semiconductor devices, solar cells, light–emitting diodes, liquid crystal displays, compact discs, electro–optic coatings, flat–panel displays, microelectromechanical systems, and photovoltaics and as an anti corrosion agent [3].

A single layer of molecules onto the substrate can be considered as ultrathin film. Ultrathin films can be fabricated using different techniques *e.g.* chemical vapour deposition (CVD), physical vapour deposition (PVD), spin coating, dip–coating, drop cast method, self–assembly and Langmuir–Blodgett (LB) technique [4–12]. Among these techniques, generation of mono– or multi–layers by LB film technique has a special significance for developing ultrathin films of appropriately functionalized molecules with controlled thickness and well–defined molecular orientation, as these have potential applications in sensors and other high–end technological devices [13–16].

1.2 Langmuir monolayer at air–water interface

A Langmuir monolayer (LM) is a stable monomolecular thick film of amphiphilic molecules at the air–water (A/W) interface. Amphiphilic molecules possess both hydrophilic and hydrophobic parts. The hydrophilic part is referred to as head group (polar) and hydrophobic part as tail group (non–polar). Examples of amphiphilic molecules are surfactants, block copolymers, lipids, fatty acids, cholesterol and protein [17–19]. Table 1.1 shows the some of possible hydrophobic (HPB) and hydrophilic (HPL) groups of amphiphilic molecules.

Table 1.1: Some of the possible HPB and HPL groups of amphiphilic molecules

HPB groups	**HPL groups**
Hydrocarbon chains (*e.g.* methyl)	Hydroxyl (–OH)
Fluorocarbon chains	Sulphates (–SO_4)
Phenyl	Sulfhydry (–SH)
Polycyclic	Carbonyl ($C = O$)
	Amino (–NH_2)
	Carboxyl (–COOH)
	Phosphate (–PO_4)

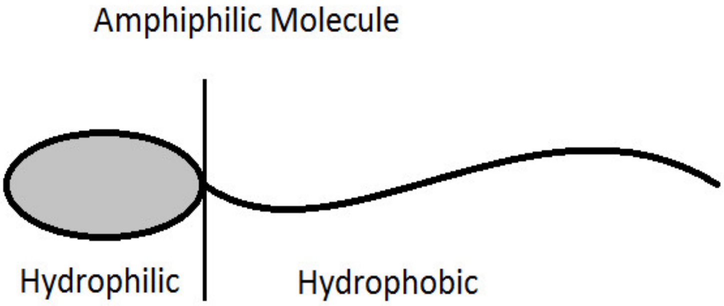

Figure 1.1: Schematic diagram of an amphiphilic molecule indicating hydrophilic head group and hydrophobic tail group.

A schematic diagram of an amphiphilic molecule is shown in Fig.1.1. The hydrophilic part of the molecule can easily form hydrogen bond with water. On the other hand, the hydrophobic part does not form hydrogen bond with water and prefers to stay away from the water. When amphiphilic molecules with proper balance between hydrophilic and hydrophobic parts are spread on the water surface, the hydrophilic part of the amphiphilic molecule get anchored to the water surface, whereas the hydrophobic part stay away from the surface. This gives rise to a monomolecular thick stable film at the A/W interface [20]. Such monomolecular thick film at the A/W interface is generally known as LM. A boundary surface between two different phases is called an interface. Generally, the thickness of the interface is only of the order of few Angstrom (Å). Therefore, an interface can be approximated to two-dimensional (2D) surface. The most important feature of an interface is the sudden change in both density and composition that gives rise to an excess free energy at the interface. The monolayer at the A/W interface can be considered as a 2D system.

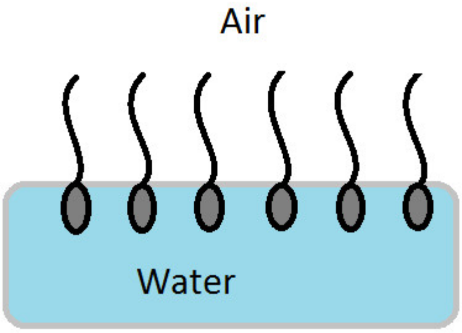

Figure 1.2: Schematic illustration of a spread monolayer of amphiphilic molecules at A/W interface.

A schematic representation of LM at the A/W interface is shown in Fig.1.2. The stability of the monolayer at the A/W interface is determined by the strength of polarity of the head group and the hydrophobicity of tail group of the molecules [21]. It has been found that the monolayer of fatty acid ($C_nH_{2n+1}COOH$) with n in the range of 12 to 24 can form stable film at the A/W interface [22]. If $n > 24$, the hydrophobicity dominates and molecules aggregate to form crystallites on water surface. If $n < 12$, the hydrophilicity dominates, and the molecules dissolve in water to form various concentration dependent structures [23]. Such structures are dependent on molecular interaction, temperature, pH and ion contents of the aqueous medium [17].

At very low concentration of the hydrophilically dominant amphiphilic molecules, the molecule adsorb and desorb from the interface and establish a dynamical equilibrium. Such monolayer at A/W interface is known as Gibb's monolayer [21]. Above a certain concentration, called the critical aggregation concentration (CAC), the molecules self–assemble into different structures *e.g.*, rods, discs, spheres, bilayers and vesicles. At concentrations much higher than the CAC, amphiphiles may form diverse liquid–crystalline phases, *e.g.*, bilayer stacks (lamellar phase) and hexagonal phases [24].

1.3 Surface Manometry

LM is an ideal system to study the thermodynamics of a 2D film where 2D plane is provided by smooth water surface. Surface manometry is a standard technique to study the thermodynamics and the surface phases in a LM. The presence of a monolayer at the A/W interface reduces the surface tension of water. Such reduction in the surface tension is defined as surface pressure (π). It is given by Eq.1.1:

$$\pi = \gamma_0 - \gamma \tag{1.1}$$

where γ_0 is the surface tension of the pure water and γ is the surface tension of water with film. The surface pressure can be measured using a transiometer connected with a Wilhelmy plate. In surface manometry, the surface density (ρ) of the amphiphilic molecules is varied and change in surface tension relative to pure aqueous subphase is recorded. The surface density can be varied either by changing number of molecules in a given area or by changing area for a given number of molecules. Practically, it is convenient to change area available for a fixed number of molecules. At a constant temperature, the variation of surface pressure as a function of area per molecule ($\mathrm{A_m}$) is known as π – $\mathrm{A_m}$ isotherm. The isotherm can provide the information about the different phases and phase transitions in monolayer at A/W interface [25, 26]. The schematic diagram of the experimental setup for obtaing π – $\mathrm{A_m}$ isotherm is shown in Fig.1.3. It consists of a trough (1) of dimension 60cm×20cm and two barriers (4) made up of teflon. Teflon is considered to be hydrophobic and oleophobic which assures no deposition of material onto the trough & barriers. The arrows indicate the direction of flow of temperature regulated water inside the chamber to control the temperature of the subphase. The subphase (2) is ultrapure ion–free water having a resistivity greater than 18 MΩ–cm obtained by passing reverse osmosis (RO) water through filtering and deionizing columns of a Milli–Q Millipore unit (DQ–5).

The amphiphilic molecules are dissolved in an appropriate organic solvent to obtain a solution of known concentration, and a volume of the solution is spread drop by

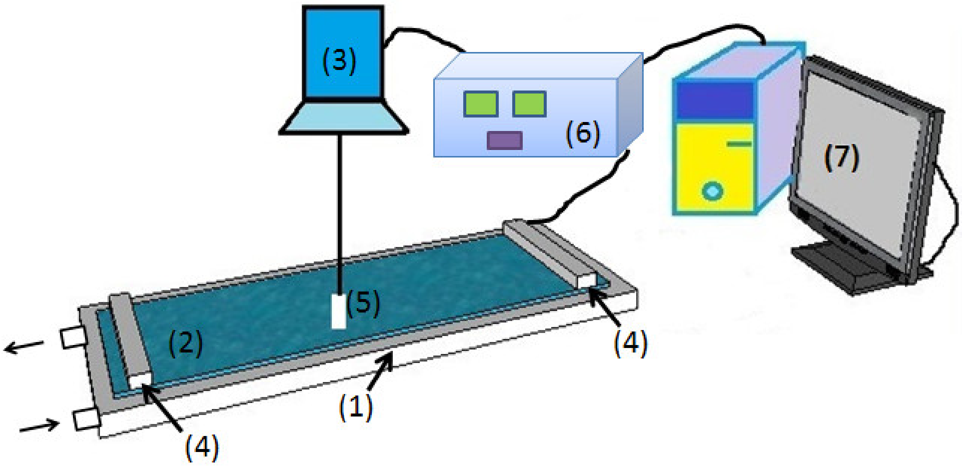

Figure 1.3: A schematic diagram of a LB trough. The components are: (1) teflon trough (2) liquid subphase (3) pressure sensor (4) barriers (5) wilhelmy plate (6) control unit (7) computer.

drop on the surface of water between the barriers using a Hamilton microsyringe. The solvent is allowed to evaporate for ~30 minutes before starting the compression. As the solvent evaporates, a monolayer is formed as dictated by the amphiphilic nature of the molecules. The head groups of amphiphilic molecules get anchored to the water surface and the tail groups stay away from the water surface. The surface density of the amphiphilic molecules in the monolayer is varied by changing the area available for the molecules by moving the barriers laterally. The barriers are driven by motors connected to a controller (6) which is interfaced with a computer (7). Barriers are coupled to each other so that it ensures a symmetric compression of the monolayer. The surface pressure is measured using a pressure sensor (3) which is connected with a Wilhelmy plate. A filter paper of appropriate size is used as the Wilhelmy plate (5). The benefit of the filter paper is that the wetting is more efficient due to the porosity, low cost comparative to a Platinum–plate and the light weight of filter paper increase its sensitivity towards the surface pressure. The filter paper is suspended from the pressure sensor and is made just to touch the surface of the water. The filter paper is allowed to soak water fully and the reading of the sensor is made zero. The surface pressure and area per molecule at a constant temperature is recorded simultaneously using the computer.

A schematic of π–A_m isotherm of a LM at A/W interface indicating the different phases and possible arrangement of molecules therein is shown Fig.1.4. The isotherm shows discontinuities in the form of kinks and plateau. The kink or plateau in the isotherm

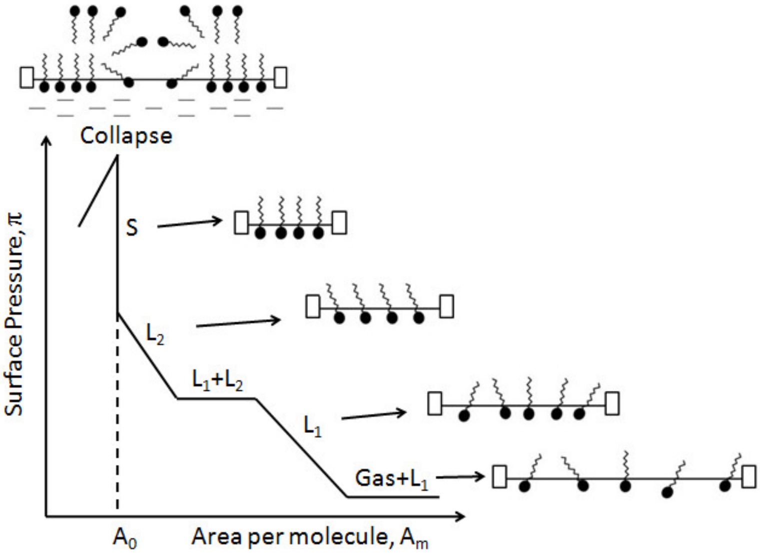

FIGURE 1.4: A schematic of surface pressure (π) – area per molecule ($\mathrm{A_m}$) isotherm of a LM at A/W interface indicating the different phases and possible molecular arrangement therein. The symbols $\mathrm{L_1}$, $\mathrm{L_2}$ and S represent liquid–expanded, liquid–condensed and solid phases, respectively.

indicate phase transitions. Due to practical limitations, the weak phase transitions sometimes does not appear exclusively as a prominent kink or plateau in the isotherm. Such weak phase transition can be studied by calculating in–plane elastic modulus (E) from the isotherm. E is an appropriate quantity for distinguishing very weak phase transitions and elastic nature of the monolayer in a given phase. The isothermal in–plane E [1] is defined as given by Eq.1.2

$$E = -\mathrm{A_m}\frac{\mathrm{d}\pi}{\mathrm{dA_m}} \tag{1.2}$$

At a very large $\mathrm{A_m}$, the molecules are far apart and do not exert any force on each other. This is a 2D gas phase. On compression, the molecules condense to a low density liquid state ($\mathrm{L_1}$). There are no positional and orientational orders in the arrangement of molecules in this phase. On further compression, the $\mathrm{L_1}$ phase transforms to a high density liquid state ($\mathrm{L_2}$) accompanied by a two phase ($\mathrm{L_1}$ + $\mathrm{L_2}$) coexisting region. This is known as high density liquid phase or condensed ($\mathrm{L_2}$) phase. In the $\mathrm{L_2}$ phase, molecules exhibit a long range orientational order and a quasi–long range positional order. On compression, the $\mathrm{L_2}$ phase transforms to a 2D solid (S) phase. On further compression, the monolayer collapses. This is indicated by a sharp decrease in surface pressure. The collapsed state is generally indicated either by a sharp decrease in π value or a plateau in the isotherm. In the collapsed state, the monolayer destabilizes and the molecules go to the third dimension. A plateau in the collapse state may indicate the formation of multilayer, whereas a sharp decrease may indicate a random crystallization into the 3–dimensional (3D) crystals. The nature of collapse varies from molecules to molecules. It also depends on the experimental conditions. The monolayer may fold or bend in the collapsed state [27–32].

As the monolayer is compressed starting from very large area per molecule, the surface pressure remains zero. The area per molecule at which the isotherm starts indicating very small and finite values of π (*e.g.* 0.2 mN/m) is known as lift–off area per molecule ($\mathrm{A_i}$). The average area occupied by the molecules in a phase is determined by extrapolating the corresponding region of the isotherm to the zero surface pressure on the $\mathrm{A_m}$ axis. The extrapolation of the steep region (*e.g.* S phase in Fig.1.4) of the isotherm to zero surface pressure is called limiting area per molecule ($\mathrm{A_0}$). This is the minimum area to which the molecules can be compressed on the water surface without collapsing the monolayer. The orientational state (tilt or untilt) of the molecules in a phase can be estimated qualitatively by comparing the extrapolated area per molecule with that of molecular cross–sectional area in the bulk single crystal. The isocycles of LM can be obtained by repeated compression and expansion of the monolayer. Small hysteresis and retraceable isocycles indicate stable and reversible phases of the LM. The shift in the isocycle curves towards the lower or higher $\mathrm{A_m}$ indicate unstable LM. The instability may arise due to dissolution of the molecules or the formation of irreversible aggregates on the water surface.

1.4 Formation of monolayer and multilayers at air–solid interface by various techniques

1.4.1 Langmuir–Blodgett Technique

The LB technique was introduced by Irving Langmuir and extensively applied by Katharine Blodgett for the deposition and characterization of thin films [33]. LB technique can be employed to form monolayer or multilayer films at the air–solid (A/S) interface. In this technique, the LM in a particular phase at the A/W interface can be

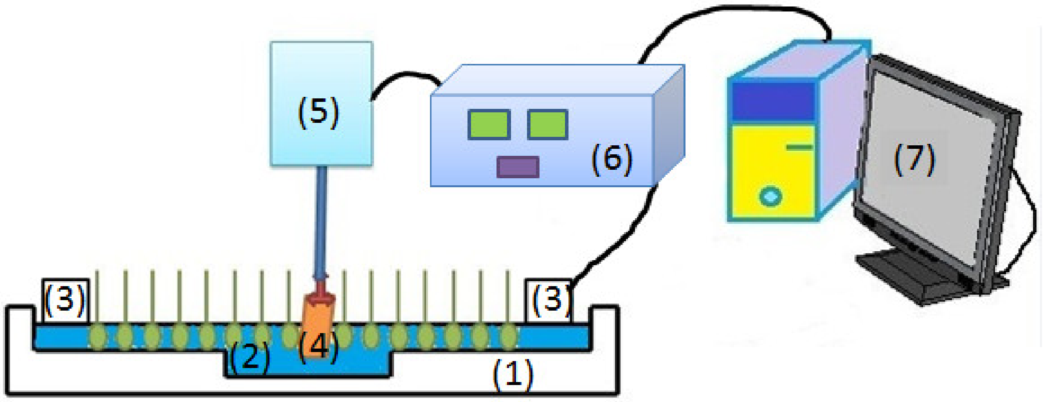

FIGURE 1.5: A schematic diagram showing the experimental setup for depositing LB films. The parts are as follows; (1) teflon trough with a well in the center, (2) subphase, (3) barriers, (4) substrate, (5) dipper, (6) control unit, (7) computer.

transferred layer by layer onto a solid substrate by vertically moving the substrate in and out of the subphase. During deposition, the surface pressure is fixed at some target value is called as target surface pressure (π_t). The schematic of experimental setup for LB deposition is shown in Fig 1.5. The setup is similar to that of the Langmuir trough except it possesses a well in the teflon trough and a dipper. For the LB film transfer, the trough has a motorized dipper which holds the substrate and it can be moved up and down very precisely. Such a motion makes the substrate to dip in and out of the subphase with a monolayer at the interface. During deposition, the surface pressure is fixed at π_t by a feedback mechanism [21, 34]. The barriers compress the monolayer until the π_t is attained. Any increase or decrease in surface pressure is fed back to the computer which in turn moves the barrier to maintain the required value of π_t. The efficiency of transfer of the monolayer on the solid substrate is estimated by measuring the transfer ratio (TR) [35]. The TR is defined as

$$\mathrm{TR} = \frac{\text{area of monolayer transferred from the A/W interface}}{\text{area of the substrate to be deposited}} \tag{1.3}$$

The value of TR = 1 indicate defectless LB film. There are different types of LB deposition. The deposition of the monolayer on the solid substrate can occur during emersion from (up stroke) or immersion into (down stroke) the water subphase, depending on the hydrophilic or hydrophobic character of the solid support [36–38]. If the substrate has a hydrophilic surface, the transfer of the monolayer will occur during the emersion. Then, the hydrophilic head groups are attached to the hydrophilic surface of the substrate, leading to a hydrophobic surface of the LB film.

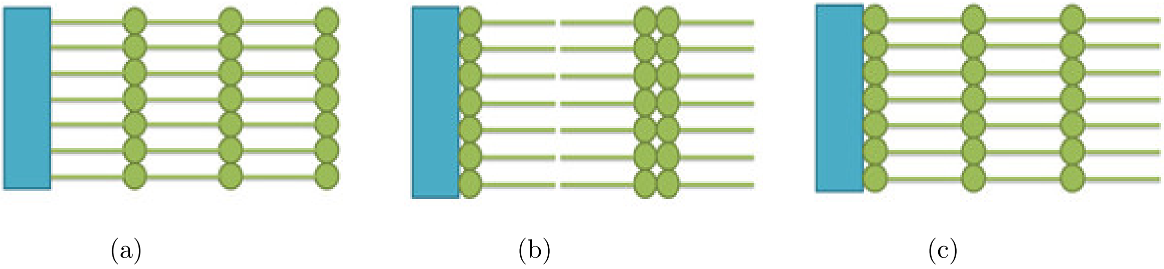

Figure 1.6: The schematic illustration of types of LB films. (a) X–type, (b) Y–type and (c) Z–type LB film.

On the other hand, if the substrate is hydrophobic, the deposition of the thin film will occur during the immersion, and the hydrophobic alkyl chains get attracted towards the surface, and the substrate becomes hydrophilic. With each additional layer transferred from the A/W interface onto the solid support, the latter changes its character from hydrophobic to hydrophilic. If the deposition starts with a hydrophilic substrate, the substrate becomes hydrophobic after the first deposition and the second monolayer will be transferred during the immersion. If the monolayer transfers during both the upstroke and downstroke of the dipper, such deposition is known as Y–type of LB deposition [33] (Fig.1.6b). On the other hand, if the deposition takes place only with either downstrokes or upstrokes, they are termed as X (Fig.1.6a) or Z–type (Fig.1.6c) of LB deposition, respectively. Sometimes a combination of these depositions are also observed [35]. The negative values of TR indicate desorption of the already deposited molecules [39]. The LB depositions are dependent on the nature of interaction between the substrate and the molecules, dipper speed, target surface pressure, ion contents of the subphase and temperature [17].

Since the LB film deposition technique allows for the preparation of highly ordered monolayers with a dense packing and precisely controlled thickness, LB monolayers have been used for immobilization of enzymes and other biomolecules in the development of various types of biosensors [40–48]. A biosensor is an analytical device which uses the specific interaction of the analyte with a biological molecule along with a physicochemically incorporated transducer to convert a molecular recognition event into an optical/electrochemical signal [49].

1.4.2 Spin Coating Method

Spin coating is a fast and economically easy method to generate thin and homogeneous organic films from solutions [50]. A known volume of a solution of material to be deposited is placed on the substrate, which is then spinned at a controlled speed. The fluid spreads due to centrifugal force. After evaporation of the solvent, a film of the material will be obtained. The thickness of a spin coated film will depend upon the concentration of solution and solvent evaporation rate which in turn depends upon the solvent viscosity, vapour pressure, temperature and local humidity. The more concentrated solution yield the thicker film. The schematic illustration of spin coating deposition technique is represented in Fig.1.7. In the spin coating process, interactions between substrate and solution layer are stronger than the interactions between solution surface and air. The advantage of spin coating is its ability to provide thin films from a few nanometres to a few microns in thickness in a quick, easy, and economical way.

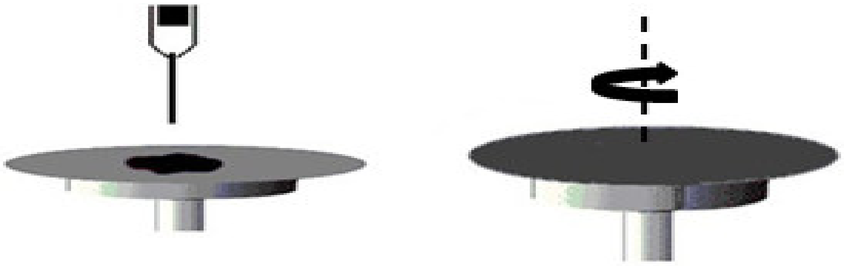

FIGURE 1.7: The schematic illustration of spin coating deposition technique.

1.4.3 Drop Casting Method

Drop casting is another technique for depositing a thin film of material from liquid phase onto a solid substrate. Drop casting simply involves placing drops of the liquid containing the desired material onto the surface of the substrate, and subsequently allowing the solvent to evaporate. Drop casting can produce variable results from nice, homogeneous organic films to poor organic films that show precipitation effects during drying. Fig.1.8 represents a schematic illustration of drop casting method.

Drop casting is a technique that allows for creating thick organic films; however, there is minimal control over the thickness and non–uniformity of resulting organic films, is a major disadvantage of this technique.

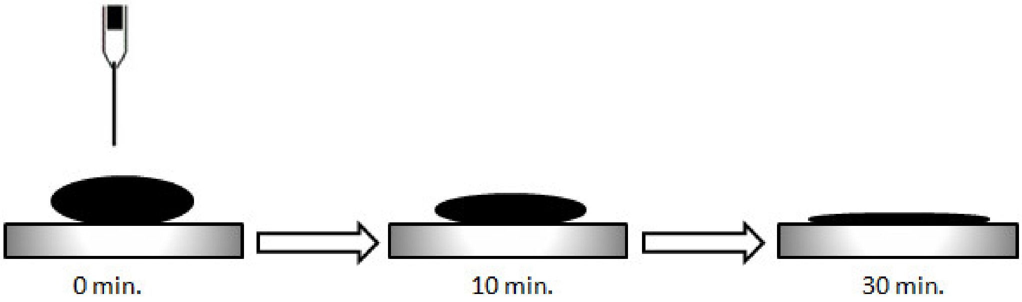

FIGURE 1.8: The schematic illustration of drop casting deposition technique.

The monolayer at the A/W interface can be transferred onto substrates by other techniques. These techniques are dip coating method, horizontal transfer method and Langmuir Schaefer's (LS) method. Dip coating is the precision controlled immersion and withdrawal of any substrate from a solution of material. In the horizontal transfer method, a hydrophilic substrate is kept immersed horizontally in the subphase and then the monolayer is formed at the A/W interface. The monolayer is compressed to achieve a required target value of π. Then the aqueous subphase is siphoned out very slowly from the other side of the barriers. The monolayer gets adsorbed onto the substrate as the water drains out. In the Schaefer's method, a hydrophobic substrate is allowed to touch the monolayer on the water surface. The hydrophobic part of the molecules gets adsorbed to the substrate. To facilitate the drainage of water, the substrates in either cases can be tilted by a small angle prior to the adsorption.

1.4.4 Self–Assembled Monolayers

The self–assembled monolayer (SAM) formation is one of the low cost and highly reproducible techniques to obtain a single layer of highly organized organic films at the A/S interface. The properties of the surfaces can be tailored easily by self–assembly. The concept was introduced by Zisman in 1946 and thereafter the field has grown remarkably. Self assembly by surfactant molecules leading to various supramolecular assemblies is another field of great importance [51] where the supramolecular structures are controlled by tuning the molecular interactions. The ultrathin films obtained through self–assembly possess numerous advantages as self assembly offers highly ordered and customizable surfaces in a very simple and low cost deposition process. SAM provides a greater flexibility to alter the surface functionality by altering the functional end of the film forming molecules. Therefore a variety of surfaces with different functionality can be created. Such flexibility made it viable that SAM can be potentially used for numerous industrial applications [52].

1.5 Experimental setup and sample preparation

1.5.1 Langmuir–Blodgett trough

A LB trough (LB2007DC, Apex Instruments Co.) is used for recording of π – $\mathrm{A_m}$ isotherm and fabrication of ultrathin LB films of different materials. The instrument consists of a trough of dimension 60cm×20cm and two barriers made up of teflon. Teflon is considered to be hydrophobic and oleophobic which assures no deposition of material onto the trough and barriers. Proper cleaning of the trough before monolayer spreading is very essential. The usual approach is to first fill the trough with dilute sulphuric acid and leave it overnight. Then the dilute sulphuric acid is suctioned out through a pump and the trough is rinsed throughly with ultrapure ion free water followed by cleaning using organic solvents like chloroform and acetone. The LB trough is enclosed in a glass box to avoid any thermal or air drift.

1.5.2 Subphase cleaning

The subphase used for the experiments is ultrapure ion free water. The ultrapure ion free water (resistivity $\geq$ 18 MΩ–cm) is obtained by feeding RO water into Millipore Milli–Q (DQ–5) filtering system. The trough is filled with the aqueous subphase and the surface is cleaned by compressing the barriers to a minimum area followed by suction of the macroscopic non–soluble impurities by means of a suction pump. The quality of the surface is checked by monitoring the change in surface pressure from uncompressed to fully compressed state of the barriers. The surface cleaning is continued until a tolerance of surface pressure 0.05mN/m is achieved.

1.5.3 Substrate cleaning

Various solid substrates like glass slides, coverslip, quartz plate, indium tin oxide (ITO) coated glass plates, silicon wafer and mica are used for LB deposition. Prior to deposition, substrates like coverslip, glass slide and silicon wafer are treated hydrophilically by boiling them in freshly prepared hot piranha solution (mixture of concentrated sulfuric acid and hydrogen peroxide in the ratio 3:1) for 10 minutes and then rinsed successively with ion–free water, absolute alcohol and acetone solvents. The substrates were then dried by blowing hot air at 70° C. The hydrophilicity is qualitatively checked by placing a drop of ultrapure water and observing the wettability. If the water completely and uniformly wets the substrate with contact angle $\sim$zero, the substrate is considered to be hydrophilic and very clean. The substrates like glass and Si wafers are treated hydrophobically by immersing the hydrophilically treated substrates in a solution (1:9, Hexamethyldisilazane (HMDS) : Chloroform) for $\sim$12 hours. Then substrates are rinsed with chloroform thoroughly and stored in ultrapure water.

1.5.4 Solvents for dispersing molecules

The commonly used solvents for dispersing the amphiphilic molecules are chloroform, benzene, acetone, toluene, cyclohexane, ethanol, methanol, dimethylformamide (DMF). The choice of the appropriate solvent for dispersing the molecules is such that it should be volatile and evaporate faster from the surface of water, disperses the amphiphilic molecules uniformly and immiscible with water. Chloroform is highly polar and it can disperse most of the organic molecules. It is immiscible in water and can evaporate rapidly from the surface (boiling point $\sim$61° C). Pristine carbon nanotubes (CNTs) are purely hydrophobic in nature. Moreover, such CNTs do not disperse easily in many organic solvents. CNTs can form a uniform dispersion in DMF solvent. However, the boiling point of DMF is 153° C and it needs very long time for its evaporation.

1.6 Molecules forming Langmuir monolayer and Langmuir–Blodgett films

There are numerous materials (shown in Table 1.2), which can form stable LM at A/W interface and can be transferred onto solid substrates by LB technique. Conventionally, amphiphilic molecules like long chain fatty acids, lipids, proteins, cholesterol and its derivatives form LM at the A/W interface and have been widely studied. Carbon based materials like CNTs as well as their functionalized form, quantum dots (QDs) and graphene also form stable LM and can be transferred onto various solid substrates by LB technique.

Table 1.2: Different materials forming stable LM

Materials	**Reference**
Fatty acids	[53–58]
Phospholipids	[32, 42, 59]
Proteins	[60–62]
Cholesterol and derivatives	[63–66]
Quantum Dots (zinc oxide, cadmium sulfide)	[67–69]
Carbon based nanomaterials (CNTs, graphene)	[70–75]
Biological systems (DNA, biopolymers)	[32, 42, 59–62, 76–80]

This thesis comprises the results of studies on thin films of carbon based nanomaterials. Different types of carbon materials such as pristine CNTs, octadecylamine functionalized CNTs (ODA–CNTs) and polyethylene glycol functionalized CNTs (PEG–CNTs) as well as carboxylic acid functionalized graphene are studied. Pristine CNTs as well as functionalized CNTs are procured from Carbon Solutions Inc, USA in highly purified form. Functionalized graphene is obtained from Redex Technologies Pvt. Ltd. These compounds are used as received, without further purifications.

1.6.1 Pristine CNTs

CNTs have attracted a great deal of attention due to their unique structural, electrical, and mechanical properties. Recently, there has been an intense interest in exploring some of their novel properties, such as superior mechanical strength, flexibility, electrical conductivity, and availability of chemical functionalization [81, 82]. CNTs can be thought of as the seamless hollow tubes composed of rolling graphite sheet. According to the layer number of graphite sheet, the CNTs can be divided into single–walled carbon nanotubes (SWCNTs) and multi–walled carbon nanotubes (MWCNTs). Several synthesis schemes, such as arc discharge, laser ablation and CVD have been developed for the preparation of CNTs [83]. Pristine CNTs are purely hydrophobic in nature. There are several reports on stable LM exhibited by hydrophobic nanoparticles at the A/W interface [84–88]. Such systems attain stability due to a balance between the attractive van der Waals interaction and steric repulsion between the particles. Pure CNTs can form stable LM at A/W interface. LM can be transferred onto different solid substrates and these LB films can be characterized using different techniques.

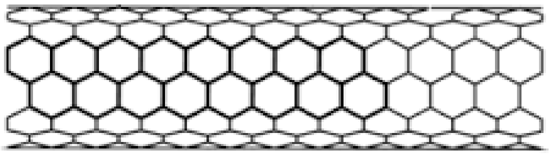

Figure 1.9: The chemical structure of pure CNTs.

1.6.2 Functionalized CNTs

Solubility and dispersibility of CNTs in solvent can greatly be enhanced by chemical functionalization of the CNTs. Polyethylene glycol (PEG) is a hydrophilic nonionic polymer used in many biochemical and pharmaceutical applications. PEG is used to functionalize CNTs to improve its dispersion in solvents [89, 90]. PEG functionalized SWCNTs (PEG–SWCNTs) are highly hydrophilic in nature. Some stabilizer like polymers and surfactants can be added to the monolayers to form a stable LB film and to study the intermolecular interaction. Long–chain octadecylamine (ODA), is also used to disperse the CNTs in organic solvents [81]. CNTs grafted with ODA were found well dispersed in organic solvent without aggregation at relatively high solubility [82]. ODA functionalized SWCNTs (ODA–SWCNTs) possess good spreading properties at A/W interface. Highly ordered LM of ODA–SWCNTs can be formed using LB technique and sensing applications of functionalized CNTs can be explored using quartz crystal microbalance (QCM) measurements.

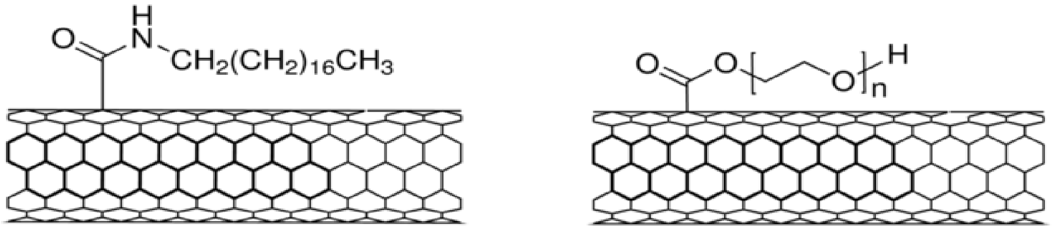

(a) (b)

FIGURE 1.10: The chemical structure of (a) ODA–SWCNTs and (b) PEG–SWCNTs.

1.6.3 Functionalized Graphene

The unique electrical, optical and mechanical properties of graphene have led to enormous possibilities of innovative applications including light emitting diodes, solar cells, optoelectronics, sensors etc [91–94]. Surface functionalization can improve the solubility of graphene in organic solvents. Carboxylic acid functionalized graphene (G–COOH) is easily dispersible in various polar solvents. The edge–modified functional groups tend to repel each other to effectively open up the edges of the G–COOH, leading to self–exfoliation in solvent [95]. The presence of carboxylic acid groups at the periphery of graphene sheets provides hydrophilicity while the basal graphene plane remains largely hydrophobic. G–COOH monolayers thus possess an overall amphiphilic character, which makes it possible to spread them and form stable LM at A/W interface, such LM can be transferred onto solid substrate to form LB monolayers and multilayers. Because of its interesting properties, a thin film of carboxylated graphene has found its way into a wide variety of applications [96].

1.6.4 Biological system

Amphiphilic molecules are ubiquitous in biological systems. The lipids are the basic constituents of the cell membrane and are amphiphilic in nature. There are extensive studies on the LM and LB films of lipid molecules [32, 42, 53–59]. Biopolymers, proteins and deoxyribonucleic acid (DNA) are well known to assemble on water surface and form a stable LM [60–62, 76–80]. Mixed monolayers are of considerable interest in many systems like biological membranes. They have been extensively studied. It provides useful information regarding the interaction and orientation of the component molecules.

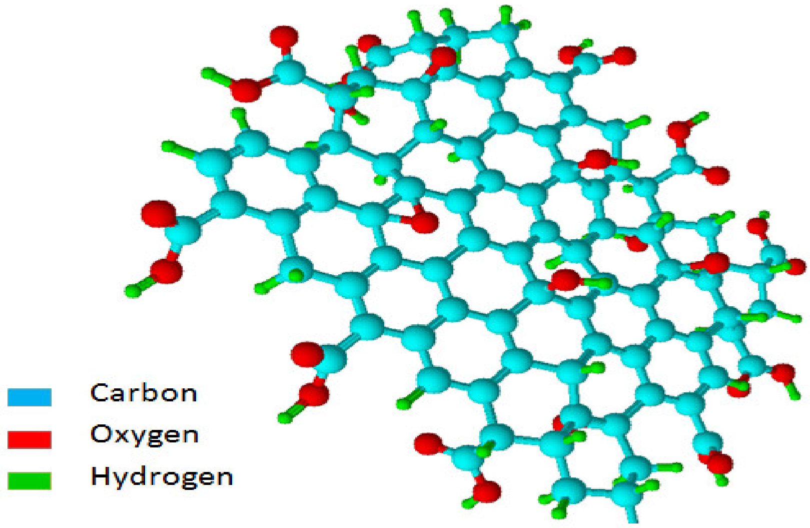

Figure 1.11: The chemical structure of G–COOH.

1.7 Characterization Techniques

There are numerous techniques to characterize the thin films deposited on solid substrates. Atomic force microscope (AFM), scanning electron microscope (SEM), Fourier Transform Infrared (FTIR) Spectroscopy, X–Ray diffraction (XRD) and Raman spectroscopy are used for thin film characterization [97–99].

The formation and characterization of thin films are prepared using the techniques listed in the Table 1.3.

1.7.1 Scanning Probe Microscopy (SPM)

In scanning probe microscopy, a physical interaction is established between a sharp probe and the sample under investigation. With a precise control of the motion of the probe in lateral and vertical direction, the various properties related to the sample film can be extracted. Some of the important types of SPM are STM and AFM. Since the invention of the STM in 1981 by Binnig and Rohrer [100] and AFM in 1986 by Binnig and Gerber [101], these instruments have established themselves as the most important techniques in surface investigations. Furthermore, they have been used to manipulate surface structures ranging from ∼100 nm down to the atomic dimensions.

Table 1.3: Experimental techniques for the formation and characterization of thin films.

Instrument	**Model, Company**	**Purpose**
LB Technique	LB2007DC, Apex Instrument Co.	Obtaining surface pressure–area per molecule isotherm and fabrication of LB films on solid substrates
Spin Coating Unit	SCU2007, Apex Instrument Co.	Deposition of thin films on solid substrates
AFM	NTMDT, Solver Pro.	Obtaining topography and related spectroscopy
FESEM	ZEISS, Sigma	Surface texture and surface morphology of thin films
FTIR	Perkin Elmer	Functional groups in LB films
Raman Spectroscopy	Renishaw inVIA reflex micro Raman Spectrometer, STR250 Laser Raman Spectrometer	Structural information, chemical composition
XRD	PANalytical XPERT–PRO powder	Phase identification and grain size of a crystalline material
Conductance Measurement	Keithley sourcemeter 2400	Charge transport mechanism in thin films
Quartz Crystal Measurement	QCM200–stanford research system	Sensing applications

Scanning Tunneling Microscope (STM)

The basic components of a STM are shown schematically in Fig.1.12. In STM, a very sharp metal tip is brought very close (< 10Å) to a conducting surface. When a low bias voltage is applied across the tip–sample junction, electrons tunnel across the gap and produce a measurable tunneling current. The tunnelling current is amplified by the current amplifier. The position of the tip is accurately controlled by the piezoelectric tube scanner. The resulting tunneling current has an exponential dependence on the tip–sample separation, and therefore an atomic resolution of surface features is possible to obtain using STM.

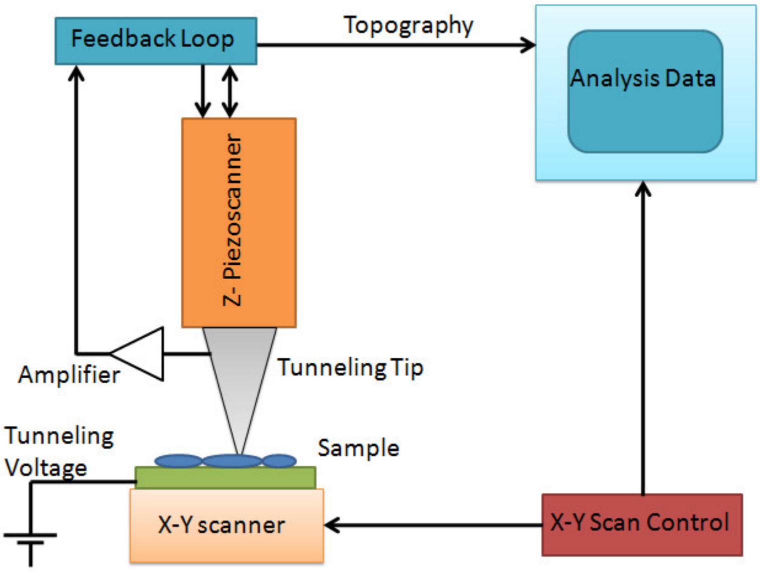

FIGURE 1.12: The schematic diagram of working principle of STM.

STM works in two modes *i.e.* constant current (CC) mode and constant height (CH) mode. While scanning the surface in CC mode, the tunneling current between the tip and the sample is kept constant. In this mode, the height of the tip is adjusted automatically using a feedback circuit to achieve the constant tunneling current. The variation in tip height as a function of lateral coordinates (x,y) gives the topographic information of the sample. In CH mode, the height of the tip is kept constant and the tunneling current is recorded as a function of (x,y). The CH mode provides the electronic information of the sample [1]. The resulting tunneling current varies with tip–to–sample spacing, and both the sample and the tip must be conductors or semiconductors. Thus, STM cannot image insulating materials.

Atomic Force Microscope (AFM)

In STM, both the sample and the tip must be conductors or semiconductors. Thus, STM cannot image insulating materials. STM signal interface with air molecules if scanned in ambient. In order to overcome these disadvantages of STM, another microscope in SPM family has been invented *i.e.* AFM. Unlike STM, AFM can be used to examine both conducting and non–conducting surfaces. AFM can be applied in a broad range of environments (ultra high vacuum, air, liquid, gases, etc).

AFM gives the topographic images by sensing the atomic forces between a sharp tip and the sample. A schematic diagram of an AFM is shown in Fig.1.13. Here, the tip is mounted on a cantilever. The head of the tip is coated with a reflecting material like gold and it is illuminated by a laser light. The reflected light is collected on a quadrant photodiode. Any deflection in the tip due to its interaction with the sample is monitored by measuring a distribution of light intensity in the photodiode.

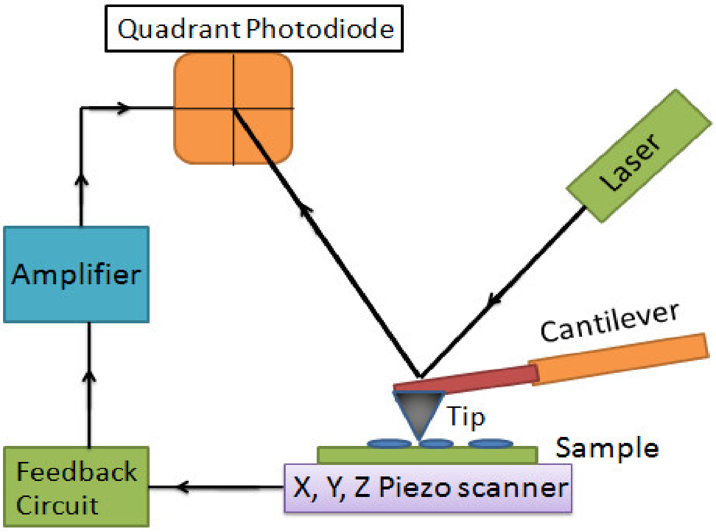

Figure 1.13: The schematic diagram of working principle of AFM.

Since the imaging process uses the force of interaction of the tip to that of the sample, AFM is used for imaging even the non–conducting samples. AFM measurements can be performed primarily in contact and tapping or non–contact modes. In contact mode, the tip is brought into direct contact with sample and the surface is scanned. The force of interaction between the tip and the sample lies in the repulsive regime in the intermolecular force curve. The force between the tip and the sample is kept constant and by monitoring the bending of the cantilever as a function of (x,y), a topographic image can be obtained. In tapping mode, the tip is allowed to oscillate nearly to its resonant frequency on the sample at a given amplitude and frequency. Due to interaction between the tip and the sample, the amplitude and phase of oscillation of the tip change. The change in amplitude can be used to obtain a topographic map of the sample. The phase change gives an insight about the chemical nature of the sample. In the non–contact mode, the tip is oscillated at a distance from the sample so that the two are no longer in contact. Besides its better–quality resolution, the AFM provides extraordinary topographic contrast, direct height measurements.

3D AFM images can be achieved without expensive sample preparation and yield far more complete information than the 2D profiles available from cross sectioned samples [1, 101].

In this thesis, SPM (Solver Pro, NTMDT) is used to scan the thin films of carbon materials deposited on solid substrates. The LB films are scanned in spreading resistance imaging (SRI) mode using diamond coated conducting tips (DCP series) having spring constant $\sim$ 8 N/m. In the SRI mode [102], the tip scans the sample while in contact with the surface maintaining a constant force between tip and sample. In our study, the bias voltage applied between tip and sample was 0.5 V. The SRI mode provides valuable information on the height map and tunneling current map of the film simultaneously. AFM has been used in contact mode to study the topography of thin films of carbon based nanomaterials as a function of target surface pressure of LB film deposition. Besides, AFM has also been used to see the change in morphology due to interaction of carbon nanomaterials with different organic compounds and biomolecules in order to ascertain the sensing application of thin films of carbon materials.

1.7.2 Field Emission Scanning Electron Microscope (FESEM)

Electron microscopes use a beam of highly energetic electrons to probe objects on a very small length scale. In standard electron microscopes, electrons are mostly generated by heating a tungsten filament (electron gun). In a FESEM, on the other hand, the probe electrons are generated by the application of high electric field. Schematic diagram of working principle of FESEM is shown in Fig.1.14. Field emission (FE) is the emission of electrons from the surface of a conductor caused by a strong electric field. An extremely thin and sharp tungsten needle (tip diameter 10–100 nm) is employed as a cathode. The acceleration voltage between cathode and anode is commonly $\sim$0.5 kV to 30 kV. The apparatus requires an extreme vacuum ($\sim 10^{-9}$ Torr) in the column of the microscope. Because the size of electron beam produced by the FE source is about 1000 times smaller than that in a standard microscope with a thermal electron gun, the image quality will be markedly improved. FESEM is a very useful tool for high resolution imaging of surfaces [103].

FESEM from ZEISS, Sigma (RRI, Bengaluru) was used to determine the surface morphology of thin films deposited on solid substrates using different deposition techniques.

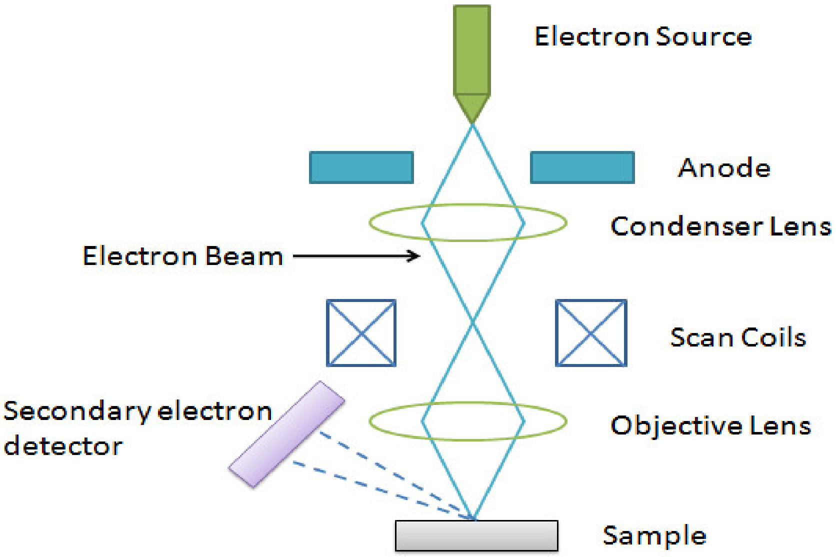

Figure 1.14: The schematic diagram of working principle of FESEM.

1.7.3 Fourier Transform Infrared (FTIR) Spectroscopy

In this thesis, FTIR spectroscopy [104] has been used to study the functional groups in carbon materials as well as their composites. The FTIR characterization of the films is carried out using a Perkin Elmer FTIR system in attenuated total reflectance (ATR) mode. The ATR crystal consists of an IR transparent material with a high refractive index and has polished surfaces. The infrared beam enters the ATR crystal at an angle of typically 45° (relative to the crystal surface) and is totally reflected at the crystal to sample interface. The fraction of the light wave that reaches into the sample is called the evanescent wave. In those spectral regions where the sample absorbs energy, the evanescent wave will be attenuated. After one or several internal reflections, the IR beam exits the ATR crystal and is directed to the IR–detector. The spectra are recorded from 400 to 4000 cm^{-1}. The films are deposited on Si/SiO$_2$ wafers, which are chemically very stable and do not have strong lattice absorption bands corresponding to the infrared region. FTIR spectroscopy was used to characterize the ultrathin LB films of functionalized graphene using Perkin Elmer Frontier FTIR (Dept. of chemical engineering, BITS Pilani).

1.7.4 Raman Spectroscopy

Raman spectroscopy is a form of molecular spectroscopy that involves the scattering of electromagnetic radiation by atom or molecules. It probes the vibrational, rotational and other low frequency modes of molecules. Raman spectra arise due to inelastic collision between incident monochromatic radiation and molecules of sample [105, 106]. Raman spectroscopy can be used to characterize the chemical composition and structure of a sample. Raman characterization of ultrathin LB films as well as bulk carbon materials is carried out using Renishaw inVIA reflex micro–Raman spectrometer (CEERI, Pilani) and STR250 Laser Raman Spectrometer (MRC, MNIT Jaipur).

1.7.5 X–Ray Diffraction

The X–ray diffraction (XRD) is a useful tool to study the structures and crystalline size of the material [107–109]. XRD from PANalytical XPERT–PRO (MRC, MNIT Jaipur) was used to analyze the crystallinity of the films of G–COOH. The diffraction data was acquired by exposing the samples to Cu–Kα X–Ray radiation, which has a characteristic wavelength (λ) of 1.54 Å with an operating voltage and current maintained at 40kV and 40mA. The data was collected between scattering angles (2θ) 5–60° at a scanning rate of 2° min^{-1}.

1.7.6 Current–Voltage (I– V) Characterization

For current–voltage (I–V) characterization of SWCNTs and graphene, a single layer of LB film was deposited onto interdigitated electrodes (IDE). A composite layer of titanium (30 nm) and gold (200 nm) was deposited onto Si/SiO$_2$ substrate for the formation of IDE using e–beam evaporation method in the ultra high vacuum $\sim 10^{-8}$ Torr. An optical photolithography was carried out for delineation of electrode structure. The fabricated IDE exhibited 10 μm line width and 10 μm gap between two electrodes. Voltage is applied across the gold pads of the IDE, and the corresponding current is measured using a source meter (Keithley, model No. 2400).

1.7.7 Quartz Crystal Microbalance Measurement

The QCM is a simple, cost effective, high–resolution mass sensing device, based upon the piezoelectric effect [110]. The measuring principle of QCM technique is based on the precise oscillation of the gold coated quartz crystal at their resonant frequency when an alternating voltage is applied. The resonance frequency is shifted by the addition or removal of a small mass due to oxide growth/decay or film deposition at the surface of the crystal resonator. The change in frequency ($\triangle$f) is directly proportional to the change in the mass per unit area ($\triangle$m). The mass per unit area on the surface of quartz crystal is estimated using the Sauerbrey equation (Eq.1.4).

$$\Delta f = –C_f \Delta m \tag{1.4}$$

where c_f is constant [111]. The AT–cut gold–coated quartz crystals exhibiting a resonance frequency of 5 MHz can be functionalized using different techniques *i.e.* LB technique, spin coating and SAM. Sensing of biomolecules can be investigated in static and dynamic mode. In static mode, QCM is used to monitor mass changes by injecting the solution of analytes onto crystal resonator. In dynamic mode, the solution of molecules to be sensed in passed through the surface of functionalized quartz crystal. As molecules bind to crystal surface the frequency of oscillation decreases, and as molecules dissociate from the surface the frequency of oscillation increases. By monitoring frequency change with time, adsorption parameters such as kinetic rates and affinity can be determined.

The QCM device (QCM200, SRS, USA) is used to study a number of SAM and LB films of surfactants and carbon based nanomaterials.

1.8 Literature review

The thin films of nanomaterials on solid substrates exhibit remarkable properties. Such properties can potentially be employed for device fabrication. Due to strong van der Waals interaction, the CNTs generally exist as the cluster of random network. In order to improve the device performance, CNTs should be aligned onto the active area of the device. The alignment can be achieved from a solution of CNTs in a dispersing medium. It is difficult to disperse CNTs in solvent. Therefore, a rather extensive effort has been devoted to achieving good dispersion of pristine CNTs through chemical functionalization and physical interactions. The fabrication of well organized thin film of CNTs through solution route relies on their dispersion in solvent. Nguyen *et al.* [112] have studied the dispersion of CNTs in various solvents. The most common technique applied to disperse CNTs is the ultrasonication of the material in DMF solvent. The dispersion of the CNTs in the solution has been studied using spectroscopic techniques. Though denatured MWCNTs has the best dispersibility in DMF solution, the pristine single–walled CNTs can also have good dispersibility in DMF.

For higher sensitivity and better device performance, the nanomaterials can be aligned on active area of the device. The aligned CNTs may have better performance than the network of random CNTs. There are two main categories for the alignment of CNTs: the post synthesis assembly and the in situ growth approaches. The post synthesis assembly approach mainly involves dispersing CNTs in solutions and aligning CNTs using spin coating, LB technique, mechanical shearing and blown bubble film techniques [113, 114]. The LB method of film deposition provides possibilities for preparing highly ordered, densely packed, and defect–free molecular films. There are some studies on the Langmuir film (LF) of CNTs at the A/W interface. Since pristine CNTs are insoluble in many solvents, it is difficult to form LM and hence LB films. Kristic *et al.* [71] have prepared LB film of CNTs by dispersing them in a surfactant (lithium dodecyl sulfate) solution and spread on a subphase of aqueous solution of poly(allylaminehydrochloride). LF consisting of CNTs and surfactant molecules were deposited on substrates possessing lithographically created electrode arrays. Electrical transport measurements were performed on individual thin bundles at room temperature and 4.2 K. At the room temperature, the I–V characteristic show a linear behavior and at low temperatures, the I–V characteristics show a non–linear dependence with step–like features.

It has been found that the solubility and dispersibility of CNTs in solvent can greatly be enhanced by chemical functionalization of the CNTs. The functionalized CNTs can form stable solution in organic solvents without aggregation indicating relatively high solubility. In addition, the surface modification may lead to the weakening of the mutual attractive force between CNTs, causing exfoliation of the bundles of CNTs into individual nanotubes [81]. Functionalized CNTs may form a stable LM at an A/W interface, and it can be transferred to various solid substrates by traditional

LB technique. Jia *et al.* [73] have done the SEM study of LB films of functionalized CNTs, and have found highly ordered in–plane orientation of CNTs films deposited at different values of π_t. It was found that the distance between the aligned CNTs decreased with increasing value of π_t of LB film deposition. The phase behavior of the spreading monolayer was studied by π – A isotherms at different temperatures and different compression speeds. The π – A isotherm curves indicated that the monolayer of chemically functionalized CNTs has good surface spreading properties at lower temperature and at lower compression speed [115]. Guo *et al.* [116] have reported a study on multilayer LB films of functionalized CNTs. Functionalized CNTs dispersed in an amphiphilic polymer matrix were spread on water surface and LB films were deposited on hydrophobic quartz plate. It has been reported that functionalized tube orientation can be controlled to some extent. In another study, Guo *et al.* [70] has reported the formation of uniform multilayers of octadecylamine functionalized CNTs deposited on hydrophilic substrates using LB technique. AFM imaging and Raman spectra indicated that chemically modified CNTs oriented almost along the dipping direction on hydrophilic substrate. Thin films containing SWCNTs mixed with arachidic acid have been fabricated using LB deposition. The morphologies of the films were studied using AFM. Single layer of pure SWCNTs exhibited relatively high, approximately ohmic conductivity for low applied voltages, while mixed LB films exhibited non–linear current versus voltage behavior [117].

Gas sensors have attracted intensive research interest due to the demand of sensitive, fast response, and stable sensors for industry, environmental monitoring, biomedicine and pharmaceutical applications. The development of nanotechnology has created huge potential to build highly sensitive, low cost, portable sensors with low power consumption. The extremely high surface–to–volume ratio with possibility of chemical modification, the nanomaterials are ideal for the adsorption of gas molecules. Recently, applications of carbon nanotubes as oxygen [118] and methane [119] gas sensors have been reported. Ong *et al.* [120] have described the possibility of obtaining a gas responsive multiwall CNTs–SiO_2 composite for monitoring CO_2, O_2 and NH_3. Absorption of different gases in the above composite layers changed the permittivity and conductivity of the material. Kong *et al.* [118] have demonstrated the use of CNTs for detecting NO_2 and NH_3. They found that exposure to NH_3 caused 100–fold depletion in conductance while exposure to NO_2 increased the conductance by almost three orders of magnitude. In terms of application, LB films of CNTs may contribute to developments in design and fabrication of chemical sensors, biosensors, optical devices and other molecular and nanoscopic structures.

Graphene is another form of carbon based nanomaterials. The unique 2D structure of graphene, combined with outstanding electrical conductivity and thermal conductivity, high optical transmittance, exceptional mechanical flexibility and durability, makes them an ideal candidate for a wide range of potential applications, including flat display, optoelectronics, sensors, energy conversion and storage systems, capacitive deionisation etc. LB assembly presents an effective approach for arranging 2D nanosheets into high–quality film architectures via controlled compression at the A/W interface. These LB films of graphene are capable of adsorbing analytes, providing the largest sensing area per unit volume. Graphene layer offers enormous gain in surface–to–volume ratio and therefore making it capable of interacting even with a single molecule of the target gas or vapor species, which eventually results in the ultrasensitive sensor response. Rumyantsev *et al.* [121] recently have reported graphene field–effect transistor (FET) based selective gas/vapor sensors. They demonstrated that vapors of different chemicals (*e.g.*, methanol, ethanol, tetrahydrofuran, chloroform, acetonitrile, toluene, and methylene chloride) show distinctly different effects that can be easily distinguished from the low–frequency noise spectra of graphene. Fowler *et al.* [122] have deposited single layer graphene by spin coating method on interdigitated electrode arrays where the operating temperature was monitored by a suitably designed micro hot plate. Four point resistance measurements are done by using two serpentine electrodes between the interdigitated electrodes. The device was tested for the detection of NO_2, NH_3, and 2,4–dinitrotoluene. Current versus voltage characteristics were found to be linear and ohmic in all cases, independent of the metal electrodes or presence of analyte. Single–layer graphene flakes presented a higher baseline resistance and superior sensitivity. Recently, in a study Yao *et al.* [123] have demonstrated the chemically derived graphene oxide (GO) thin film as a sensitive coating on electrodes of QCM for humidity detection in the range of 6.4–93.5% at room temperature. Thin film of GO exhibits an excellent humidity sensing performance. It is further concluded that the frequency response of the QCM is dependent on adsorbed/desorbed masses of water molecules on GO thin film in the large relative humidity range.

1.9 Gap in research

Many experimental and theoretical studies have revealed the outstanding properties of carbon nanomaterials. These studies enable us to understand various interactions and mechanisms involved in fabrication of devices based on thin films of carbon nanomaterials. CNTs based thin films offer potential applications as conducting and semiconducting layer in various types of electronic, optoelectronic and sensor systems. However, challenges still exist in understanding different aspects of thin films of carbon materials. Some of the research gaps which are addressed in this thesis, are discussed in this section.

There are some practical limitations regarding the solubility of CNTs in many organic solvents. Due to such limitations, there are not many studies on thin films of pristine CNTs. In some reports, CNTs are dispersed in polymer matrix before deposition. The electrical and magnetic properties of such thin films are greatly influenced by the polymer matrix. Therefore, it is desirable to fabricate the thin films of pristine CNTs on surface. For some device fabrication, it is essential to control the alignment of CNTs onto the surfaces so that the properties of the fabricated device can be optimized for their best performance. The CNTs can be aligned onto the surfaces by various techniques. LB is the most promising one as it provides a control over the ordering of the CNTs during the deposition, the thickness of the film, and a control over tuning the functionality of the films.

In chapter 2, we report the formation of a stable and reversible LF of bundles of SWCNTs at the A/W interface. We transferred the LB films on conducting ITO substrates at different values of π_t and characterized the films using an AFM in SRI mode. We found a significant effect of π_t of deposition on the morphology of the SWCNTs in the LB films. We obtained a supramolecular assembly of the SWCNTs in the LB films deposited onto ITO substrate in the liquid like phase of the LF.

Development of sensors for detecting various chemical species in many industrial, medicinal, environmental pollution control and commercial applications is in great need. In this regard, carbon materials are emerging as a promising candidate for sensing application because of the large change in physicochemical properties due to small perturbation on adsorption of analytes. Unlike semiconducting based sensors, CNTs based sensor can work even in room temperature.

For some of CNTs based devices, it will be interesting to align the CNTs on IDE with a proper orientation. When electron–withdrawing molecules or electron–donating molecules interact with the semiconducting CNTs, they will change the density of the main charge carriers, which changes the conductance of CNTs. The electrical properties of such organized LB films can be measured and the electrical behavior of LB films can be compared with those of bulk CNTs. This behavior forms the basis for applications of CNTs as gas sensors.

In chapter 3, we have demonstrated a control on the alignment of SWCNTs on the Si/SiO_2 substrate during the ultrathin film fabrication by LB technique. We have demonstrated the methane (CH_4) gas sensing capability of the aligned SWCNTs in the LB film at the room temperature. The sensing capability of the aligned SWCNTs in single layer of LB film of SWCNTs is compared with that of randomly oriented SWCNTs in the film grown by drop cast method. We found that the gas sensing capability of the LB film of SWCNTs is more efficient than that of the drop cast film.

The CNTs are functionalized for dual purpose: Firstly, it can be easily dispersed in organic solvent which can facilitate the function of thin film devices and secondly, such functionalization can be employed for establishing molecular specific interaction during sensing. There are some studies on LB films of chemically functionalized CNTs. The electrochemical and spectroscopic studies of those functionalized CNTs are reported. It will be interesting to study the role of some ionic surfactants and biomolecules with functionalized CNTs at A/W interface. To understand the interaction between ions and functionalized CNTs, different microscopy and spectroscopy can be used. Using QCM, sensing applications of such LB films can also be investigated.

In chapter 4, We report a stable LF of ODA–SWCNTs. The LB films of ODA–SWCNTs are fabricated onto the quartz crystal wafers of a QCM and are employed for sensing the biological analytes *viz.* L–aspartic (L–asp) acid and bovine serum albumin (BSA) protein. The sensing performance of the LB films of ODA–SWCNTs is compared with that of thin film of randomly oriented ODA–SWCNTs obtained through spin coating technique. The sensitivity of the analytes using LB film is found to be far better than that of spin coated film of ODA–SWCNTs. The highly oriented CNTs in the LB films may create large surface density of adsorption sites which support the further growth of the nucleates sites into bigger domains. This in turn yield better performance and high sensitivity of the analytes by the LB films.

In chapter 5, we studied the LM and LB films of the cationic surfactants. We formed the LB films of dioctadecyl ammonium bromide (DOAB) and studied the DNA sensing application. The lowest detectable concentration of DNA in the liquid is found to be 20 fM. We have demonstrated the interaction of cationic surfactant with functionalized SWCNTs. PEG–SWCNTs is immobilized with the monolayer of cationic dioctadecylamine (DODA) by electrostatic interaction at A/W interface. Ultrathin films of PEG–SWCNTs/DODA have been deposited onto gold deposited quartz crystal. The interaction of DNA and PEG–SWCNTs/DODA mixed LF is studied using QCM, whose morphological features are visualized by AFM. The DNA sensing studies of LB films of DODA/PEG– SWCNTs indicate that the lowest detectable concentration of DNA in aqueous medium is $\sim$3 fM which is far lower than that of the LB film of DOAB.

The unique physicochemical properties of graphene has made it an attractive candidate for sensor applications. Graphene can be functionalized by covalent, non covalent and also other methods, which meet the specific requirments of different kind of sensors. There are some studies on carboxylic acid functionalized graphene as biosensor for simultaneous determination of Adenine and Guanine in DNA [124]. In a report, thin films of GO are studied using QCM [123]. GO thin film exhibits an excellent humidity sensing performance.

It will be interesting to study the sensing applications of LB films of G–COOH using QCM and sensing performance can be compared with spin coated films of G–COOH. Ultrathin films of functionalized graphene can be utilized in fabrication of different kind of chemical and biological sensors.

In chapter 6, we discuss the formation and characterization of LF and LB films of G–COOH. The LF of G–COOH at the A/W interface is found to be very stable and reversible. The functional layers of G–COOH were formed over the quartz crystal wafers by LB and spin coating techniques, and employed for sensing urea in aqueous medium. The response is found to be linear in the given concentration range. The lowest detectable concentration of urea in water by LB film was found to be very low (8.32 μM). The sensing performance of LB film of G–COOH is found to be better than that of spin coated film of G–COOH. The detection of urea in milk sample using the functional layers of G–COOH is also studied. The study on sensing of urea in milk sample indicate that the LB film of G–COOH can be employed for sensing urea even in the presence of different other species in the aqueous medium.

In summary, we developed the protocols to control the nanostructure in the thin films by fabricating LB films of CNTs and graphene with different functional groups on a variety of substrates under extremely controlled experimental conditions. The developed protocol for aligning CNTs and graphene will be useful for device applications.

Chapter 2

Langmuir and Langmuir–Blodgett Films of Single–Walled Carbon Nanotubes

2.1 Introduction

The fields of nanoscience and nanotechnology have grown remarkably after the realization of extraordinary electrical, mechanical, and thermal properties of carbon nanotubes (CNTs). The CNTs are highly anisotropic materials which exhibit exceptionally high anisotropy in electrical and optical properties [83, 125–127]. CNTs need preferential alignment onto solid surfaces for some device fabrication. Therefore, it is essential to control the alignment of CNTs onto the surfaces so that the properties of the fabricated device can be optimized for their best performance [128–131]. The CNTs can be aligned onto the surfaces by various techniques. Langmuir–Blodgett (LB) technique is the most promising one as it provides a control over the ordering of the CNTs during the deposition, the thickness of the film, and a control over tuning the functionality of the films [35]. In order to fabricate LB films, it is essential to obtain a stable Langmuir film (LF) of the material [132]. The stability of the LF primarily depends on the amphiphilic nature of the molecules, and it demands a proper balance of hydrophobicity and hydrophilicity of the molecules [21]. Nonetheless, there are several reports indicating a stable LF formed by pure hydrophobic materials [133–135]. Numerous reports also indicate stable LF of hydrophobic polymers [136, 137]. Such systems attain stability due to entropic reason. There are several reports on stable LF exhibited by hydrophobic nanoparticles at the air–water (A/W) interface [84–88]. Such systems can attain stability due to a balance between the attractive van der Waals interaction and steric repulsion between the particles. There are a few reports on the studies of LF and LB films of chemically modified CNTs or CNTs mixed with some stabilizer like polymers and surfactants [70, 72, 115, 138, 139]. There are few attempts [117, 140] for the formation of LF and LB films of pure CNTs; however, the stability of such films is hitherto unaddressed.

In this chapter, we report the formation of a stable and reversible LF of bundles of single–walled carbon nanotubes (SWCNTs) at the A/W interface. We transferred the LB films on conducting indium tin oxide deposited glass (ITO) substrates at different target surface pressures (π_t) and characterized the films using an atomic force microscope (AFM) in spreading resistance imaging (SRI) mode. We found a significant effect of target surface pressure of deposition on the morphology of the SWCNTs in the LB films. We obtained a supramolecular assembly of the SWCNTs in the LB films deposited in the liquid like phase of the LF.

2.2 Experimental methods

2.2.1 Langmuir and Langmuir–Blodgett Film

The SWCNTs are purchased from Carbon Solutions Inc, USA. The product is in the pristine state and is used as procured. We have characterized the material using Fourier transform infrared (FTIR) spectroscopy and found the material to be free from any other organic functional groups like carboxylic and amide groups. As the CNTs can be dispersed easily in dimethylformamide (DMF) solvent [112, 141], a solution of concentration 8800 μg/ml of the SWCNTs is formed in high performance liquid chromatography (HPLC) grade DMF. A solution of uniformly dispersed SWCNTs is obtained by ultrasonicating the SWCNTs–DMF solution for about an hour. The photograph of the solution of dispersion of SWCNTs is shown in Fig.2.1. The image clearly shows a homogeneous dispersion of SWCNTs.

The LF of SWCNTs is formed in a LB trough by spreading 2,650 μl of the solution very slowly using a microsyringe onto ultrapure ion free water subphase. About one

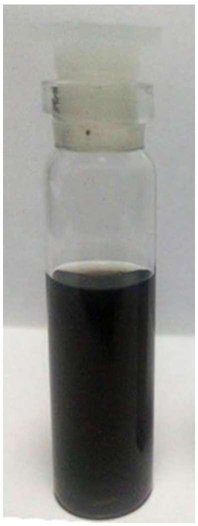

FIGURE 2.1: Soultion (concentration of ∼0.3 mg/ml) of SWCNTs uniformly dispersed in HPLC grade DMF.

hour is allowed for the solvent to evaporate from the water subphase leaving behind the dispersed SWCNTs. The surface pressure (π) – area per μg (A_w) isotherm of SWCNTs is recorded by compressing the film of SWCNTs symmetrically using the two barriers of the LB trough and recording the surface pressure simultaneously using an integrated balance. We spread the pure DMF solvent onto the water subphase and recorded the isotherms after one hour. The isotherm indicated negligible change in the π value. Such measurement ensures negligible effect of DMF solvent on the isotherm of the SWCNTs [142]. The stability of the LF of the SWCNTs is studied by recording isocycles during repeated compression and expansion of the film. The isocycles of LF can be obtained by repeated compression and expansion of the monolayer. Negligible hysteresis and retraceable isocycles indicate stable and reversible phases of the LF. The shift in the isocycle curves towards the lower or higher $\mathrm{A_w}$ indicate unstable LF. The instability may arise due to dissolution of the molecules or the formation of irreversible aggregates on the water surface. The LF of SWCNTs is transferred onto ITO substrates by LB technique. The ITO substrates were procured commercially and used after cleaning them thoroughly by ultrapure ion–free water, absolute alcohol, and HPLC grade chloroform, successively. The substrates were dried by blowing hot air at about 60° C. Prior to the LB deposition, the LF of SWCNTs is compressed to a π_t, and a time of 20 min is allowed to equilibrate the film. The single layers of LB films are deposited at different values of π_t by a single upstroke motion of the dipper at a speed of 5 mm/min. The transfer ratio for LB deposition on ITO substrates was found to be 1±0.2. The thickness of the LB films were measured using an ellipsometer (Laser Pro) equipped with 535 nm laser at a fixed angle of incidence, 70°. The thickness was measured at several places of the films, and the average thickness was calculated. The average thickness of the LB films deposited at $\pi_t = 0.5$ and 6 mN/m was obtained as 30 and 110 nm, respectively.

2.2.2 Atomic Force Microscopy

The LB films deposited onto ITO substrate were transferred to the scanning stage of the AFM, and the films were scanned in the SRI mode [102]. The films were scanned using diamond–coated conducting tips (DCP series, NTMDT) having the spring constant ~8 N/m. A bias voltage of 0.5 V was applied between the tip and the sample. The topographic and tunneling current maps were obtained simultaneously. The localized current–voltage (I–V) measurement is performed by positioning the conducting AFM tip at the desired part of the nanostructures and applying voltage between the tip and sample. The tip is positioned by choosing a constant force and retaining the feedback on so as to maintain a constant tip–sample separation for all the I–V measurements. All the experiments were carried out in ambient at room temperature ~22°C.

2.3 Results and discussion

2.3.1 Surface Manometry

The surface pressure (π) – area per μg (A_w) isotherm of the LF of SWCNTs at the A/W interface is shown in Fig.2.2. The isotherm indicates zero surface pressure at very large A_w. This is a gas–like phase of the LF of the SWCNTs. On reducing the A_w by compressing the film, the surface pressure started rising sharply at around 24 cm^2/μg. This is the onset of a liquid–like phase. On further compression of the monolayer of SWCNTs, a change in slope is observed at 15 cm^2/μg. The surface pressure keeps rising till the film is compressed completely in the trough. The change in the slope at 15 cm^2/μg can be considered as a collapse of the LF of SWCNTs. The collapse surface pressure is obtained as 11 mN/m. Unlike the case of sharp collapse of stearic acid [143] or plateau type collapse of octyl cyanobiphenyl [1], here the collapse is indicated by a slow change in the slope. The surface pressure increases monotonically thereafter.

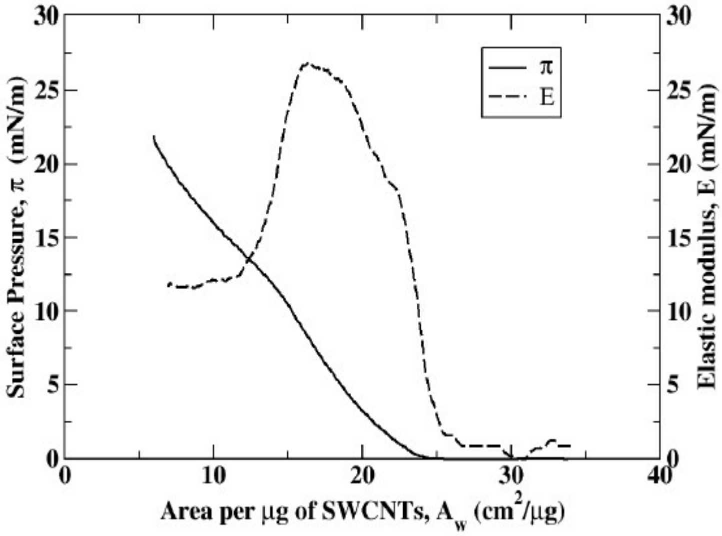

FIGURE 2.2: Surface pressure (π) – area per μg (A_w) isotherm of the LF of SWCNTs at the A/W interface. The isothermal in–plane elastic modulus (E) is shown by the dashed line.

The slow collapse may arise due to a transformation of 2–dimensional (2D) film to 3–dimensional (3D) structure with random entanglement of the SWCNTs.

The isothermal in–plane elastic modulus (E) is an appropriate quantity not only for distinguishing weak phase transition but also for quantification of the elasticity in a particular phase of LF [144]. The E of the LF can be calculated employing the Eq.2.1,

$$E = -A_w \frac{d\pi}{dA_w} \tag{2.1}$$

The E versus A_w of the LF of SWCNTs is shown in Fig.2.2. The E values remain very low for the larger value of A_w (*i.e.*, gas–like phase) whereas it increases rapidly at the onset of the liquid like phase. The maximum value of E (Ep) in the liquid–like phase is obtained as 27 mN/m. Such Ep value lies within the range of the liquid phase of LF of some reported hydrophobic polymers [136].

The stability of the LF of SWCNTs is studied by compressing and expanding the film repeatedly and recording the corresponding surface pressure. The isocycle measurement of the SWCNTs system indicates negligible hysteresis (Fig.2.3). In the isocycle measurement, the expansion curve almost follows the compression curve. During expansion, the zero surface pressure is attained at very large A_w. This indicates that

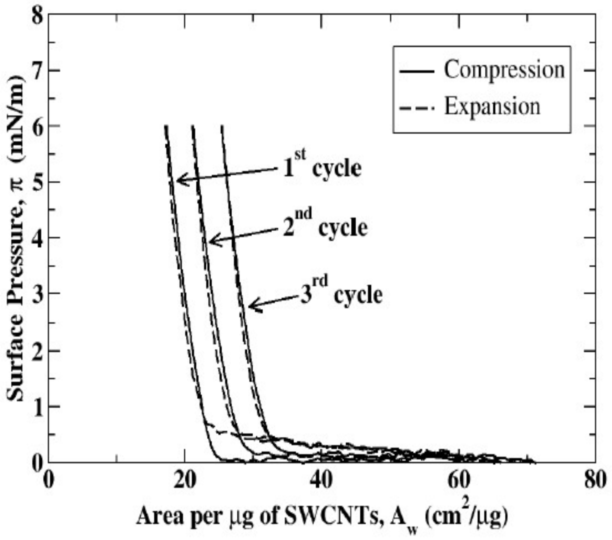

Figure 2.3: The isocycles of the SWCNTs at A/W interface. For visual clarity, the curve for 2nd and 3rd cycles are shifted toward right by an amount 4.3 and 8.6 $\mathrm{cm}^2/\mu\mathrm{g}$, respectively with respect to the curve representing 1st cycle.

though the liquid–like phase is completely reversible, the gas phase appears at very large A_w during the expansion of the film of SWCNTs. The isocycle measurement indicates not only a reversible but also a stable LF of the SWCNTs at the A/W interface. The SWCNTs chosen for our studies are pristine in nature and do not possess any polar functional group. There are numerous reports where a non–polar and purely hydrophobic nanomaterials form a stable LF at the A/W interface [84–88]. Such film stabilizes due to a balance between the attractive van der Waals interaction and steric repulsion between the hydrophobic units. Similarly, the stability of LF of SWCNTs at the A/W interface might be due to the balance between van der Waals attraction and steric repulsion between the SWCNTs.

2.3.2 AFM Characterization

The morphology of such LB films of SWCNTs was studied using AFM. The LB films of SWCNTs are deposited on ITO substrates at different value of π_t and scanned using AFM in SRI mode. The working principle of SRI mode in AFM is shown in Fig.2.4. In SRI mode, a conductive AFM probe scans the sample while in contact with the surface maintaining a constant force between tip and sample. A bias voltage is applied to the conductive AFM probe and recording of current flow between the tip and the sample are perfomed as a function of tip position on the surface. Therefore, SRI mode provides an insight of not only the topographic information of the sample but also local conducting nature of the films, simultaneously [102].

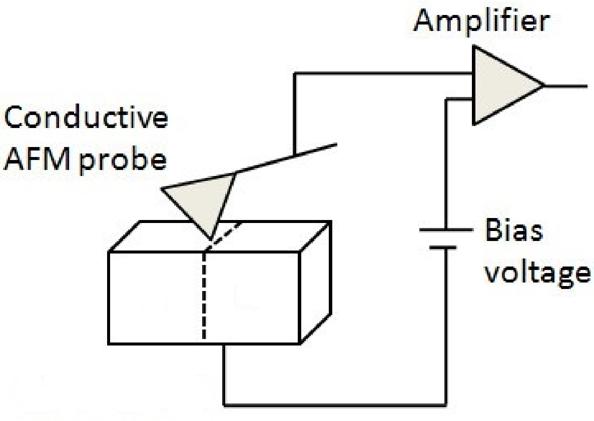

Figure 2.4: The schematic diagram of working principle of SRI mode in AFM.

ITO surface have its own characteristic and specific features. The topographic images of the ITO substrate obtained using AFM in contact mode is shown in Fig.2.5. The image shows granular texture. The image indicates the size of the ITO domain to be in the range of 150–250nm. The average height of ITO domains was found to be around 16 nm.

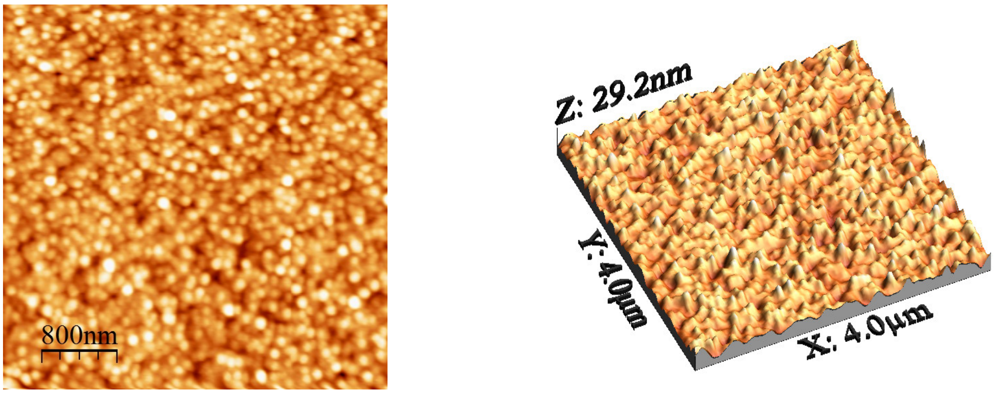

(a) (b)

Figure 2.5: Topographic image of ITO substrate (a) 2D and (b) 3D representation.

The SRI mode image of the ITO substrate is shown in Fig.2.6. The topographic image of the ITO substrate (Fig.2.6(a)) shows large domains. However, the tunneling current image (Fig.2.6(b)) is featureless, and it shows predominantly bright region with a little variation in the grayscale values. The LB films of the SWCNTs are deposited onto the

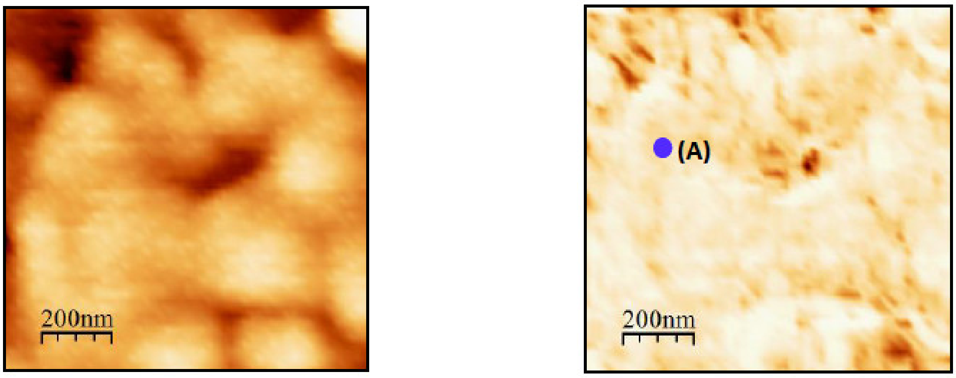

(a) (b)

Figure 2.6: SRI mode images of the ITO substrate. (a) Topographic image and (b) Tunneling current image. The bias voltage maintained during the scanning was 0.5 V. The blue dot in the image (b) represents the position where current– voltage (I–V) measurement has been carried out.

ITO substrates at the π_t = 0.5, 2, and 6 mN/m. The SRI mode images of such LB films of SWCNTs are shown in Fig.2.7 and Fig.2.8.

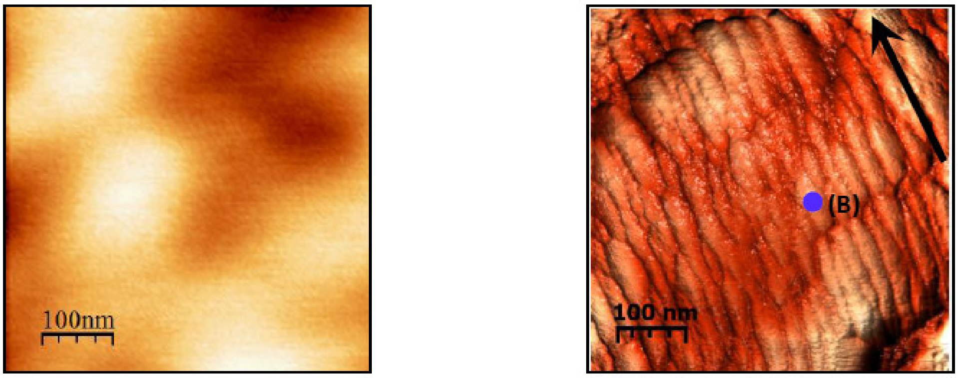

(a) (b)

Figure 2.7: (a) Topographic image and (b) Tunneling current image of the LB film of SWCNTs deposited on ITO substrate at a π_t = 0.5 mN/m. The images are scanned in SRI mode of the AFM. The bias voltage was maintained at 0.5 V. During LB deposition, the dipping direction of the ITO substrate is indicated by the black arrow in image (b). The blue dot in the image (b) represents the position where I–V measurement has been carried out.

The topographic image (Fig.2.7(a)) of the LB film of SWCNTs deposited at the π_t = 0.5 mN/m shows featureless texture. The hump in the image may be due to the underlying feature of the ITO domains. The tunneling current image (Fig.2.7(b)) shows long–oriented rod–like feature. The width of the rods varies from 20 to 35 nm. These are the bundles of SWCNTs which are oriented with their long axis parallel to the substrate dipping direction during LB film fabrication.

The LB films deposited at $\pi_t = 2$ and 6 mN/m are shown in Fig.2.8. The topographic images (Fig.2.8(a) and (c)) of the LB films of SWCNTs deposited at 2 and 6 mN/m indicate blob–like texture. Interestingly, the corresponding tunneling current images (Fig.2.8(b) and (d)) reveal the SWCNTs which are coiled to form donut structures. The hole in the donut can be considered as nanopore. This supramolecular assembly of the SWCNTs is observed in the LB films deposited in the liquid–like phase of the LF onto the ITO substrates. This assembly of the SWCNTs is independent of π_t provided the LB deposition is done in the regime of liquid–like phase of LF of the SWCNTs.

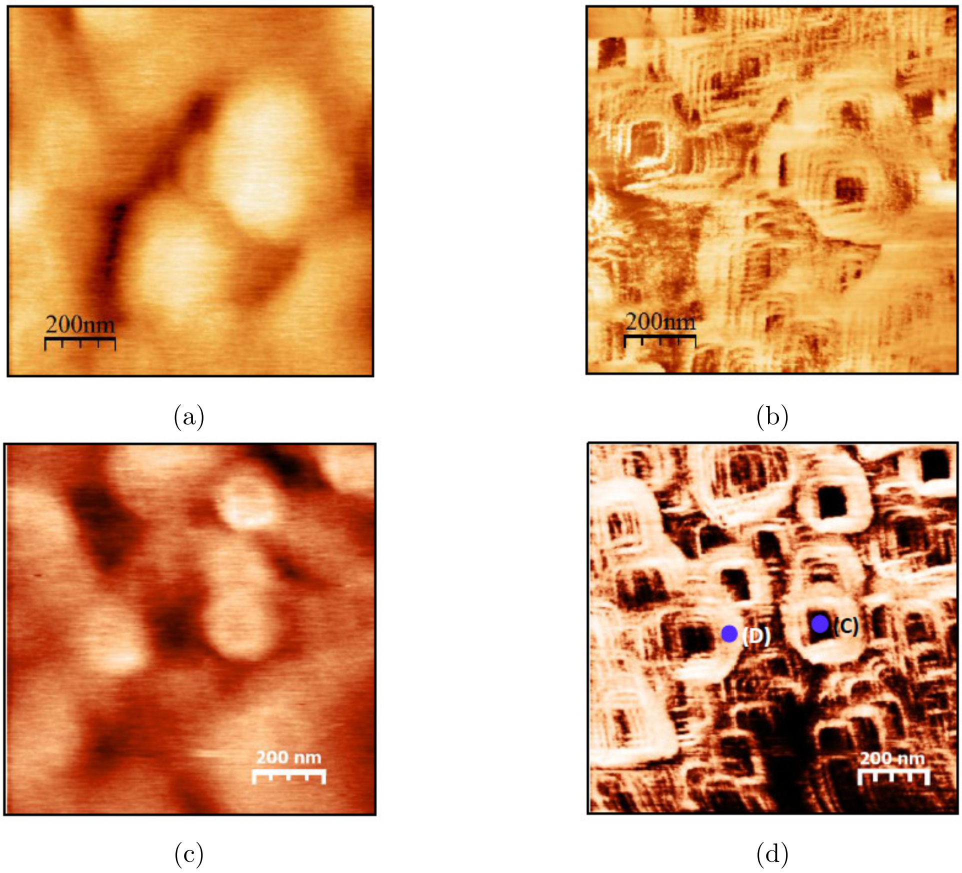

(a) (b) (c) (d)

FIGURE 2.8: (a) and (b) are the topographic and the corresponding tunneling current image of the LB film of the SWCNTs deposited at surface pressure 2 mN/m, respectively. (c) and (d) are the same obtained for LB film deposited at the $\pi_t =$ 6 mN/m. The images are scanned in SRI mode of the AFM. The bias voltage was maintained at 0.5 V. The blue dots in the image (d) represent the positions where I–V measurements have been carried out.

The topographic images could not able to resolve the bundles of SWCNTs because of the long range van der Waals interaction of the tip and the sample. The tunneling images reveal the presence of SWCNTs as the tunneling current is very sensitive to small perturbation due to change in local curvature and hence the local electronic state of the sample. A careful observation of the topographic images (Fig.2.8(a) and (c)) shows very low resolving edges of the blob structures. A 5x5 μm^2 tunneling current image (Fig.2.9) of the LB films deposited at $\pi_t = 4$ mN/m shows the presence of large number of donuts and nanopores distributed over the entire area. In an earlier report, Martel *et al.* [145] have found that SWCNTs can coil up and form rings. Using a simplest model, they have suggested that coiling involves significant strain energy due to the increased curvature, but the van der Waals interaction alone stabilizes the coil–structure.

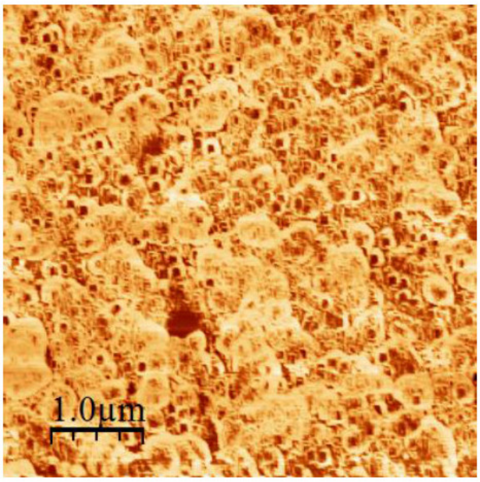

FIGURE 2.9: Tunneling current image of LB film of SWCNTs deposited at $\pi_t = 4$ mN/m obtained in SRI of AFM.

When the film of SWCNTs at the A/W interface is compressed, the possibility of interaction sites for van der Waals attraction increases. Therefore, a large number of SWCNTs can coil up to form donut structure all over the region of the LB film. A high resolution image revealing the internal features of the SWCNTs is shown in Fig.2.10(a). The figure clearly indicates that each of the SWCNTs is composed of thin tubes which wind themselves to form the bundle. A black line is drawn on a bundle, and the corresponding profile is shown Fig.2.10(b). The average width of the thin tubes is ~3 nm which is similar to the width of a SWCNTs. Therefore, these thin tubes are the individual nanotubes which wind to form the bundles. These bundles form supramolecular assembly in the LB films deposited in the liquid–like phase of the LF. The supramolecular assembly of SWCNTs was found only on the ITO substrate. The surface morphology and the roughness of the ITO substrate may have role in such assembly. The morphology of the SWCNTs in the LB film deposited onto smooth substrates *viz.* silicon wafer and mica was found to be aligned bundle of SWCNTs.

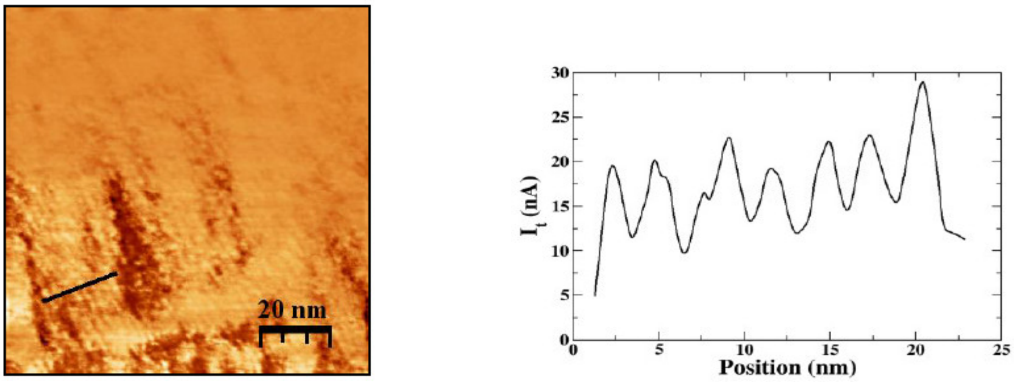

(a) (b)

FIGURE 2.10: (a) A high resolution current image of the LB film of SWCNTs deposited at π_t = 2 mN/m. (b) Line profile corresponding to the black line drawn across a SWCNTs bundle as shown in (a).

2.3.3 Tunneling Spectroscopy

Tunneling spectroscopy as a function of the bias voltage, i.e., I–V curves, provides very important information about the surface electronic structure, such as the local density of states of the sample. In tunneling spectroscopy, for a given tip–sample separation, the tunneling current (I) is continuously recorded by varying bias voltage (V), generating a tunneling conductance or I–V curve. Tunneling spectroscopy (I–V curve) focuses on the differential tunneling conductance which gives information about the conduction phenomena of the material [146].

The differential conductance (dI/dV) curves of the ITO substrate and the various local nanostructures obtained in the LB films of the SWCNTs are shown in Fig.2.11. The corresponding I–V curves are shown in the inset of Fig.2.11. The I–V curve corresponding to the ITO (A) shows the normal metallic behavior. The current rises sharply with the application of the voltage. It shows a non–zero differential conductance of about 110 nA/V at zero applied voltage. The I–V curve corresponding to the LB film deposited at π_t = 0.5 mN/m (B) shows a semi–metallic nature. The slope of the curve decreased drastically as compared to that of the ITO. However, there is non–zero differential conductance (∼15 nA/V) at zero applied voltage.

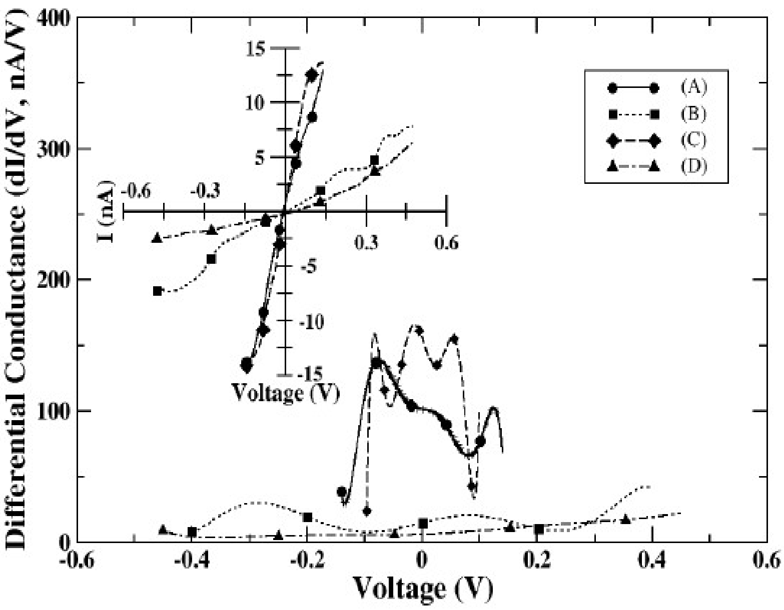

FIGURE 2.11: The differential conductance (dI/dV) vs applied voltage (V) curves. The corresponding I–V curves are shown in the inset. The curves A to D correspond to the reference points as shown by blue dots in the images of Fig.2.6b, Fig.2.7b and Fig.2.8d, respectively.

The I–V curve corresponding to the hole in the donut (nanopore) (C) exhibits similar behavior as compared to that of ITO. The differential conductance at zero applied voltage of the nanopore is about 150 nA/V. The donut structure shows an I–V curve (D) with a smaller slope. The differential conductance at zero applied voltage is 8 nA/V. Thus, the SWCNTs in the donut form exhibit semi–metallic nature. The LB films at the surface pressure higher than 0.5 mN/m exhibit the nanostructures possessing both the metallic (hole–region in the donut) and semi–metallic (donut) properties. Such supramolecular assembly composed of both metallic pores with semi–metallic boundaries can potentially be employed for various technological applications like fuel cells, photochemical cells, batteries, supercapacitors, and gas and biosensors.

2.4 Conclusion

Alignments of SWCNTs on solid surfaces are essential for some technological applications. Here, we have attempted to control the assembly of SWCNTs on solid substrate through LB deposition technique. We formed a stable and reversible LF of SWCNTs.

The LF exhibits gas like and liquid–like phase, and it collapses at $\pi_t = 11$ mN/m. The film is transferred to solid substrates by LB technique. The films are characterized using SRI mode of AFM. The film deposited at $\pi_t = 0.5$ mN/m shows the SWCNTs oriented along the preferential direction of deposition. The films deposited at surface pressures $\geq$2 mN/m shows SWCNTs forming a supramolecular donut structure. A high resolution image of the bundles shows a winding of the individual SWCNTs. Our studies indicate a dependence of SWCNTs alignment on solid support on the π_t during LB deposition. The I–V characteristic of LB films of SWCNTs deposited in liquid–like phase reveals metallic nanopores inside the semi–metallic donut. Such surface pressure–induced assemblies of SWCNTs on substrates have not been observed earlier. It will be very interesting to study the effect of alignment of SWCNTs on the performance of devices. In the next chapter we are presenting the effect of alignment of SWCNTs on the methane gas sensing and compared the results with that of random network of the SWCNTs in the thin film obtained using drop–casting method.

Chapter 3

Ultrathin Films of Single–Walled Carbon Nanotubes: A Potential Methane Gas Sensor

3.1 Introduction

In previous chapter, we have demonstrated that single–walled carbon nanotubes (SWCNTs) can form interesting mophologies onto solid substrates as a function of target surface pressure (π_t) of Langmuir–Blodgett (LB) film deposition. It will be interesting to study the role of alignment of SWCNTs in the ultrathin film on some physical properties. In this chapter, we proposed a methodology to align SWCNTs onto interdigitated electrodes. We describe our study on methane gas sensing application of LB films of SWCNTs and compared the result with that of random network of SWCNTs film obtained through drop cast method.

Due to extraordinary electrical and mechanical properties of carbon nanotubes (CNTs), it is a potential material for numerous device applications. The CNTs can be used to fabricate functional thin films which can be employed for various industrial applications [147–151]. In general, the CNTs are chemically inactive [152]. However, the electronic properties of the CNTs can be altered significantly even by physisorption of the chemical species. Such unique properties of the CNTs made it viable for the sensing application. It is believed that the sensor technology based on CNTs will have high sensitivity, high selectivity, consume low power, be largely miniaturized and will be of low cost [153]. Sensors based on CNTs as the functional material has numerous advantages over the other inorganic materials like metal oxide semiconductors. The sensing capability of CNTs even at the room temperature is found to be significantly high, and therefore it is a promising candidate for employing as functional material for building room temperature sensor. Gas sensors based on carbon nanotubes field effect transistor (CNTFET) show remarkable sensing capability. However, the CNTFET based device normally requires longer times (in seconds) for the detection of the gas molecules [154]. The sensitivity of a device can be increased by increasing surface–to–volume ratio of the functional material and the number of interaction sites [155]. In the previous chapter, we have demonstrated that SWCNTs can form a stable Langmuir film (LF) at the air–water (A/W) interface. We transferred the LB film and obtained surface pressure depended interesting assemblies of the SWCNTs. Our studies further provide avenue to manipulate the assemblies by altering the experimental parameters. For some technological applications, it may be essential to align the SWCNTs on the active area of the device.

In this chapter, we demonstrate a control on the alignment of SWCNTs on the solid substrate during the ultrathin film fabrication by LB technique. Using a very simple mechanism during the LB deposition (Fig.3.1), the orientation of SWCNTs can be manipulated either parallel or perpendicular to the dipping direction. During the compression of LF of the SWCNTs on the surface of water, the SWCNTs can align

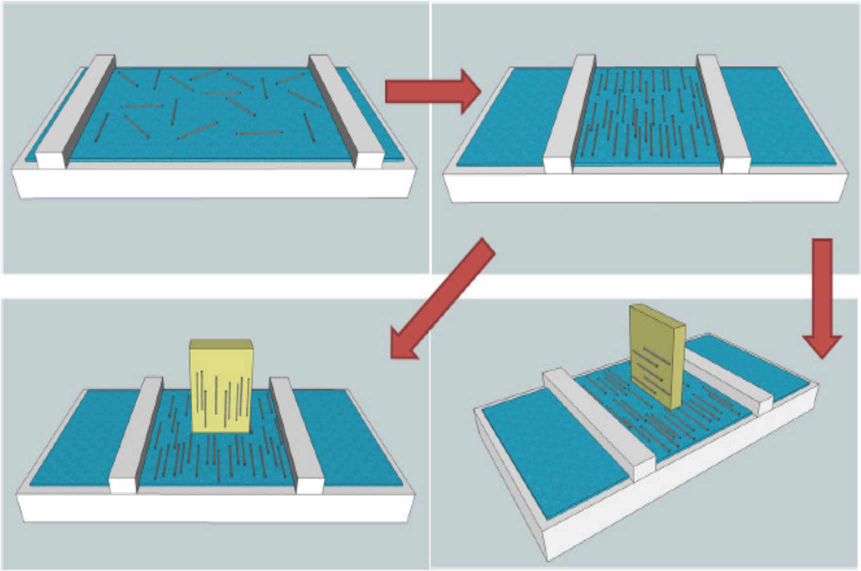

FIGURE 3.1: Mechanism for orienting SWCNTs during LB film deposition.

with their long axis perpendicular to the compression direction. Therefore, during LB deposition if the substrate plane is made parallel or perpendicular to the compression direction, the SWCNTs on the solid substrates will align with their long axis parallel or perpendicular to the dipping direction, respectively. The LB films with different orientation of SWCNTs are characterized by atomic force microscopy and current–voltage (I–V) measurements.

We have demonstrated the methane (CH_4) gas sensing capability of the aligned SWCNTs in the LB film at the room temperature. The sensing capability of the aligned SWCNTs in single layer of LB film of SWCNTs is compared with that of randomly oriented SWCNTs in the film grown by drop cast method. We found that the gas sensing capability of the LB film of SWCNTs is more efficient than that of the drop cast film. Furthermore, the sensitivity of the LB film is higher in humid condition as compared to that of dry environment. In this work, the lowest concentration (10 ppm) of the methane gas detected using the LB film of SWCNTs is much lower than its lowest explosive limit (*i.e.*, 50 ppm) [156–158].

3.2 Experimental methods

3.2.1 Langmuir and Langmuir–Blodgett Film

A solution of concentration 8.8 μg/ml of the SWCNTs (Carbon Solutions Inc, USA.) is formed in high performance liquid chromatography (HPLC) grade dimethylformamide (DMF) [112] and uniformly dispersed by ultrasonicating the SWCNTs–DMF solution for about an hour. The LF of SWCNTs was formed by spreading 2650 μl of the filtered solution very slowly using a microsyringe onto ultrapure ion–free water subphase. About one hour is allowed for the solvent to evaporate from the surface of the water leaving behind the dispersed SWCNTs. The surface pressure (π)–area (A) isotherm is recorded by compressing the monolayer of SWCNTs symmetrically using the two barriers of a LB trough and recording the surface pressure simultaneously using an integrated balance. Here, the A refers to area of the film at the A/W interface enclosed between the two barriers of the LB trough. The LF of SWCNTs is transferred onto different solid substrates by the vertically dipping mechanism of LB technique. A single layer of LB film was deposited onto interdigitated electrodes (IDE) for electrical characterization and oxidized silicon (Si/SiO_2) substrates for CH_4 gas sensing. The

LB films were deposited at a target surface pressure (π_t) of 6 mN/m corresponding to liquid–like phase of the LF. The drop cast films of SWCNTs were fabricated by spreading 50 μl of the solution of SWCNTs (0.086 mg/ml) onto the Si/SiO$_2$ substrate (area ∼1 cm^2) and allowing the solvent to evaporate completely from the surface. The thickness of the LB and drop cast films were measured using an ellipsometer (Laser Pro) equipped with 535 nm laser at a fixed angle of incidence, 70°. The value of thickness was measured at several places of the films and the average thickness was calculated. The value of average thickness of the LB and drop cast films of the SWCNTs were obtained as 30 and 2200 nm, respectively. All the experiments were carried out at room temperature ∼22° C.

3.2.2 Raman Spectroscopy

A single layer of LB film of SWCNTs transferred onto Si/SiO$_2$ substrate are characterized using Raman spectrometer equipped with 20 mW Ar$^+$ Laser as the excitation source. The Raman spectrum was also recorded for the bulk SWCNTs.

3.2.3 Atomic Force Microscopy

The surface topography of the LB films deposited onto Si/SiO$_2$ substrate was obtained by scanning the films using an atomic force microscope (AFM) in the contact mode. The films were scanned using silicon tips (CSG series, NTMDT) having the spring constant ∼0.1 N/m.

3.2.4 Field Emission Scanning Electron Microscopy

The surface morphology of the LB film and the dropcast film of SWCNTs deposited onto Si/SiO$_2$ substrate were obtained using a field emission scanning electron microscope (FESEM). The extra–high tension (EHT) voltage was maintained at 1–2 kV.

3.2.5 Electrical Characterization

The LB films were deposited in the liquid–like phase of the LF of SWCNTs on the IDE such that the long axis of the nanotubes is aligned parallel and perpendicular to the direction of the electric field applied to the IDE. The fabrication of IDE is discussed in chapter 1. For I–V characterization of the LB films, the voltage is applied across the gold pads of the IDE, and the corresponding current is measured using a Keithley source meter (model No. 2400). The relative permittivity for LB films with different orientational states of the SWCNTs was obtained using a model for Poole–Frenkel (P–F) conductivity. P–F conductivity normally occurs at high values of applied electric field and is related to a field–induced lowering of potential barriers within a material.

3.2.6 Kelvin Probe Measurement

The gas sensing of films of SWCNTs was measured for CH_4 using an Kelvin Probe (KP) based gas sensor characterization setup in CEERI, Pilani as shown in Fig.3.2. The KP technique measures the change in work function in terms of change in contact potential between the oscillating gold grid and the sensing layer. The contact potential difference between two metals is caused by their different work functions, which are energies needed to remove an electron from the metal surface. If two metals with different work functions are brought in contact, electron diffuses from the metal with lower work function to that with higher one. The electron transfer process stops once the electric field between them compensates for the work function difference. In this equilibrium state, the potential associated with the electric field exactly equals the work function difference, i.e. the contact potential difference (CPD), between the metals. The gold grid is not sensitive to the gas used, so it can be concluded that the signal represents the changes of the electronic structure of the sample under investigation.

V. Pentyala *et al.* [159] have investigated the gas sensing behavior of metal–organic frameworks (MOFs) materials (Mg– and Co–MOF74) towards CO_2, ethanol and acetone in humid air by means of work function based KP setup. Both MOFs show similar behavior for CO_2 sensing. The changes in CPD of 5–8 eV in positive direction were observed. Exposure to acetone exhibits nearly no changes in work function, whereas in case of ethanol the work function changes in the opposite direction. P. Davydovskaya *et al.* [160] have reported that copper 1,3,5–benzene–tricarboxylate (Cu–BTC) MOF layers can be used in work function based gas sensing devices for selective aldehyde sensing. Ethanal, propanal, pentanal and hexanal were used as target aldehyde gases. Work function measurements were performed using a KP setup. The humidity level

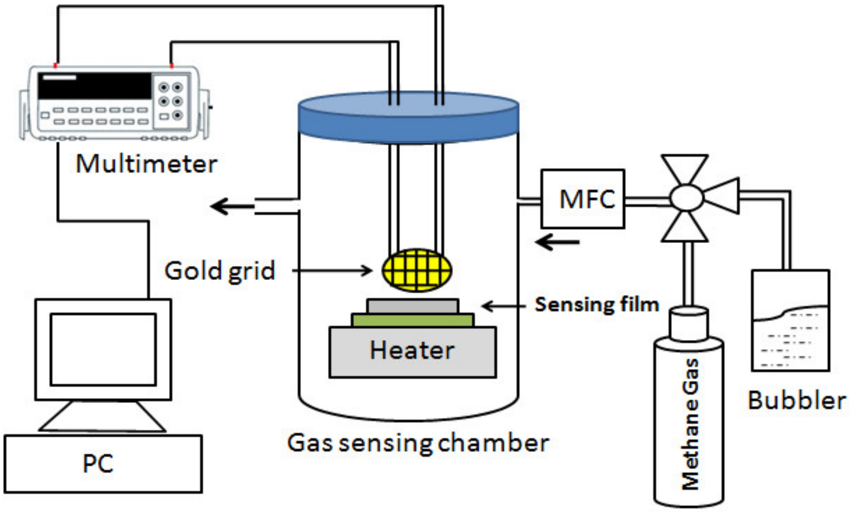

Figure 3.2: Kelvin Probe based gas sensor characterization setup.

has a strong influence on the sensing behavior. Increasing work function during exposure to pentanal with increasing humidity level indicate that water molecules have some role in the sensing layer–gas interaction.

In our study, the LB film deposited onto Si/SiO$_2$ was employed for CH$_4$ gas sensing and compared the result with that of random network of SWCNTs film obtained by drop cast method. The SWCNTs are p–type semiconducting material having the work function 4.8 eV [161]. The KP system provides information about a change in work function of sensing film upon exposure to ambient gas in process chamber. The system has provision to dilute the gas by mixing hydrocarbon free dry air with the help of mass flow controllers (MFCs). In addition, the ambient can also be made humid in a very controlled manner by passing the dry air through bubbler followed by MFCs. The complete characterization setup is interfaced with LabVIEW programme to acquire the CPD values. The CPD provides the information about the change in work function with respect to reference electrode. The change in CPD upon exposure to gas indicates the sensitivity of film. Responses were acquired for different concentrations of the gas (10 ppm, 30 ppm and 50 ppm) at the room temperature. An exposure time of 10 minutes was given to all experiments. The signals were recorded as CPD between gold grid and the films of SWCNTs deposited onto Si/SiO$_2$ substrate. The CPD values for the Si/SiO$_2$ substrate were found to be negligible under the exposure of CH$_4$ and water molecules.

3.3 Results and discussion

3.3.1 Surface Manometry and AFM/FESEM Characterization

In the previous chapter, we have found that the LF of SWCNTs at A/W interface to be stable and reversible. The π–A_w isotherm of the LF of SWCNTs at A/W interface is shown in Fig.2.2. The film exhibited gas–like phase, liquid–like phase and collapse.

The topographic images of the Si/SiO$_2$ substrate is shown in Fig 3.3. Figure shows the 2–dimensional (2D) and 3–dimensional (3D) representation of Si/SiO$_2$ surface. AFM images of Si/SiO$_2$ substrates reveal that Si/SiO$_2$ substrate exhibits smooth and uniform surface. The average height of grain was found to be around 1.6 nm.

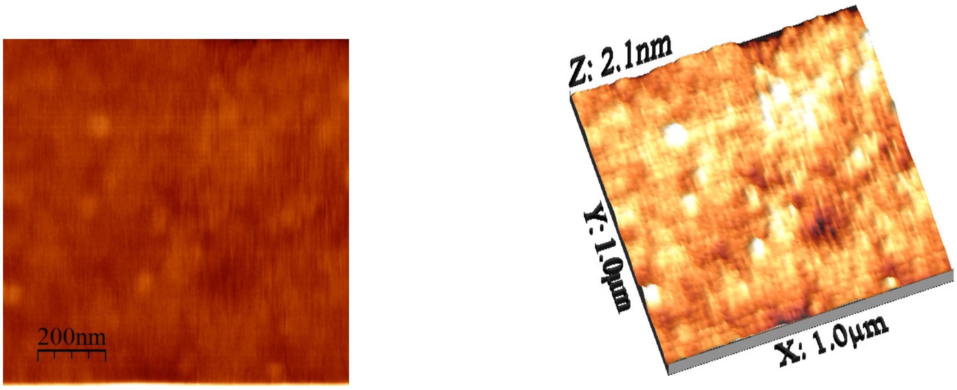

(a) (b)

FIGURE 3.3: Topographic image of Si/SiO$_2$ substrate (a) 2D and (b) 3D representation.

A single layer of LB film of SWCNTs at π_t = 6 mN/m is transferred on Si/SiO$_2$ substrates. The surface topography of the LB films was obtained by scanning the film using AFM in contact mode. Fig.3.4 shows the AFM images depicting the surface topography of the single layer LB film of SWCNTs deposited in the liquid–like phase onto the solid Si/SiO$_2$ substrate. The AFM images show the bundles of SWCNTs aligned along the dipping direction during the deposition of LB film on the substrate. This indicates that the SWCNTs in a functional thin film can be aligned in a preferred direction on the 2D surface by employing LB deposition technique. The width of the bundles is found to be 20–30 nm.

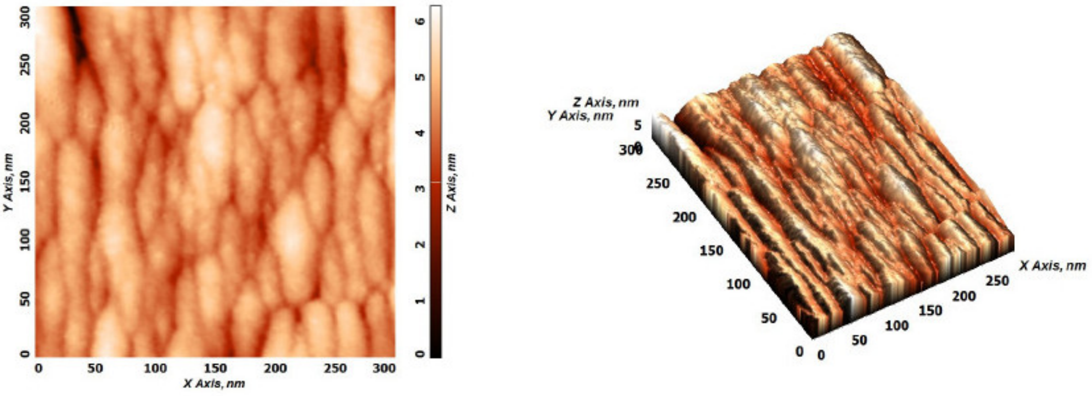

(a) (b)

Figure 3.4: AFM image of the LB film of SWCNTs deposited onto Si/SiO$_2$ substrate in liquid–like phase with (a) 2D (b) 3D representation. The dipping direction is along the y–axis.

The FESEM images of the LB film and the drop cast film are shown in Fig.3.5. The FESEM image (Fig.3.5(a)) of the drop cast film deposited onto Si/SiO$_2$ substrate shows the random network of the bundles of nanotubes. However, surface morphology of the LB film of SWCNTs shows the aligned nanotubes which are aligned on an average to a particular direction.

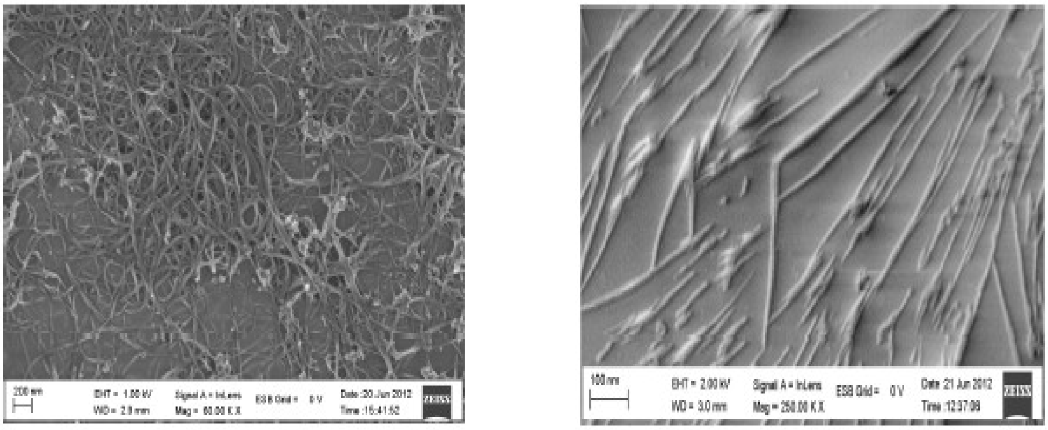

(a) (b)

Figure 3.5: FESEM images of (a) drop cast films and (b) LB film of SWCNTs deposited onto Si/SiO$_2$ substrates.

3.3.2 Raman Spectroscopy

The Raman spectrographs of LB film of SWCNTs and bulk SWCNTs deposited on Si/SiO$_2$ substrates are shown in Fig.3.6. The Raman spectrum of the bulk sample of SWCNTs shows the characteristics modes of SWCNTs, *e.g.*, D, G, and radial breathing mode (RBM) at 1,592, 1,350, and 164 cm^{-1}, respectively. The Raman spectrum of the single layer of LB film of SWCNTs exhibits all the characteristic Raman modes as observed in the bulk sample. Apart from the characteristic modes, the spectrum reveals strong peaks corresponding to the silicon substrate at 520 cm^{-1}. The peak corresponding to Si–O–Si is observed at 972 cm^{-1}. The presence of the characteristic Raman modes ensures the existence of SWCNTs in the single layer of LB film.

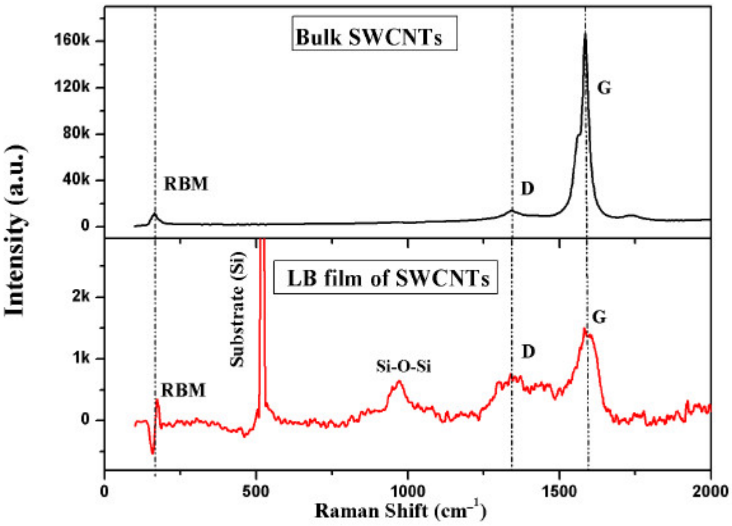

FIGURE 3.6: Raman spectrographs of the bulk sample of SWCNTs and LB film of SWCNTs deposited onto Si/SiO$_2$ surface at a $\pi_t = 6$ mN/m. The characteristics G, D, and radial breathing mode (RBM) frequencies of the SWCNTs are observed at 1,592, 1,350, and 164 cm^{-1}, respectively and are indicated by the vertical dashed lines.

3.3.3 Electrical Characterization

The LB films with different orientational states of the SWCNTs are further characterized by I–V measurement. For such characterization, the LB films are deposited with long axis of SWCNTs either parallel or perpendicular to the direction of the electric field applied by the IDE. The I–V measurements were performed at room temperature to evaluate the electrical behavior of the LB films of SWCNTs. In this experiment, the IDE gap was taken to be 10 μm, which is greater than the length of an individual SWCNTs. Conducting pathway between two electrodes must therefore consist of several interconnected bundles of SWCNTs spanning the gold electrodes. When an electric field is applied, the trapped charge can enter the quasi–conduction band of SWCNTs by the P–F type of conduction mechanism, and flows from one electrode into the other [140]. This is a bulk–limited process operating at high electric fields in which the conduction is determined by charge traps. In the presence of an electric field, E, the energy barrier associated with the trapping centers is lowered. The standard quantitative equation for P–F conduction is given by

$$I_{\mathrm{PF}} = \mathrm{AE}exp\left[\frac{\beta_{\mathrm{PF}}\sqrt{\mathrm{E}}}{k_B T}-\phi\right] \tag{3.1}$$

where A is constant, ϕ is a constant related to the trap depth, T is temperature, k_B is the Boltzmann constant and β_{PF} is P–F constant which can be defined as

$$\beta_{\mathrm{PF}} = \sqrt{\frac{e^3}{\pi\epsilon_r\epsilon_0}} \tag{3.2}$$

Where e is the electronic charge, ϵ_r is the relative permittivity of the LB film of SWCNTs, ϵ_0 is the permittivity of the free space.

Fig.3.7 shows the I–V characteristic curves of the LB films with SWCNTs aligned parallel and perpendicular to the applied electric field. In the case of SWCNTs aligned parallel to the electric field (Fig.3.7(a)), the interconnected network or bundle of SWCNTs over the surface of electrodes provides a sufficient path for possible charge conduction. As a result, the variation in the current value with respect to the applied voltage for such type of orientation seems to be virtually linear. The corresponding I–V curve is fit with the P–F equation, and the value of relative permittivity is obtained to be around 39. If the long axis of the SWCNTs is aligned perpendicular to the electric field, the charge carriers find limited pathways for their conduction through the SWCNTs network. Hence, the I–V characteristic of such film shows a flat curve and the current rises only at higher applied voltages (Fig.3.7(b)). A fit to P–F equation yields the value of the relative permittivity to be around 2.4.

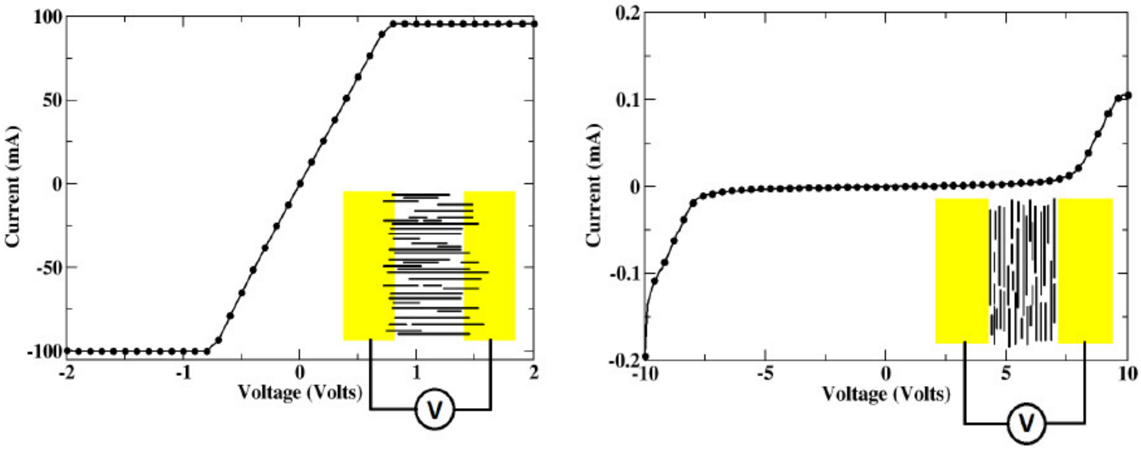

(a)

(b)

Figure 3.7: Current–voltage (I–V) characteristics of LB films of SWCNTs where long axis of the SWCNTs is aligned (a) parallel and (b) perpendicular to the direction of electric field, respectively. The yellow rectangular regions depict the gold electrodes of the IDE. The black rods between the electrodesrepresent the SWCNTs.

3.3.4 Methane Gas Sensing

It has been demonstrated by theoretical calculation and experimental observations [118, 147] that individual semiconducting SWCNTs or a mixture of metallic and semiconducting nanotubes shows a global p–type semiconducting behavior. Therefore, the charge conduction in such a system is guided by transport of holes through the material. The electrical properties of CNTs are very much sensitive to any charge transfer to it due to chemical/physical adsorption of molecular species. When the p–type semiconducting CNTs interact with the electron–donating molecules (*e.g.*, NH_3, water) or electron withdrawing molecules (*e.g.* NO_2, O_2, CH_4) a significant change in the density of main charge carriers (*i.e.*, holes) in the bulk of the nanotubes takes place, resulting into the changes in the work function of CNTs [115, 153, 162]. This electrical behavior is one of the basics for the development of CNTs based chemical gas sensors. The KP measurements on the LB film and drop cast film of SWCNTs on Si/SiO_2 are shown in Fig.3.8 (a) and (b), respectively.

The CH_4 gas is introduced in the chamber at the room temperature under the two different conditions; dry and with relative humidity equal to 50%. In an electrical transport measurement, it has been found that the conduction of the nanotubes is decreased on interaction with water molecules [163]. On interaction, the water molecules

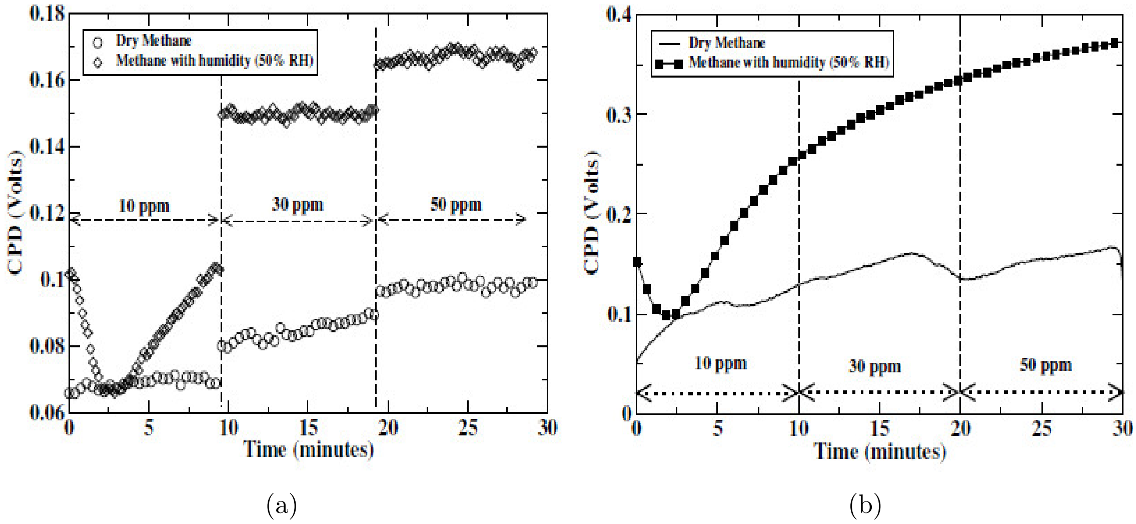

FIGURE 3.8: KP measurements at the room temperature on (a) LB film (b) drop cast film of the SWCNTs deposited on Si/SiO$_2$ substrates. The CPD value for the bare Si/SiO$_2$ substrate was found to be zero for all the concentrations of CH$_4$ in dry and humid environment.

donate electronic charge (0.03 e$^-$) to the nanotubes. This charge transfer due to water adsorption depletes the hole concentrations in the nanotubes, thereby reducing the conduction in the system [164]. Both the curves (curve (a) and (b) of Fig.3.8) corresponding to 10 ppm in the humid environment show an initial drop (upto ∼2–3 minutes) and then rise. The initial drop in the CPD values due to the introduction of water molecules in the process chamber is therefore, due to the depletion of hole concentration in the SWCNTs [164].

On the other hand, due to the weak acidic nature of CH$_4$, it can donate protons and increase the concentration of holes in the nanotubes on adsorption and thereby increases the CPD values. During the initial stage of insertion of water and CH$_4$ molecules in the chamber, the water molecules interact with SWCNTs rapidly. Therefore, the charge transfer to the nanotubes is dominated by its interaction with water molecules. This results in decrease in CPD values for the initial 2–3 minutes. However after 2–3 minutes, the charge transfer to the SWCNTs is dominated by its interaction with CH$_4$ molecules leading to an increase in CPD values.

Interestingly, the CPD values for the LB film of SWCNTs in dry and humid ambient indicate a systematic variation in data. The CPD value remains constant for a given concentration of the gas molecules (ppm level) in the chamber. However, there is an abrupt change (step like jump) in the CPD values on changing the ppm level of the gas molecules. Such response is an indicative for using LB films of SWCNTs as a potential CH_4 gas sensor. The discontinuity in the CPD values on the change of the gas concentration can be potentially employed for sensing the change in the concentration of the gas molecules in the ambient. It is noteworthy, that the jump in the CPD values due to the change in the gas concentration in the humid environment is much higher than that of the jump in the dry environment. Therefore, the CH_4 gas sensor based on the LB film of SWCNTs will be more sensitive in humid environment. The CPD values for the drop cast film in the dry environment indicate a small rise in the overall values even for the change in the gas concentration from 10 to 50 ppm. However, the variation does not indicate any systematic change in the values. Whereas, the CPD values rises monotonically with time (except the initial drop due to depletion of hole concentration by the adsorbing water molecules) on the insertion and increasing the ppm level of the gas molecules in the chamber in humid condition. The surface mass density of the LB film and the drop cast films were $5.64\text{x}10^{-5}$ mg/cm^2 and $4.33\text{x}10^{-3}$ mg/cm^2, respectively. If the CPD values are normalized with respect to the surface mass density of each of the respective films, the response of the drop cast films should be approximately 130 times greater than that of LB films. However, the raw CPD data variation (from Fig.3.8) indicates an increase in the CPD values of drop cast film is about 1.5 to 2 times greater than that of LB films. Therefore, the normalized response of the LB film of SWCNTs is much higher than that of drop cast film. In an earlier work, the random network of SWCNTs and carbon nanofibres were employed for the CH_4 gas detection [165]. The sensitivity of such sensor was reported to be varying with time. The sensor had attained maximum sensitivity for the detection of 3000 ppm of the gas very slowly (80 seconds).

Here, the response of the LB film of SWCNTs is rapid due to any change in the ppm level, and it remains invariant with time for the given concentration of the gas. The SWCNTs in the LB films are well aligned thereby the adsorption of CH_4 molecules on the preferential sites of the SWCNTs may also follow some alignment. Any change in the concentration of the gas molecules in the ambient increases the density of the adsorbed CH_4 molecules on the aligned SWCNTs giving rise to an abrupt change in the CPD values. On the other hand, the alignment of SWCNTs in the drop cast film is completely random, thereby creating random adsorption sites for the CH_4 gas molecules. The random adsorption of the gas molecules gives rise to increase in the overall CPD values, though step–like change in the values are not being observed on increasing the concentration of the gas molecules. These findings make the LB films of SWCNTs to be a potential CH_4 gas sensor whose sensitivity is larger in the humid environment.

3.4 Conclusion

In this chapter, we demonstrate a control on the alignment of SWCNTs on Si/SiO_2 substrate during ultrathin film fabrication by employing LB technique. The SWCNTs are aligned parallel and perpendicular to applied electric fields between the interdigitated electrodes, and the corresponding I–V curves are studied. The CNTs can be used for gas sensing and storage [166, 167]. We have studied the CH_4 gas sensing capability of LB films of SWCNTs at the room temperature, and it is compared with that of the film fabricated by the drop cast method. We found the LB films are very sensitive to a change in the concentration of the CH_4 molecules in the environment. We observed the sensitivity of the LB films to be significantly high in the humid environment than compared to dry environment. Such a behavior makes LB films of SWCNTs more viable for CH_4 gas sensing in the normal atmospheric condition which in general possesses finite humidity. The functionality of the CNTs based devices can be altered by the suitable chemical modification of the CNTs. Such chemical functionalization can not only facilitate film processibility but also provides specificity to a target analyte during sensing. In the next chapter we present our studies on the thin films of functionalized SWCNTs.

Chapter 4

Biosensing Properties of Langmuir–Blodgett Film of Octadecylamine Functionalized Single–Walled Carbon Nanotubes

4.1 Introduction

Carbon nanotubes (CNTs) are playing an increasingly important role in the development of numerous devices including sensors [168, 169]. The sensitivity and performance of the sensors are being improved by using organically functionalized CNTs. The high surface–to–volume ratio of the CNTs renders them as a useful candidate for the rapid detection of chemical or biological species even at very low concentrations. Thus, CNTs based biosensors are recognized to be a next generation building block for ultra–sensitive biosensing systems [170]. Many biological species, such as deoxyribonucleic acid (DNA), proteins and enzymes, have been immobilized onto CNTs either on their sidewalls or at the end–caps [171]. While the CNTs bioconjugates are functional materials essential for the development of advanced nanotube biosensors, the device fabrication process also plays an important role in regulating their biosensing performance [172]. Functionalized CNTs have many improved characteristics, such as large edge plane, high surface activity, high catalytic efficiency and better dispersibility in a host. Functionalized CNTs can improve the fixed efficiency of biological recognition of molecules (e.g. enzymes, DNA, antigen/antibody, etc.) in biosensors [173]. Many biological species such as nucleic acids, peptides, and proteins, can be non–covalently adsorbed on the CNTs surfaces through hydrophobic, π–π stacking, and electrostatic interactions [171].

Recently, Zhang *et al.* [174] have designed a sensitive DNA biosensor based on a glassy carbon electrode modified with multi–walled CNTs (MWCNTs), polydopamine (PDA), and gold nanoparticles (Au–NPs), for a sequence–specific DNA detection. The interface of Au–NPs/PDA/MWCNTs film sensor significantly enhances the performance of the electrochemical DNA biosensor. Proteins are the commonly used material for dispersing CNTs efficiently in aqueous medium. Iancu *et al.* [175] have utilized functionalized MWCNTs with serum albumin to detect liver carcinoma cells.

The immobilization of ligands during the development of a biosensor plays a crucial role for the stability, reproducibility and efficiency of the sensor. The stability of immobilized species onto a surface depends primarily on the molecule–substrate interaction. Such interaction can be studied systematically using a quartz crystal microbalance (QCM). In recent years, there has been a rapid growth in the number of scientific reports on sensing application using QCM. QCM is an analytical technique that provides in–situ analysis of interactions during the sensing process. The main advantages of sensing through QCM are high sensitivity, high stability, fast response and low cost. The widespread use of QCMs began when they were found to be applicable in liquid environments in around 1980 [176, 177]. Liquid phase application of QCM technology expanded the number of potential applications dramatically including biotechnology applications and in particular biosensing applications [178]. Nowadays, quartz resonators can be regarded as typical mechanical transducers for chemical and biological sensing devices that transform the change in mass due to the adsorption of the analytes into an electrical signal [179]. Detection of proteins and other biomolecules in liquid phase is the essence for the design of a biosensor. The sensitivity of a sensor can be enhanced by the appropriate functionalization of the sensing area so as to establish the molecular specific interaction. In an interesting work, Kaufman *et al.* [180] have described the adsorption characteristics of three proteins [bovine serum albumin (BSA), myoglobin (Mb), and cytochrome c (CytC)] onto self–assembled monolayer (SAM) of 11–mercaptoundecanoic acid (MUA) on both gold nanoparticles (AuNP) and gold surfaces (Au). BSA showed the highest affinity for the SAM of MUA on Au, forming an irreversibly adsorbed rigid monolayer.

Su *et al.* [181] have fabricated novel low–humidity sensors by in situ photopolymerization of polypyrrole /Ag/TiO_2 nanoparticles (PPy/Ag/TiO_2 NPs) composite thin films deposited on quartz crystal of a QCM. The sensitivity increased with the doping amount of TiO_2 NPs. Because of its high reliability, high stability, ease of surface coating, and nanogram scale sensivity, the QCM technique has increased interest both in liquid and gas phase applications.

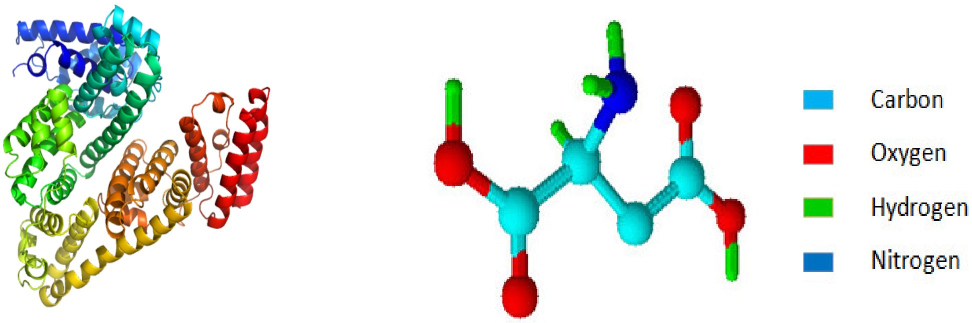

(a) (b)

FIGURE 4.1: Structure of (a) BSA (Appendix A) and (b) L–aspartic acid.

In the previous chapter, we found that the Langmuir–Blodgett (LB) thin film of pristine SWCNTs can be employed for methane gas sensing. The sensing capability of the LB film of SWCNTs was found to be remarkably enhanced as compared to that of drop casted film. The LB film offers a higher degree of ordering in the film architecture as compared to that of drop casted film. Such ordering in the LB films may have role in providing the enhanced performance of the sensing device. In order to employ the extraordinary physicochemical properties of SWCNTs for sensing applications, it is preferred to functionalize them organically. Such chemical functionalization is required for different reasons. Functionalization of the SWCNTs provide not only better dispersibility in a host but also creates avenues for establishing molecular–specific interaction which are essential for the development and performance of a sensor. In this chapter, we discuss our studies on the Langmuir film (LF) and LB films of octadecylamine functionalized single–walled carbon nanotubes (ODA–SWCNTs) at different interfaces. We also discuss our studies on the LB films of ODA–SWCNTs towards its sensing capabilities of biologically relevant species e.g. aspartic acid and BSA protein. Amino acids (AAs) are the building blocks of protein. The interaction between SWCNTs and AA is very important for understanding the interaction mechanism between SWCNTs and biomolecules [182, 183]. The molecular structure of BSA and L–aspartic (L–asp) acid are shown in Fig.4.1. The average size of L–asp acid is ∼0.7 nm and BSA protein is ∼8nm [184]. In order to understand the sensing of the BSA using QCM by a standard functional layer, the gold–coated quartz crystals were functionalized by forming SAM of MUA. The adsorption characteristics of BSA onto SAM of MUA on quartz crystal are studied. BSA showed the large affinity for surface treated with SAM of MUA as compared to pure gold surface. Thin films of the functional material exhibiting amine groups are of great interest for many applications because they are known to influence protein adsorption and provides sites for physical/covalent immobilization of biomolecules. The amine group of ODA–SWCNTs can provide molecular–specificity for attracting suitable analytes. Here, sensing layers of ODA–SWCNTs are fabricated using LB technique and spin coating method on QCM gold deposited quartz wafers. The LB film deposited onto quartz crystal was employed for detection of L–asp acid and BSA protein and compared the result with that of random network of ODA–SWCNTs film obtained by spin coating method. Our experimental results show that sensing capability of LB films of ODA–SWCNTs is more enhanced as compared to spin coated film.

4.2 Experimental methods

4.2.1 Lanmuir and Langmuir–Blodgett Films

The ODA–SWCNTs are purchased from Carbon Solutions Inc, USA. The MUA and L–asp acid were purchased from Sigma Aldrich and BSA was purchased from Merck.

A solution of concentration 0.03 mg/ml of ODA–SWCNTs is formed in high performance liquid chromatography (HPLC) grade chloroform. Uniformly dispersed solution of ODA–SWCNTs is obtained by ultrasonicating the solution for ∼30 minutes. The LF of ODA–SWCNTs was formed by spreading 700 μl of the solution very slowly using a micropipette (Tarsons) onto ion–free water subphase in a LB trough. About 30 minutes were allowed for the solvent to evaporate from the surface of the water leaving behind the dispersed ODA–SWCNTs. The surface pressure (π) – area (A) isotherm was recorded by compressing the monolayer of ODA–SWCNTs symmetrically using the two barriers of the LB trough and recording the surface pressure simultaneously using an integrated balance. Here, the area refers to area of the film at the air–water (A/W) interface enclosed between the two barriers of the LB trough. The LF of

ODA–SWCNTs is transferred after three isocycles onto quartz crystal wafers by the vertical dipping mechanism of LB technique. The LB films were deposited at target surface pressure (π_t) = 8 mN/m corresponding to liquid–like phase of the LF of ODA–SWCNTs. The spin coating was done by spreading 150 μl of ODA–SWCNTs solution in the HPLC grade chloroform solvent onto MUA functionalized quartz crystal. Deposition was done at a spinning rate of 2500 rotations per minute. The experiments were carried out at room temperature ($\sim$22^o C)

4.2.2 QCM Measurememts

The AT–cut gold–coated quartz crystals (SRS, USA) exhibiting a resonance frequency of 5 MHz were employed as the sensing element. The quartz wafer was cleaned in cold piranha solution (conc. H_2SO_4 : H_2O_2 as 3:1) and rinsed successively with plenty of ion–free water, alcohol and acetone. The quartz crystals were deposited with SAM by immersing them for 10 hours in freshly prepared 1mM pure ethanol solution of MUA. The modified crystals were removed from the solution and rinsed with ethanol to remove any unbound MUA molecules. BSA is a globular protein ($\sim$66,000 Da) typically around 583 AAs in length. The sensing of BSA in aqueous medium was studied by recording a change in piezoresponse using QCM (QCM200, SRS, USA). The sensing setup is shown in Fig.4.2. The functionalized quartz wafer is mounted in the QCM holder. The holder was vertically dipped into the beaker filled with 200 ml of aqueous medium. The ultrapure ion–free water having the resistivity greater than 18

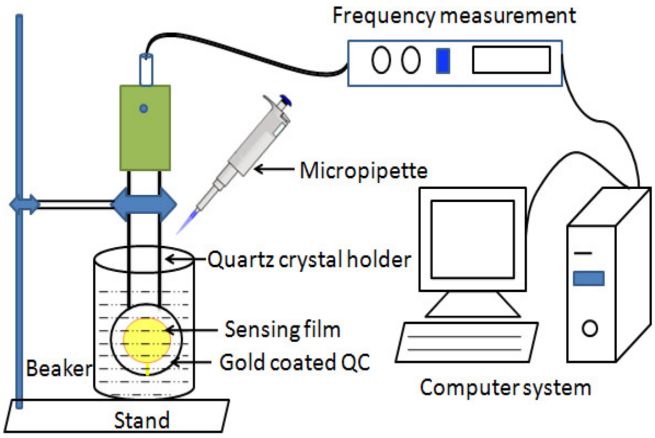

FIGURE 4.2: Quartz crystal microbalance sensing setup.

MΩ–cm was obtained from a Millipore (DQ–5) unit. Stock solution of BSA and L–asp acid was prepared in ultrapure water with a concentration of 10 mg/ml and 8.5mg/ml, respectively. The BSA solution was injected into the beaker through a micropipette and the change in frequency (△f) is recorded as a function of concentration of BSA.

4.2.3 Atomic Force Microscopy

The morphology of the films deposited over the crystal before and after adsorption of analytes were observed using an atomic force microscope (AFM) in contact mode (SolverPro, NTMDT). The samples were scanned using the silicon tip having the spring constant ∼0.2 N/m.

4.3 Results and discussion

4.3.1 Surface Manometry and Langmuir Blodgett Films

The surface pressure (π) – area (A) isotherm of LF of ODA–SWCNTs at A/W interface is shown in Fig.4.3. The isotherm indicates zero surface pressure at very large area.

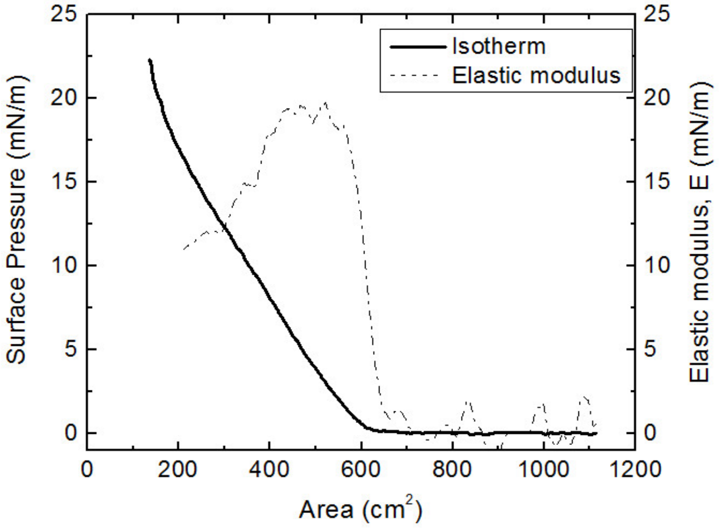

FIGURE 4.3: Surface pressure (π) – area (A) isotherms of Langmuir film of ODA–SWCNTs at A/W interface. The isothermal in–plane elastic modulus (E) is shown by the dashed line.

This is a gas–like phase of the LF of the ODA–SWCNTs. On reducing the area by compressing the film, the surface pressure started rising sharply at around 600 cm^2. This is the onset of a liquid–like phase. On further compression of the film of ODA–SWCNTs, a change in slope is observed at around 15 mN/m. The surface pressure keeps rising till the film is compressed completely in the trough. The slow change in the slope can be considered as a collapse of the LF of ODA–SWCNTs.

The isothermal in–plane elastic modulus (E) of LF can be calculated employing the relation Eq.2.1. The E versus A of the LF of ODA–SWCNTs is shown in Fig.4.3 (dashed line). The E values remain very low for the large area (*i.e.*, gas–like phase) whereas it increases rapidly at the onset of liquid–like phase. The maximum value of E in liquid–like phase is 19 mN/m. The LB film of ODA–SWCNTs is deposited onto quartz crystal wafers in liquid–like phase at π_t = 8 mN/m.

4.3.2 Sensing of BSA protein using SAM of MUA as the functional layer

Using the QCM, the change in values of mass per unit area due to the adsorption of analytes is estimated by measuring the change in resonance frequency of the quartz crystal resonator. The change in frequency ($\triangle$f) is directly proportional to the change in mass per unit area ($\triangle$m) [111] through the Sauerbrey relation, (Eq.1.4). The concentration of BSA in ion–free ultrapure water was varied from 0.075 nM to 142.11 nM and the change in piezoresponse with respect to the ultrapure ion–free water is measured. Fig.4.4 shows the variation of mass of BSA adsorbed per unit area on (i) piranha treated quartz wafer (filled squares) and (ii) the SAM of MUA (open squares) as a function of concentration of BSA in aqueous medium.

It can be noted (Fig.4.4) that the change in mass increases monotonically with the increase in concentration of BSA. The rate of change in mass with respect to concentration of BSA appears to be comparable at the lower concentrations of BSA in water (i.e. $<$ 40 nM) for both the cases of pure gold and carboxylated (MUA) treated gold surfaces. Above the concentration $\sim$40 nM, there is a dramatic increase in the rate of mass change on the carboxylated surface as compared to that of pure gold surface. At the lower concentration, few BSA molecules adsorbed to the surface, act as nucleation sites for the further adsorption of molecules with the increase in concentration of the BSA in the medium. The SAM of MUA offers carboxylated surface which can attract

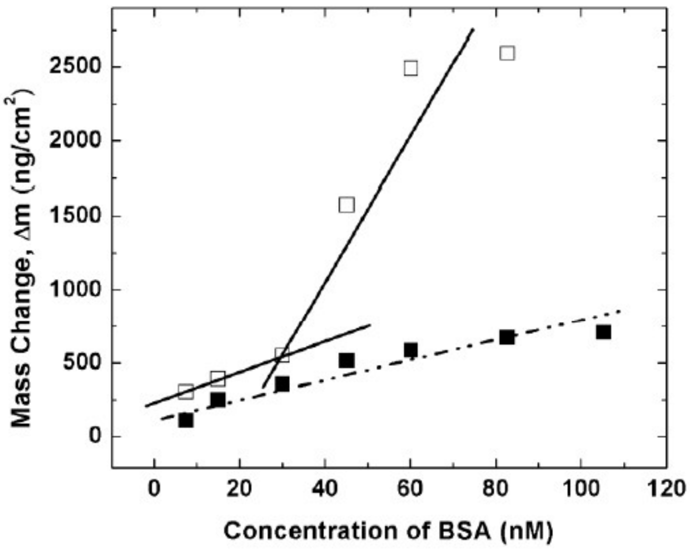

FIGURE 4.4: Variation of mass of BSA adsorbed per unit area on (i) piranha treated gold–coated quartz wafer (filled squares) and (ii) the SAM of MUA (open squares) as a function of concentration of BSA in aqueous medium.

the compatible (cationic) part of the protein to get adsorbed onto the surface to form the nucleation sites. Such nucleation sites on MUA can further attract other BSA molecules to get adsorbed onto the surface of SAM leading to the growth of the BSA domain.

In contrast, the gold surface offers only an area for normal physio–adsorption of the BSA molecule. Hence, the adsorption curve obtained for pure gold surface shows a constant slope indicating a constant rate of adsorption with increase in concentration of BSA protein in aqueous medium. The normal physical adsorption onto the gold surface is unstable due to weak BSA molecule–substrate interaction. It was also observed during the measurement that the adsorption of BSA over the SAM of MUA was rapid as compared to that onto the surface of pure gold.

The morphology of the functional layer (SAM of MUA) and adsorbed BSA on MUA functionalized surface is studied using the AFM. Fig.4.5 shows the morphology of SAM of MUA deposited on gold–coated quartz crystal and BSA adsorbed over the functionalized gold–coated quartz crystal. The morphology of SAM of MUA (Fig.4.5(a)) shows relatively smaller domain as compare to that of BSA adsorbed layer (Fig.4.5(b)). The calculated average roughness of the SAM of MUA and BSA over the SAM are 3.5 and 2.7 nm, respectively. Due to adsorption of BSA over the SAM of MUA, the uniformity

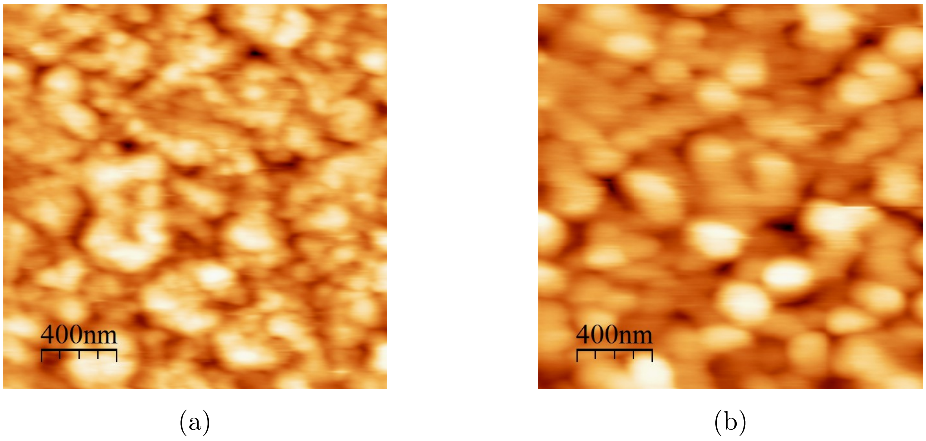

(a) (b)

Figure 4.5: AFM images of (a) SAM of MUA over gold coated crystal and (b) BSA adsorbed over SAM of MUA. The size of each image is 2x2 μm^2.

in the texture increases and the roughness of the film reduces to 2.7 nm . The image (Fig.4.5(b)) shows spherical domains which can represent the domains of globular BSA protein. The size of the spherical domains lies in range of 200 to 300 nm. Our studies indicate a strong signature of BSA protein adsorption by the functional layer of MUA. The sensing performance of BSA protein using a QCM can be enhanced with suitable functionalization of the gold deposited quartz crystals.

Based on our study, a schematic diagram for BSA adsorption over gold coated quartz crystal and SAM of MUA on the quartz crystal is shown in Fig.4.6.

4.3.3 Sensing of L–asp acid using LB and spin coated films of ODA– SWCNTs as the functional layer

ODA–SWCNTs can provide opportunity to create not only the mesopororous film but also cationic adsorption sites for the trapping of anionic analytes. Preserving the fundamental properties of CNTs, the functionalized CNTs can be aligned onto the active area of a device to yield its best performance. Here, we have studied the sensing of biologically relevant chemical analytes e.g. L–asp acid and BSA protein using the LB and spin coated films of ODA–SWCNTs. Sensing layer of ODA–SWCNTs is fabricated over the SAM of MUA deposited onto the quartz crystal wafers using LB technique and spin coating method. The LB technique provides highly organized layer of ODA–SWCNTs, however the spin coating technique provide random netwok of ODA–SWCNTs. The single layer of LB film of ODA–SWCNTs was deopisted on

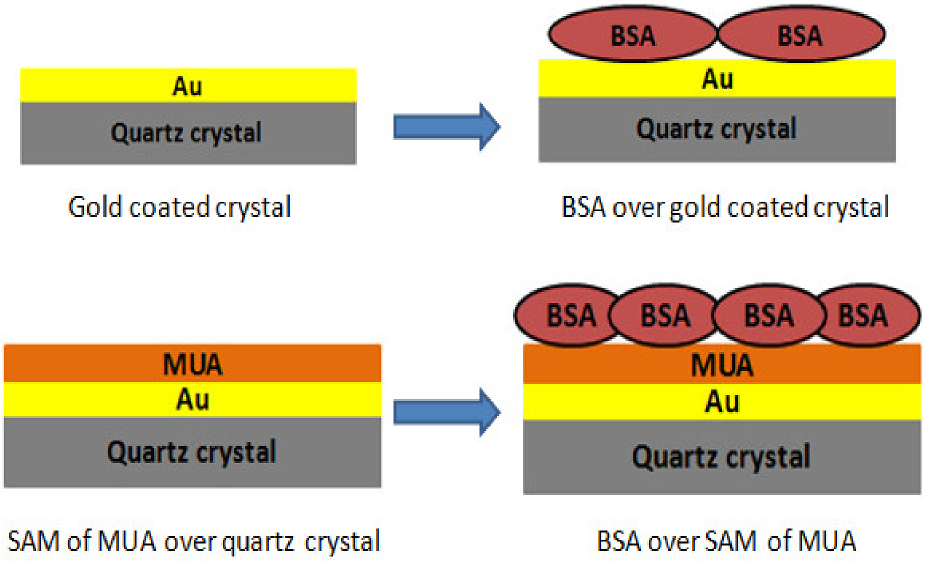

FIGURE 4.6: Schematic of adsorption of BSA over gold–coated quartz crystal and SAM of MUA.

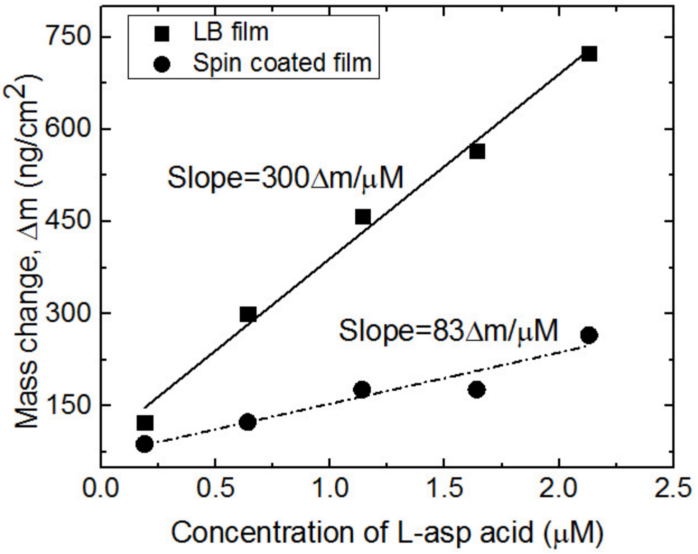

FIGURE 4.7: Variation of mass of L–asp acid adsorbed per unit area on (i) LB film of ODA–SWCNTs (filled squares) and (ii) the spin coated film of ODA–SWCNTs (filled circles) as a function of concentration of BSA in aqueous medium.

functionalized (SAM of MUA) quartz crystal and employed for the sensing of L–asp acid using QCM. The change in mass due to adsorption of L–asp acid onto the spin coated thin film of ODA–SWCNTs shows a linearly increasing trend with the increase in concentration of L–asp acid in the ultrapure ion–free water (Fig.4.7 (filled circles)).

The sensitivity of a sensor is proportional to slope of such curves [185]. The calculated slope value for mass adsorbed over spin coated film of ODA–SWCNTs is 83 ng/cm^2/μM. Mass of L–asp acid adsorbed over LB film of ODA–SWCNTs vs concentration of L–asp acid curve is shown in Fig.4.7 (filled squares). The change in mass increases rapidly and linearly with the increase in concentration of L–asp acid dissolved into the ultrapure ion–free water. The lowest detectable concentration of L–asp acid is found to be around 0.2 μM. The calculated slope value for mass adsorbed over LB film of ODA–SWCNTs is 300 ng/cm^2/μM which is much higher than that of spin coated film of ODA–SWCNTs. Thus, the sensitivity of the L–asp acid sensor fabricated using LB films is much higher than that of spin coated films of ODA–SWCNTs.

The L–asp acid sensing characteristics of LB film of ODA–SWCNTs is comparatively better than spin coated film. This may be due to the alignment in ODA–SWCNTs in ultrathin LB films. The morphology of the surface after the adsorption of L–asp acid adsorbed onto spin coated film and ultrathin LB film of ODA–SWCNTs is shown in Figs. 4.8(a) and (b), respectively. Image (a) shows few large domains of maximum thickness ∼7 nm whereas image (b) shows a large number of circular domains with maximum thickness ∼20 nm. This indicates that the LB films of ODA–SWCNTs

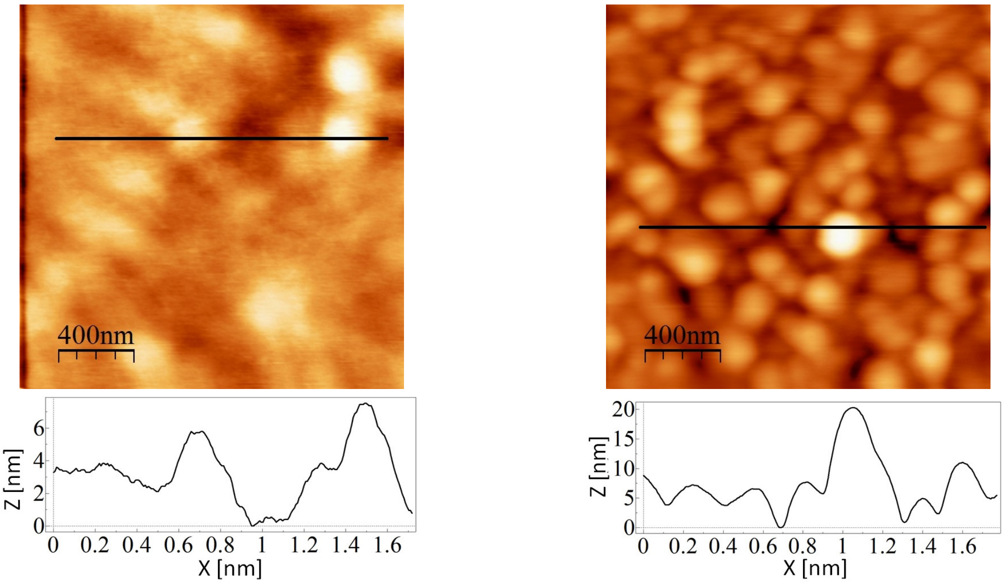

(a)

(b)

Figure 4.8: AFM images of L–asp acid adsorbed over (a) spin coated film of ODA–SWCNTs and (b) LB film of ODA–SWCNTs. The size of each image is 2x2 μm^2. The height profile along the black line is shown below the respective AFM image.

creates a large number of adsorption sites and faciliated the nucleation and growth of the circular domains of L–asp acid. The random network of the ODA–SWCNTs in the spin coated film may not facilitate the growth of nucleated sites into the larger domains and hence image (a) (Fig.4.8) appears smoother as compared to that of image (b) (Fig.4.8). The aligned bundles of ODA–SWCNTs in the LB films may support not only the creation of larger number of nucleation sites for L–asp acid adsorption but also further growth of the sites into larger domains. This result is in consistence with the results obtained from the QCM which indicates the sensitivity of LB film is much higher than that of the spin coated film of ODA–SWCNTs.

The schematic of adsorption of L–asp acid over ODA–SWCNTs is shown in Fig.4.9.

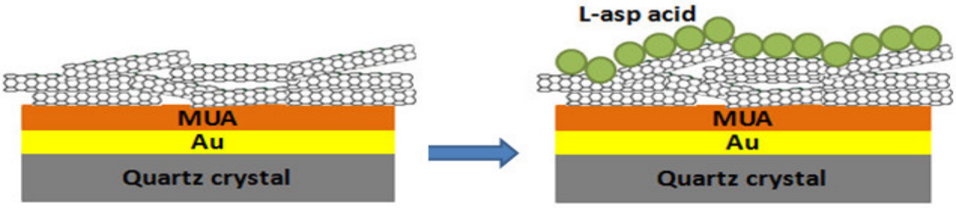

Figure 4.9: Schematic of adsorption of L–asp acid over ODA–SWCNTs.

4.3.4 Sensing of BSA protein using LB and spin coated films of ODA– SWCNTs as the functional layer

The LB film of ODA–SWCNTs is found to be a promising candidate as the functional layer for sensing the amino acid *i.e.* L–asp acid. We extended our investigation by studying the sensing performance of LB films as compared to that of spin coated films of ODA–SWCNTs towards BSA protein. Fig.4.10 shows the variation of change in mass due to adsorption of BSA per unit area on (i) LB film of ODA–SWCNTs (filled circle) and (ii) the spin coated film of ODA–SWCNTs (filled squares) as a function of concentration of BSA in aqueous medium. The ODA–SWCNTs films are fabricated onto the SAM of MUA over the quartz crystal wafers for QCM measurememts.

It can be noted that the piezoresponse on the adsorption of BSA over the spin coated film of ODA–SWCNTs is relatively very small. Assuming the linear trend in the variation of change in mass vs concentration of BSA in aqueous medium, the slope

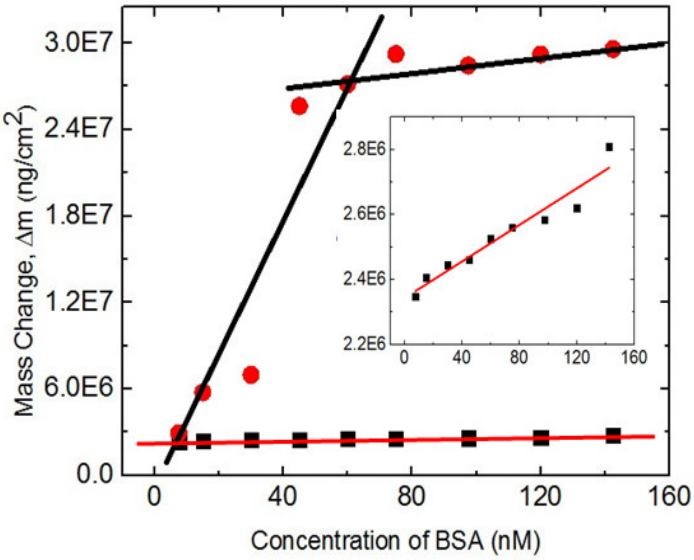

FIGURE 4.10: Variation of mass of BSA adsorbed per unit area over (i) LB film of ODA–SWCNTs (filled circles) and (ii) the spin coated film of ODA–SWCNTs (filled squares) as a function of concentration of BSA in aqueous medium.

is estimated to be $\sim 2.8\times10^3$ ng/cm^2/nM. Interestingly, the piezoresponse from the LB film of ODA–SWCNTs for the sensing of BSA protein is found to increase very rapidly for the lower concentration range ($<$ 60 nM) and then increase slowly for the concentration $>$ 60 nM of BSA in the aqueous medium. Similarly, assuming the linear trend for these two different concentration range, the slopes are estimated to be $\sim 5.1\times10^5$ ng/cm^2/nM for the concentration $<$ 60 nM and 2.2×10^4 ng/cm^2/nM. This indicates that the sensitivity of the LB film of ODA–SWCNTs increases by orders of magnitude as compared to that of spin coated film of ODA–SWCNTs. The enhanced sensitivity of the LB film of ODA–SWCNTs can be related to the creation of large number of adsorption sites for attracting BSA protein. The further adsorption of BSA on the nucleated sites is facilitated by the ordering of the ODA–SWCNTs in the LB film leading to the growth of BSA domains. The adsorption of BSA protein over sensing layers is studied by obtaining the morphologies of the films before and after BSA protein adsorption using AFM.

The surface morphology of thin film of ODA–SWCNTs deposited by spin coating method and adsorbed BSA protein over such film of ODA–SWCNTs is studied using AFM. Fig.4.11(a) and (b) show the morphology of spin coated ODA–SWCNTs deposited on SAM of MUA on the quartz crystal wafer and the adsorbed BSA over the such functionalized quartz crystal. The image (Fig.4.11(a)) reveals the random

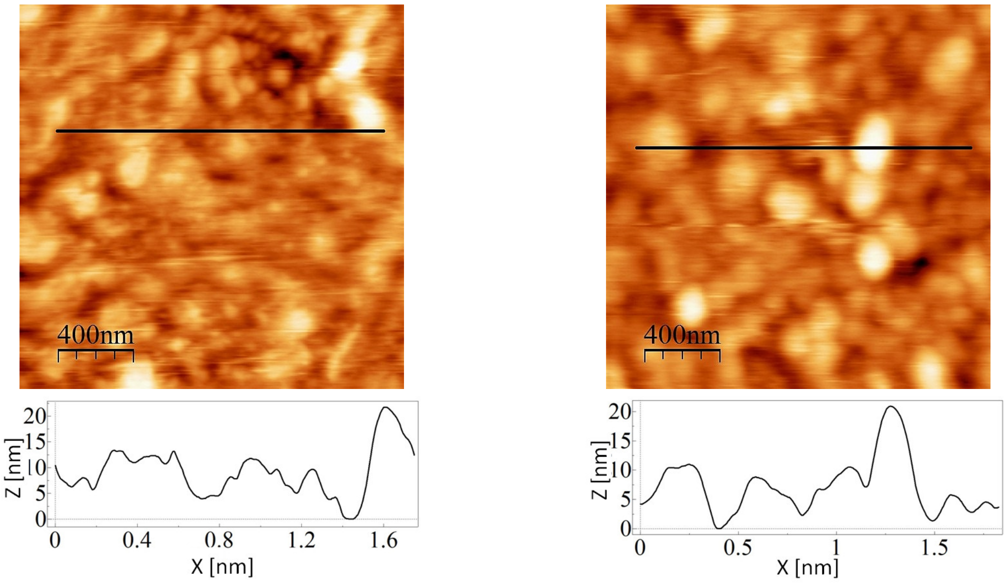

(a) (b)

Figure 4.11: AFM images of (a) spin coated film of ODA–SWCNTs over SAM of MUA and (b) BSA adsorbed over spin coated film of ODA–SWCNTs. The size of each image is 2x2 μm^2. The height profile along the black line is shown below the respective AFM image.

features which arises due to the random network of ODA–SWCNTs. After the QCM measurements on the same film, the features appears little smoother as compared to Fig.4.11(a). The random network of the ODA–SWCNTs in the spin coated film may not facilitate the growth of nucleated sites into the larger domains and therefore only a few globular domains can be seen from the image (Fig.4.11(b)). The height profiles shows that the average thickness of the film is not changed much after BSA adsorption experiment. The average height increases only by a few nanometers. Therefore, the adsorption of BSA protein is poor onto the spin coated film of ODA–SWCNTs.

The surface morphology of the LB film of ODA–SWCNTs on the SAM of MUA on the quartz crystal wafers and the adsorbed BSA over such functionalized surface is shown in Fig.4.12. Fig.4.12(a) reveals the organized elongated domains over the surface. This may be the bundles of ODA–SWCNTs over the SAM of MUA. The width of the elongated domains is around to be 50 – 60 nm which may correspond to the width of the bundles of SWCNTs. After the QCM measurements using such LB films, the AFM image (Fig.4.12(b)) shows large number of globular domains of size ranging between 100 – 250 nm. The height profiles below the respective images (Fig.4.12) show that the average thickness of the film is increased due to BSA adsorption. This clearly indicates

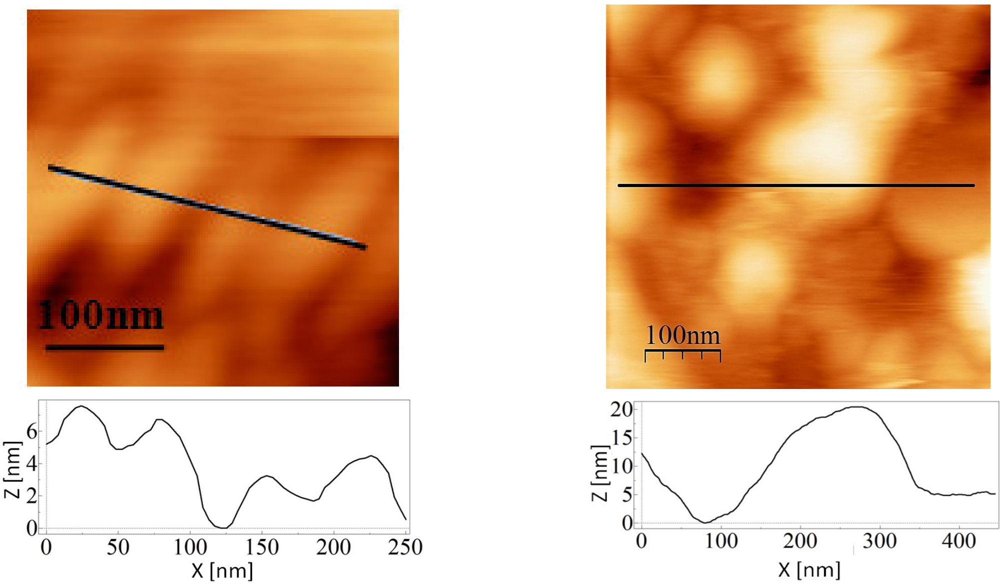

(a) (b)

Figure 4.12: AFM images of (a) LB film of ODA–SWCNTs over SAM of MUA. The size of image is 300x300 nm^2. (b) BSA adsorbed over LB film of ODA–SWCNTs. The size of image is 500x500 nm^2. The height profile along the black line is shown below the respective AFM image.

that the adsorption of BSA protein over the LB film is favored more as compared to that of spin coated film of ODA–SWCNTs.

The schematic of adsorption of BSA over ODA–SWCNTs is shown in Fig.4.13.

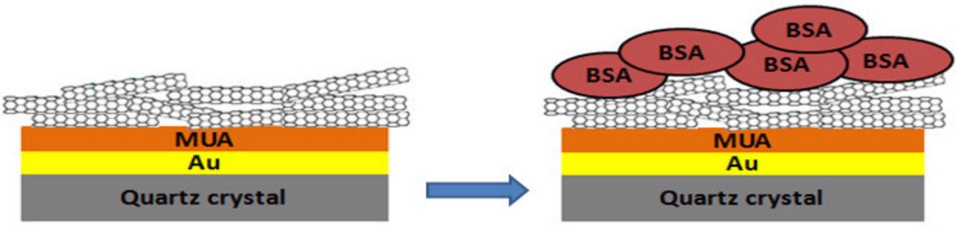

Figure 4.13: Schematic of adsorption of BSA over ODA–SWCNTs.

Estimation of slope values for change in mass per unit area of the different adsorbed layer is shown in Table. 4.1

Table 4.1: Summary of slope values for sensing L–asp acid and BSA using different sensing layer.

Sensing Layer	**Sensitivity for L–asp acid, ng/cm^2/μM**	**Sensitivity for BSA, ng/cm^2/nM**
Gold surface	–	6
SAM of MUA	–	64 for $\geq$40nM, 10 for $<$ 40nM
Spin coated film of ODA–SWCNTs	83	2.8×10^3
LB film of ODA–SWCNTs	300	2.2×10^4 for $>$ 60nM, 5.1×10^5 for $<$ 60nM

4.4 Conclusion

The functionalized SWCNTs offers not only the ease of device processability but also functional layer for attracting specific analytes in the sensing application. In this chapter, we report formation a stable LF of ODA–SWCNTs. The LB films of ODA–SWCNTs are fabricated onto the quartz crystal wafers of a QCM and are employed for sensing the biological analytes *viz.* L–asp acid and BSA protein. The sensing performance of the LB films of ODA–SWCNTs is compared with that of thin film of randomly oriented ODA–SWCNTs obtained through spin coating technique. The sensitivity towards the analytes using LB film is found to be far better than that of spin coated film of ODA–SWCNTs. The highly oriented ODA–SWCNTs in the LB films may create large surface density of adsorption sites which support the further growth of the nucleates sites into bigger domains. This in turn yield better performance and high sensitivity of the analytes by the LB films. The surface morphology study also reveals large number of adsorbed domains of L–asp acid and BSA protein by the LB film than that of spin coated film of ODA–SWCNTs.

It will be interesting to study the surface properties of more biologically compatible CNTs *viz.* poly ethylene glycol functionalized SWCNTs (PEG–SWCNTs). In the next chapter, we discuss the ultrathin film fabrication involving PEG–SWCNTs and their sensing application.

Chapter 5

Effect of PEG–SWCNTs in Subphase on Langmuir Monolayer and Langmuir–Blodgett Films of Cationic Surfactants

5.1 Introduction

In the previous chapter, we have demonstrated that the octadecylamine functionalized single–walled carbon nanotubes (ODA–SWCNTs) based quartz crystal microbalance (QCM) sensors are very sensitive to bovine serum albumin (BSA) protein at room temperature. The sensing capability of Langmuir–Blodgett (LB) films of ODA–SWCNTs is more enhanced as compared to spin coated film due to the nucleation and growth of domains of analytes on the aligned nanotubes in the ultrathin LB film.

It will be interesting to study the role of functionalized SWCNTs onto sensing of biologically relevant analytes. In this chapter, we present our studies on the interaction of cationic surfactant with deoxyribonucleic acid (DNA) using QCM. The interaction of polyethylene glycol functionalized SWCNTs (PEG–SWCNTs) with a cationic surfactant e.g. dioctadecylamine (DODA) at air – water (A/W) and air – solid (A/S) interfaces are investigated. We have employed the LB films of DODA/PEG–SWCNTs for DNA sensing and observed that DNA adsorption over LB film of DODA/PEG–SWCNTs is more enhanced as compared to dioctadecyl ammonium bromide (DOAB).

For many industrial applications, a uniform and stable dispersion of SWCNTs plays an important role. However, SWCNTs are highly hydrophobic and thus aggregate in aqueous environment under physiological condition, a fact which limits their use in biomedical applications. The dispersion of SWCNTs in water without its chemical modification is difficult. To maximize their versatility, the poor dispersibility of SWCNTs in aqueous medium needs to be addressed [186, 187]. The dispersibility of SWCNTs was significantly enhanced after their surface modification. SWCNTs have been often modified with amphiphiles such as lipids, surfactants, proteins, and hydrophilic polymers [188–191]. Functionalization of SWCNTs with polymer molecules, done either by noncovalent or covalent bonding, is one of the most common methods for enhancing nanotube dispersibility [89, 192, 193]. In one of such simple method, non–covalent SWCNTs functionalization uses single stranded DNA (ssDNA) to improve its aqueous dispersion. Zheng *et al.* [194] have reported that through π–π interactions, the DNA molecule was helically wrapped around the SWCNT surface. Fernando *et al.* [195] have used poly (propionylethylenimin–co–ethylenimine) and poly (vinyl alcohol), to increase SWCNTs dispersibility. The addition of polymer chains to the surface of SWCNTs is very useful as these macromolecules not only help to disperse the SWCNTs in solvent, but also provide functional groups for investigating molecular specific interactions [196–199].

Among the water–soluble polymers used for chemical modification of SWCNTs, polyethylene glycol (PEG) has received significant attention. PEG is a water–soluble, nontoxic, and biocompatible polymer. Fuctionalization of SWCNTs with PEG has been shown to render them soluble in physiological buffers, [200] and these systems have been studied as molecular transporters inside mammalian cells [191], as agents for selective probing and imaging of cells with fluorescence spectroscopy [201], and tumor targeting agents [202]. In particular, PEG has been often attached to the SWCNTs by a process called PEGylation [203, 204]. Such modification of SWCNTs increased solubility significantly and reduced cytotoxicity [205–210]. The functionalization of SWCNTs with PEG have resulted in SWCNTs graft copolymers with high dispersibility in water [89, 211]. The covalent approach to the preparation of water soluble SWCNTs provides materials with controlled composition and reproducible properties, which is of significant importance for biomedical studies. [212–217].

Understanding the molecular interactions of the biologically relevant molecules are essential not only for the design of novel drugs, but also for devices probing the systems rapidly and accurately. There are molecular specific interactions like antibody–antigen which work on the principle of lock–key mechanism. Such molecular specific interactions are potentially employed for the development of sensors [218, 219]. There are numerous studies on the interaction of DNA with proteins, lipid membranes and cationic surfactants [220–223].

In this chapter, we report our study on the interaction of DNA with the ultrathin film of a cationic surfactant DOAB. The ultrathin film of DOAB is fabricated by LB technique onto the hydrophobically treated quartz crystal wafers. The solution of DNA in phosphate buffer saline (PBS) is injected through a flow cell in a QCM loaded with the functional ultrathin film. The kinetic data indicates that the time constant (τ) of the adsorption of DNA on DOAB layer is ~162 seconds. The surface morphology of the aggregation of DNA over the DOAB layer is investigated using atomic force microscope (AFM). The AFM image indicates the trapping of DNA over the DOAB layer. Such trapping of DNA can be potentially employed in the field of genomics.

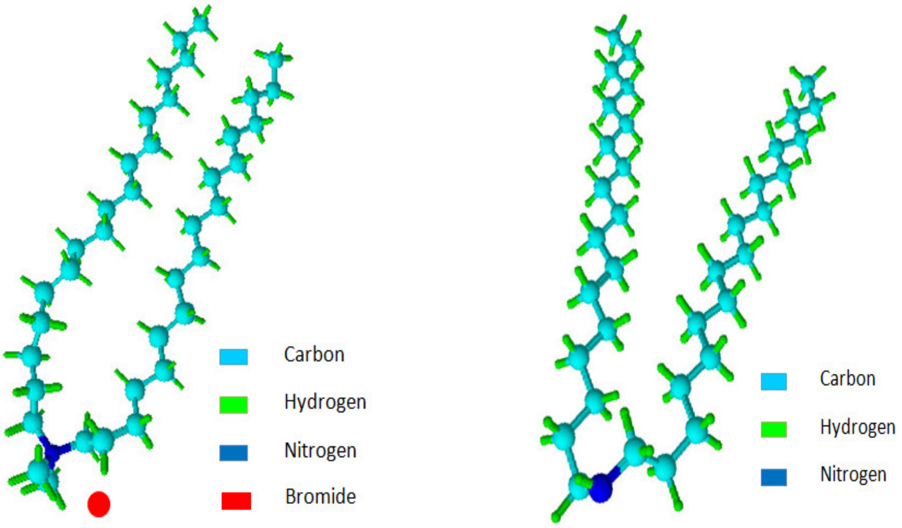

(a) (b)

FIGURE 5.1: Molecular structure of (a) Dioctadecylammonium bromide (DOAB) and (b) Dioctadecylamine (DODA).

The combination of DNA and SWCNTs has been intensively investigated by many research groups. DNA–SWCNTs conjugates have been used as biosensors for the detection of diverse species, including glucose [224, 225], proteins [226], pesticides [227], peroxide [228] among others. Hu et al. [229] reported the application of DNA–wrapped SWCNTs for biosensing. DNA–wrapped CNTs deposited over glass substrates were used as an electrochemical biosensor for the detection of dopamine. Their results showed that the prepared dopamine biosensor possesses excellent selectivity and sensitivity, even in the presence of interferences due to ascorbic acid.

The interaction of a cationic surfactant with PEG–SWCNTs has been studied. PEG–SWCNTs is immobilized with the monolayer of cationic dioctadecylamine (DODA) by electrostatic interaction at A/W interface. The molecular structure of DOAB and DODA are shown in Fig.5.1. The surface behavior of DODA and DODA/PEG–SWCNTs mixed Langmuir films (LF) has been characterized by surface pressure – area ($\pi - A$) isotherms. The LB film of DODA/PEG–SWCNTs is deposited onto quartz wafers of QCM and employed for sensing DNA. The lowest detectable concentration of DNA is found to be 3 fM. The morphological study on the film before and after adsorption of DNA also indicates the adsorption of DNA.

5.2 Experimental methods

5.2.1 Lanmuir and Langmuir–Blodgett Films

Dioctadecyl ammonium bromide (DOAB), dioctadecylamine (DODA) and octadecanethiol (ODT) were purchased from Sigma Aldrich and used without any further purification. PEG–SWCNTs was purchased from Carbon Solutions Inc, USA.

The DOAB and DODA solutions, each of concentration 1 mg/ml were prepared in high performance liquid chromatography (HPLC) grade chloroform. A solution of concentration 12 μg/ml of PEG–SWCNTs was prepared in absolute alcohol. 1ml solution of PEG–SWCNTs was added to the ultrapure ion free water (Millipore; 18 MΩ–cm) subphase maintained at a definite pH. The pH of the subphase is controlled by the addition of H_2SO_4 (Merck) or NH_4OH (Merck). The average pH value of pure water is 5.7. The pH value of water subphase was maintained at 3 and 10 in this study. The pH value reported is the average value recorded during the experiment. The LF of DODA was formed by spreading 100 μl solution drop by drop onto the water subphase using a Hamilton microsyringe. About 1 hour is allowed for the solvent to evaporate from the surface of the water and for the interaction of amine group of

DODA with PEG–SWCNTs dissolved into water. The $\pi - A$ isotherms are recorded by compressing the monolayer symmetrically using the two barriers of a LB trough. The compression rate of the barriers is maintained at 10.47 ($\AA^2$/molecule)/sec. DODA and DODA/PEG–SWCNTs layers are transferred onto hydrophobically treated quartz crystal wafers and Si/SiO_2 substrates by the vertical dipping mechanism of LB technique.

5.2.2 QCM Measurememts

The 5 MHz AT–cut quartz crystal wafers (SRS, USA) are used for DNA sensing application using QCM. The piranha treated gold–coated quartz wafer is made hydrophobic by depositing self assembled monolayer (SAM) of ODT. The wafers were dipped into 1 mM solution of ODT in absolute alcohol for about 24 hours. The treated wafers were rinsed thoroughly by the absolute ethanol and stored in water for LB film deposition. A single layer of LB films of the cationic surfactants were deposited onto the SAM–deposited quartz wafers. The single LB film of DOAB was deposited at 20 mN/m such that the functional group, amine is exposed to the air. Such arrangement of film is essential for establishing the cationic surfactant – DNA interaction. The functionalized quartz wafer is mounted in the QCM and the change in frequency ($\triangle$f) due to deposition of DNA are recorded as a function of time. A flow cell and a peristaltic pump for injecting fluids in a highly controlled manner are used in conjunction with the QCM (QCM200, SRS, USA). The escherichia coli (E. coli) bacterial DNA is dispersed in PBS solution with a concentration of 0.032 pM. The DNA solution was injected in the QCM at a rate of 75 μl/min. The lowest detectable concentration of DNA in PBS using the LB film of DOAB was found to be 0.020 pM. Therefore, for studying the kinetics of adsorption of DNA over LB film of DOAB, 0.032 pM solution of DNA in PBS was used.

The single LB film of DODA/PEG–SWCNTs deopisted on functionalized quartz wafer is mounted in the QCM holder. The holder was vertically dipped into the beaker filled with 80 ml of PBS solution. A stock solution of E. coli DNA was prepared in PBS with a concentration of 2.58 pM. The 100μl DNA solution from stock solution was injected into the beaker through a micropipette and the change in frequency ($\triangle$f) for different concentration of DNA solution was recorded.

5.2.3 Atomic Force Microscopy

The surface topography of the films are studied using an AFM in contact mode. The images were obtained by scanning the films using silicon tips having the spring constants ∼1 N/m. The images were analyzed using the proprietary software of NTMDT.

5.2.4 Field Emission Scanning Electron Microscopy

The surface morphology of the LB film was obtained using a field emission scanning electron microscope (FESEM). The extra high tension (EHT) voltage was maintained at 1–2 kV.

5.2.5 Raman Spectroscopy

The spin coated film of PEG–SWCNTs deposited onto Si/SiO$_2$ substrate was scanned using a Raman spectrometer equipped with 20 mW Ar$^+$ laser as the excitation source.

Raman spectrum of spin coated film of PEG–SWCNTs is shown in Fig.5.2. It indicates the presence of two strong peaks at about 1352 cm^{-1} and 1580 cm^{-1}, commonly known as the first–order D and G bands of SWCNTs. The peak at about 1580 cm^{-1} corresponds to G–band of SWCNTs, which is due to the sp2–bonded carbon atoms in SWCNTs. The D band at about 1352 cm^{-1} is associated with the presence of defects in structure of SWCNTs [230, 231].

Furthermore, the two–order D peak (G'–band) at about 2690 cm^{-1} is also observed. The ratio of the intensity of the D and G bands is known to be correlated to the quality of SWCNTs, which is used to estimate the degree of disorder in structure of carbon nanotubes [230]. By calculation, the I$_D$/I$_G$ ratio of sample is found to be 0.15. However, the low D–to–G peak intensity ratio indicates the overall high structural quality of the spin coated PEG–SWCNTs. The Raman spectrum of PEG–SWCNTs shows the radial breathing mode (RBM) of SWCNTs at 164 cm^{-1}. Tube diameters can be easily estimated from RBM frequencies of Raman spectra and can be calculated from [232]:

$$d = \frac{234}{\omega_r} \tag{5.1}$$

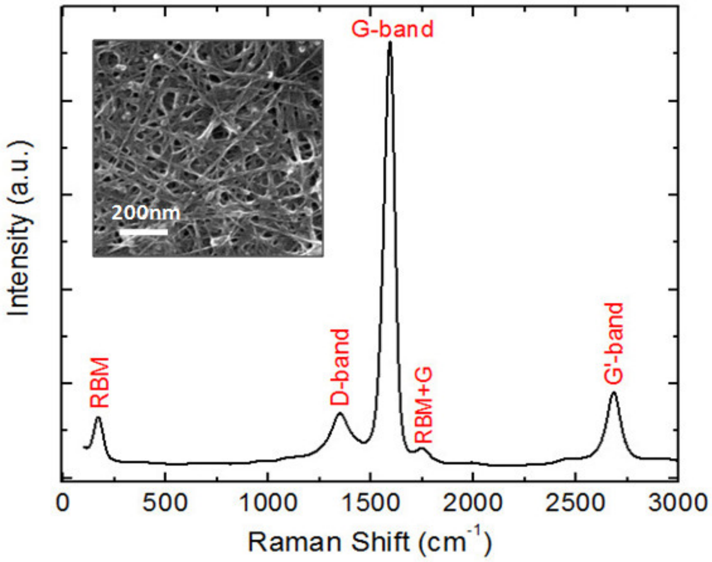

Figure 5.2: Raman spectrum of spin coated film of PEG–SWCNTs. The FESEM image of the film is shown in the inset.

where d is the tube diameter in nm and ω_r is the RBM frequency in cm^{-1}. Figure shows a clear RBM centered at 164 cm^{-1} and can be attributed to the strong presence of SWCNTs having a mean diameter of 1.4 nm. The Raman spectrum contains the prominent peaks at 1750 cm^{-1} corresponding to the well documented RBM+G band [233]. The FESEM image of the spin coated film of PEG–SWCNTs deposited onto Si/SiO$_2$ substrates is shown as inset of Fig.5.2. The FESEM image in the inset shows the random network of the bundles of PEG–SWCNTs.

5.3 Results and discussion

5.3.1 Surface Manometry of LM of DOAB

The surface pressure (π) – area (A_m) isotherm of the Langmuir monolayer (LM) of DOAB at A/W interface is shown in Fig.5.3(a). The isotherm shows zero value of π at a very large A_m. This is the gas phase of the monolayer. On compression, the isotherm starts showing non–zero value of π at A_m = 0.65 nm^2 (a). This is the onset of a liquid–expanded (LE) phase. The value of π rises slowly till a kink is ovserved at π = 15mN/m (b). The π increases rapidly and monotonically thereafter on reducing A_m till the monolayer collapses at around 54 mN/m. The region of the isotherm from a to b corresponds to LE phase. The phase corresponding to the steep rise in π (b to c) may corresponds to a liquid–condensed (LC) phase. The orientational state (tilt or untilt) of the molecules in a phase can be estimated qualitatively by comparing the extrapolated area per molecule with that of molecular cross–sectional area in the bulk single crystal [143]. Theoretically, the cross–sectional area of the vertically aligned DOAB molecule was calculated using chemsketch software and it is found to be $\sim$0.5 nm^2. The estimated A_0 value from the isotherm is found to be $\sim$0.53 nm^2. Therefore, the DOAB molecules are expected to be aligned vertically in the LC phase. The in–plane isothermal elastic modulus (E) as a function of A_m is evaluated from a given isotherm using the Eq.2.1. The E – A_m for the LF of DOAB is shown in Fig.5.3(b). The maximum value of E corresponding to LE and LC phases is found to be $\sim$70 and $\sim$185 mN/m, respectively. LC phase is more elastic and may possess high ordering as compared to LE phase. Since the molecules are in more ordered state in the LC phase, we have chosen the LB film deposition of DOAB on the quartz wafer of QCM in this phase.

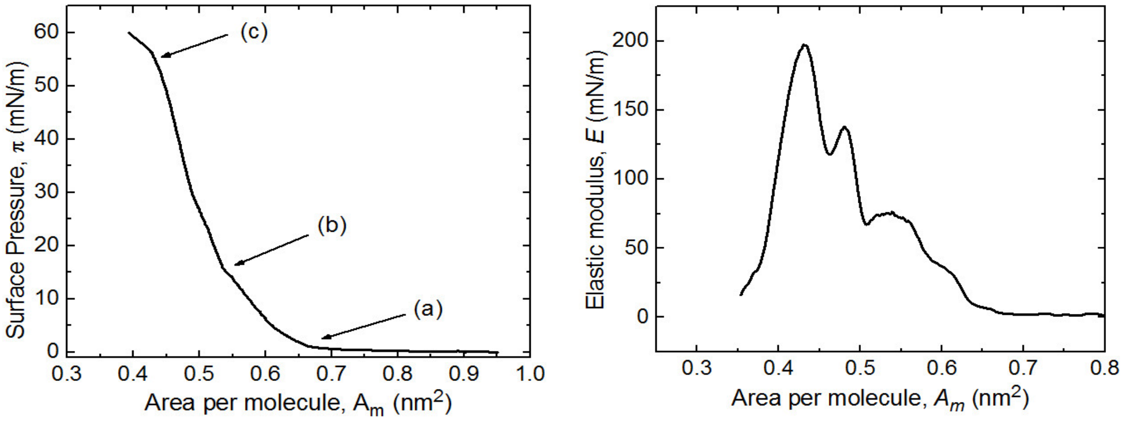

(a)

(b)

FIGURE 5.3: (a) Surface pressure (π) – area (A_m) isotherm of Langmuir film of DOAB and (b) the in–plane elastic modulus of Langmuir film of DOAB, as a function of A_m.

5.3.2 Sensing of DNA using LB film of DOAB

The LB film of DOAB is deposited onto the quartz crystal wafers and employed for sensing DNA in the aqueous medium using the QCM. In order to enhance the adsorption of anionic DNA, the functional layer with cationic adsorption sites are created by depositing a single layer of LB film of DOAB such that cationic ammonium bromide part is exposed to air and available for attracting DNA. This is achieved by the following procedure. A SAM of ODT is deposited onto the gold film of quartz wafers. This yields hydrophobic surface. Such hydrophobic quartz wafer is used for depositing one layer of LB film of DOAB. The LM is held at the target surface pressure and the dipper holding the hydrophobic quartz wafer is dipped down from air to the water subphase with the monolayer at the A/W interface. Due to such downstroke of the dipper, one layer of cationic surfactant is deposited onto the quartz wafer. The monolayer at the A/W interface is removed and the quartz wafer deposited with such single layer of LB film is taken out. Such functionalized quartz wafer is employed for sensing DNA using the QCM. The modified quartz crystal is mounted on the QCM and the change in mass is recorded at every step. This is shown in Fig. 5.4. The curve

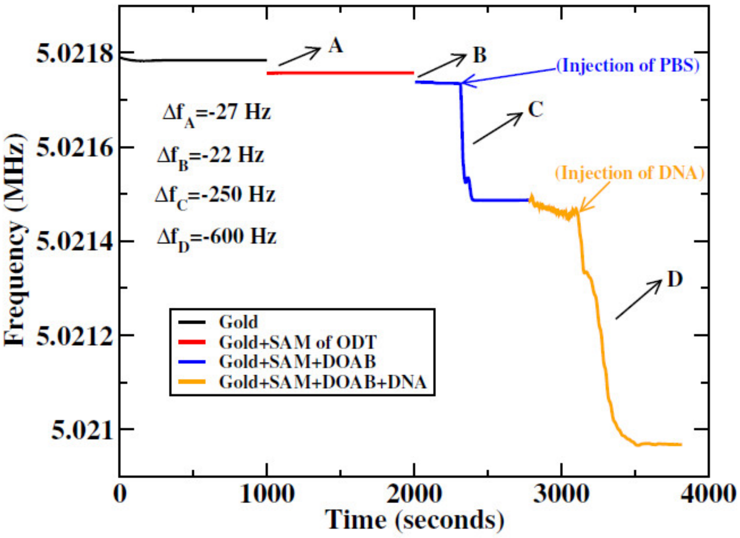

FIGURE 5.4: Quartz crystal microbalance measurements. The labels indicate change in response due to: A→SAM of ODT, B→LB film of DOAB on SAM of ODT, C→injection of PBS, D→injection of DNA in PBS.

showing change in mass due to adsorption of SAM (A), and LB film of DOAB (B) remain constant with time as there is no change in mass with time. The pure PBS solution is injected into the flow cell of QCM and a drastic drop in response is recorded (C). The curve remains almost flat till a solution of DNA having a concentration of 32 fM in PBS is injected in the flowcell (D). The response drops and becomes saturated after sometime. The drop in the response due to the injection of pure PBS (C) is due to change in medium from air to PBS whereas the drop in response due to injection of

PBS solution of DNA is due to interaction and adsorption of DNA over the cationic layer of DOAB. The time constant (τ) for such adsorption is calculated by fitting the experimental curve using an exponential curve: $f(t) = A_1\ Exp(-t/\tau)$, where A_1 and τ are the fitting parameters. The time constant (τ) is found to be ~162 seconds (Fig. 5.5).

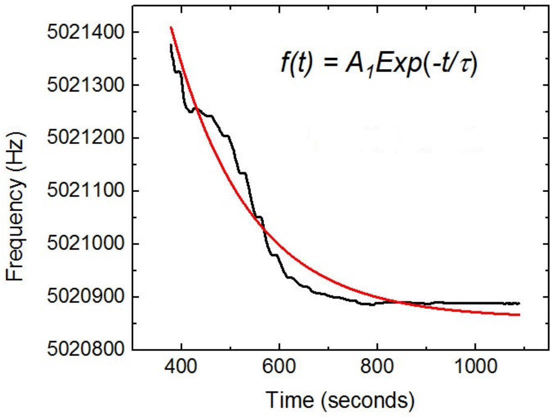

FIGURE 5.5: Kinetic curve showing the variation of frequency of the QCM with time due to the adsorption of DNA in PBS solvent.

The change in mass per unit area of the adsorbed layer is tabulated in Table 5.1.

TABLE 5.1: Estimation of mass per unit area of the adsorbed layer at the different levels of the QCM measurement. The change in frequency is measured with respect to the frequency corresponding to the previous adsorbed layer.

Adsorbed Layer	**△f, Hz**	**△m, ng/cm^2**
SAM of ODT	27	477
DOAB	22	389
PBS	250	4417
DNA	600	10601

The surface morphology of the functional layers and the adsorbed DNA layer is studied using the AFM. The images are shown in Fig.5.6. The AFM image of the SAM of ODT reveal layer with few defects (image A and B of Fig.5.6). The presence of defects in the height image is consistent with the phase imaging. The defects appear very small and distributed uniformly over the entire scan range of 10×10 μm^2. Due the deposition of one layer of LB film of DOAB over the SAM of ODT, the uniformity in the texture is increased. The AFM image of the DOAB reveals a uniform and homogeneous LB film

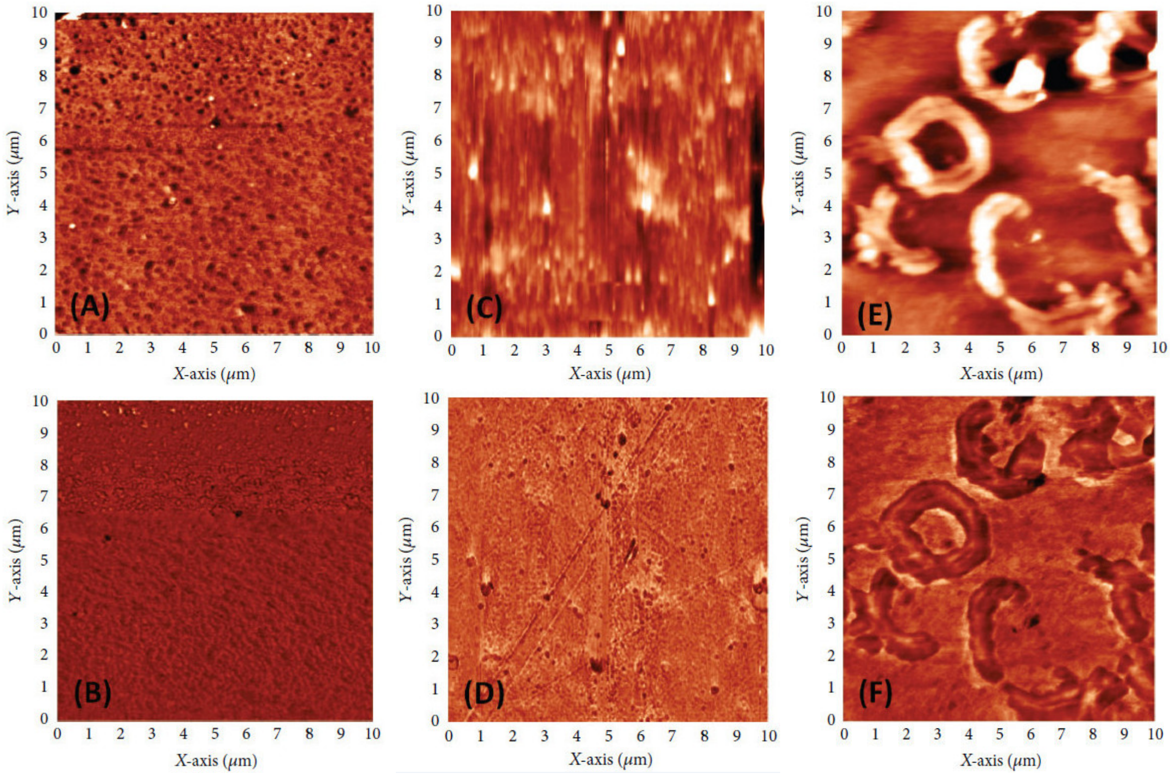

Figure 5.6: AFM image of (A and B) SAM of ODT on gold deposited quartz crystal, (C and D) one layer of LB film of DOAB deposited over the SAM of ODT and (E and F) DNA adsorbed over DOAB after the QCM measurement. The images were scanned in semicontact mode of the AFM. The upper row represents the height images and bottom one is corresponding to phase image.

(image C and D of Fig.5.6). On injection of DNA solution over the DOAB layer, due to the electrostatic charge–charge interaction of DNA and DOAB, the DNA strands physio–adsorbed onto the surface of LB film of DOAB. Image E and F of Fig.5.6 clearly shows the adsorbed DNA over the DOAB layer. The strands of DNA are clearly visible in both the height and phase images. Our study indicates the trapping of DNA over the highly ordered functional ultrathin layer of DOAB. Such trapped DNA may serve as an useful tool in genomics.

The pH value of ultrapure water is found to be 5.7. This is due to the absorption of atmospheric CO_2 and the formation of weak carbonic acid in water. The isoelectric point (IP) of DOAB is 5.5 which is similar to the pH value of ultrapure water subphase. Therefore, DOAB can easily get dissociated in ultrapure water, becomes cationic and hence the LM of DOAB becomes little less stable. The IP of DODA is 4.5 and it become positively charged only at lower pH (below 4.5). Therefore, LM of DODA can form a more stable monolayer on the ultrapure ion–free water. Furthermore, we have investigated surface manometry of LM of DODA at different pH values of water subphase and studied the phase behavior of DODA and DODA/PEG–SWCNTs. We have also investigated the interaction of DNA with LB film of DODA/PEG–SWCNTs using QCM.

5.3.3 Surface Manometry of LM of DODA and DODA/PEG–SWCNTs

The $\pi - A$ isotherms of DODA monolayer at the A/W interface recorded on the surface of ultrapure water and PEG–SWCNTs solution at various values of pH are shown in Fig.5.7. The monolayer of DODA on the ultrapure water subphase (Fig.5.7(b)) shows zero surface pressure at large A$_m$. This is gas phase of the monolayer. On compression, the surface pressure rises sharply. This may be LC phase of DODA at the A/W interface. The extrapolated A$_m$ to the zero surface pressure of this phase

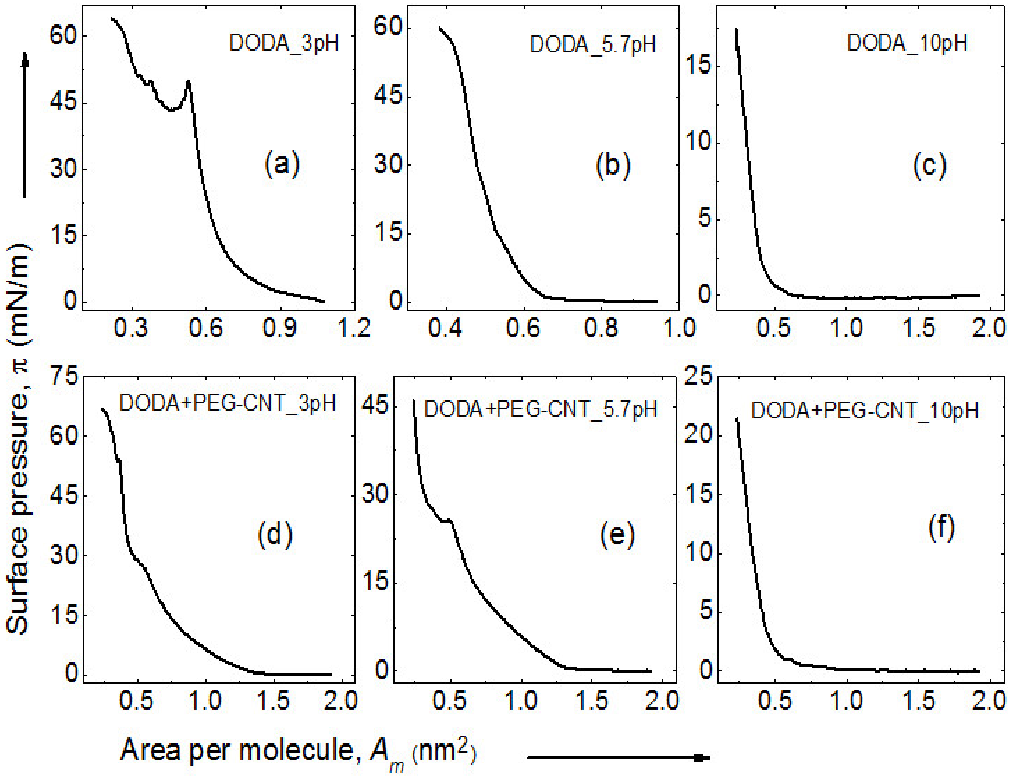

FIGURE 5.7: Surface pressure (π) – area (A) isotherms of LF of DODA (curve a, b and c) and DODA/PEG–SWCNTs (curve d, e and f) at different pH value of water subphase. Here the PEG–SWCNTs are dispersed in the aqueous subphase having a concentration of 12 μg/ml.

is found to be ∼0.6 nm^2. The collapse of the monolayer is observed as the change in slope at ∼57 mN/m. On reducing the pH of the subphase (acidic medium), the LM of DODA becomes unstable. The sharp kink at the startup surface pressure vanishes and the surface pressure rises gradually on compression of the monolayer. The collapse surface pressure appears at lower values i.e. 48 mN/m (Fig.5.7(b)). The isotherm recoded on the basic medium (Fig.5.7(c)) shows very steep rise in surface pressure. The collapse of the monolayer is not observed in this case. The presence of PEG–SWCNTs in the aqueous subphase has its effect on the isotherms only for ultrapure and acidic water subphase. This clearly indicates that PEG–SWCNTs do not interact with the DODA in the basic medium (Fig.5.7(c) & (f)). The startup surface pressure of the LM of DODA on ultrapure water with PEG–SWCNTs in subphase is found to increased to 1.3 nm^2 (Fig.5.7(e)) from 0.65 nm^2 as compared to that of LM on ultrapure water subphase (Fig.5.7(b)). It can also be noted that due to interaction of PEG–SWCNTs in the subphase in ultrapure water (Fig.5.7(e)), the isotherm shows an additional kink at ∼24 mN/m. This can be the collapse of LM of DODA/PEG–SWCNTs. Since LM of DODA is little unstable on acidic subphase, and its interaction with PEG–SWCNTs is almost negligible on the basic subphase, we have formed the LB film of DODA/PEG–SWCNTs from ultrapure ion–free water subphase at a target surface pressure of 10 mN/m and characterized them using FESEM.

5.3.3.1 FESEM Characterization

Different growth patterns such as dendritic domains [234], fractal–like domains [235] and dense–branched domains [236] have been observed when LM undergoes a first–order phase transition from LE to LC phase. The FESEM images of single layer of LB film of DODA deposited on Si/SiO$_2$ substrate at π_t =10 mN/m from the ultrapure water subphase is shown in Fig.5.8. The image shows small round bright domains along with large bright domains with dendritic pattern. The small domains seems to be nucleation sites. The further growth of the nucleation sites destabilizes yielding the dendritic domains.

FESEM images of the LB film of DODA/PEG–SWCNTs deposited at $\pi_t = 10mN/m$ from the ultrapure water subphase containing 12 μM PEG–SWCNTs is shown in Fig.5.9. The characteristic morphological features of the LB film of DODA e.g. small bright domains and big dendritic domains can be clearly seen from the image (Fig.5.9(a)). In addition to these features, the zoomed image (Fig.5.9(b)) reveals long and thin

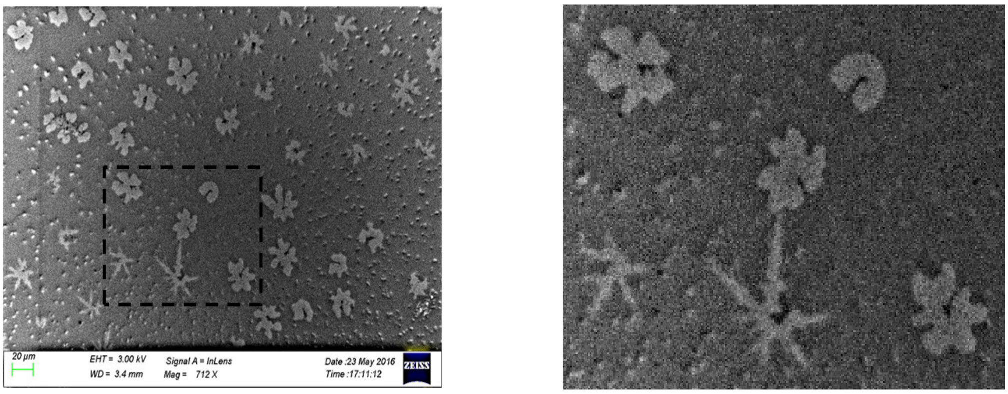

(a) (b)

Figure 5.8: FESEM image of LB film of DODA deposited at π_t = 10mN/m. The size of the image is: (a) 425x425μm^2 and (b) 150x150μm^2.

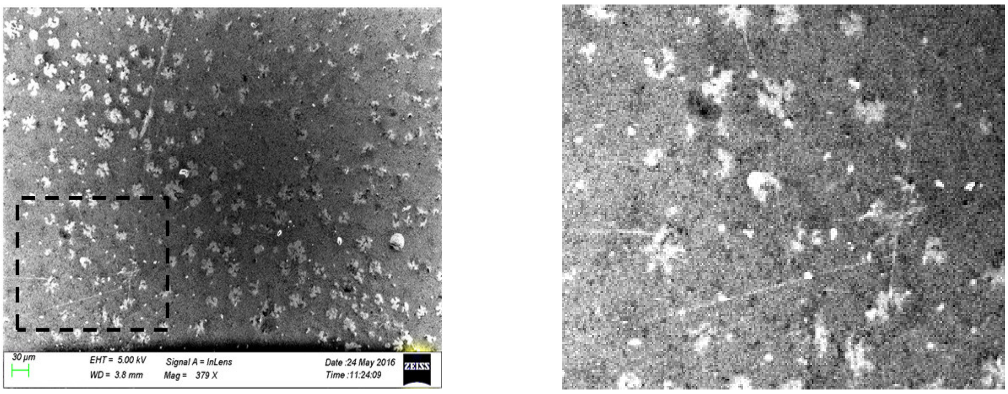

(a) (b)

Figure 5.9: FESEM image of LB film of DODA/PEG–SWCNTs deposited at π_t = 10 mN/m. The size of the image is: (a) 780×780 μm^2 and (b) 260×260 μm^2.

wire–like strands. Such strands are due to the adsorption of PEG–SWCNTs on the LB film of DODA from the liquid phase.

5.3.4 Sensing of DNA using LB films of DODA/PEG–SWCNTs

A single layer of LB film of DODA/PEG–SWCNTs was deopisted on the SAM of ODT over quartz crystal and employed for DNA sensing using QCM. The value of change in mass due to DNA adsorption per unit area is estimated by measuring the change in resonance frequency of the quartz crystal resonator. The mass change vs concentration of DNA in PBS solvent is shown in Fig.5.10.

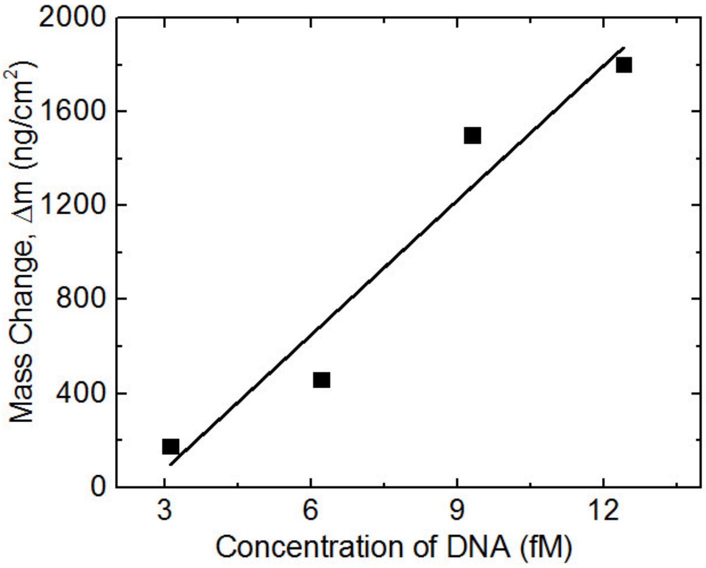

Figure 5.10: Mass change vs DNA concentration curve for LB film of DODA/PEG–SWCNTs over gold–coated quartz crystal.

It can be noted that the change in mass increases monotonically with the increase in concentration of DNA. The lowest detectable concentration of DNA is found to be ∼3 fM which is very low as compared to that of sensing using LB film of DOAB. Assuming a linear trend, the slope of the curve is found to be 190 ng/cm^2/fM. DNA can easily bind to CNTs by non–covalent attachment [237]. The DNA strands spontaneously wrap around the CNTs [238, 239]. This occurs via π–stacking between the aromatic rings of the DNA bases and the sidewall of CNTs [240]. Also, the presence of PEG–SWCNTs over the LB film of DODA can create a semi–mesoporous structure (as seen in the FESEM images) which can enhance the trapping of analytes when LB film architecture of DODA/PEG–SWCNTs is employed for sensing application. It is therefore, expected that the LB film of cationic surfactant, DODA can interact with anionic analytes and the PEG–SWCNTs can enhance the further adsorption of the analytes by trapping them in their semi– mesoporous structure. The PEG–functionalization of the SWCNTs can also facilitate the hydrogen bonding with the analytes.

The surface topography of the LB films of DODA/PEG–SWCNTs before and after the adsorption of DNA from the liquid phase is obtained by scanning the films using AFM in contact mode. The LB films of DODA/PEG–SWCNTs was transferred on pre–treated (SAM of ODT) quartz crystal. LB Film of DODA/PEG–SWCNTs is deposited in the liquid condensed phase of the LF from the ultrapure ion–free water subphase. The AFM images depicting the surface topography of LB film of DODA/PEG–SWCNTs and DNA adsorption onto the LB film of DODA/PEG–SWCNTs are shown in Fig.5.11.

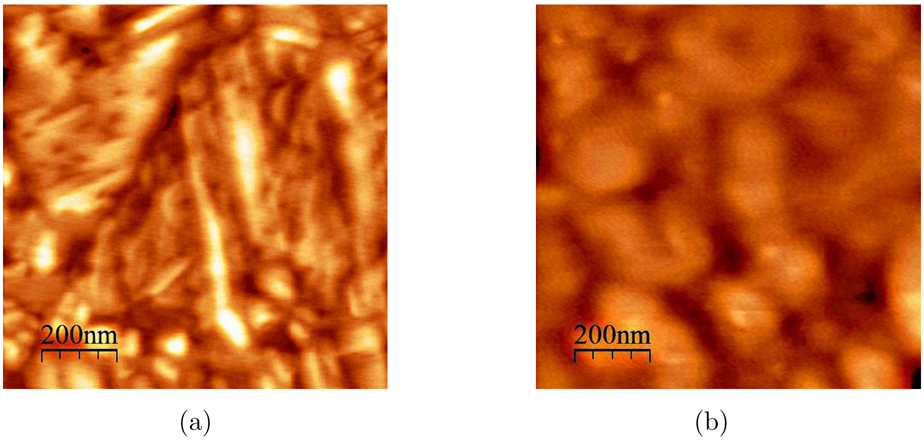

(a) (b)

FIGURE 5.11: AFM image of LB film of (a) DODA/PEG–SWCNTs and (b) DNA adsorbed over LB film of DODA/PEG–SWCNTs. The size of the image is 1x1μm^2.

The AFM image of LB film of DODA/PEG–SWCNTs (Fig.5.11(a)) shows long strand–like domains. The width of the strands are ∼50 to 60 nm. These strand–like domains may represent the PEG–SWCNTs adsorbed over LB film of DODA. Fig.5.11(b) shows globular domains which are due to the adsorption of DNA on the functional layer.

5.4 Conclusion

The LM and LB films of cationic surfactants is very interesting not only for understanding the fundamental science involving the molecular interactions at the interfaces but also its application for attracting and trapping of anionic analytes during sensing process. Here, we studied the LM and LB films of the cationic surfactants. We formed the LB films of DOAB and studied the DNA sensing application. The lowest detectable concentration of DNA in the liquid is found to be 20 fM. The kinetic study indicate the characteristic time for DNA adsorption over the LB film of DOAB is ∼162 seconds. The effect of PEG–SWCNTs in the aqueous subphase on the LM of DODA is studied as the function of pH of the subphase. We found that the association of PEG–SWCNTs with LM of DODA is better at the ultrapure water subphase than that compared with aqueous basic subphase. We formed the LB film of DODA and DODA/PEG–SWCNTs at $\pi_t = 10$ mN/m from the ultrapure water subphase and characterized using FESEM. The FESEM image clearly shows the formation of LC domains in form of small domains and big dendritic domains. The LB film of DODA/PEG–SWCNTs also reveals the presence of nanotubes on the monolayer matrix of DODA. The DNA sensing studies of LB films of DODA/PEG–SWCNTs indicate that the lowest detectable concentration of DNA in aqueous medium is $\sim$3 fM which is far lower than that of the LB film of DOAB. The piezoresponse signal obtained from CNTs incorporated film are much stable than that of pure organic surfactant layer. The presence of SWCNTs in the functional layer for sensing may provide mechanical strength to the film against any dissolution of the surfactant in the fluid medium. Our studies indicate that presence of SWCNTs in the functional layer for sensing can provide several advantages including sensitivity, stability and reproducibility.

Chapter 6

Langmuir–Blodgett films of carboxylated graphene and its application as urea sensor

6.1 Introduction

In the previous chapters, we have discussed our studies on Langmuir monolayer and Langmuir–Blodgett (LB) films of pristine and functionalized single–walled carbon nanotubes (SWCNTs). The LB films of such SWCNTs are fabricated and their sensing properties are compared with that of spin coated/drop casted films. We found the sensing characteristics of the highly organized SWCNTs in LB film is far better than that of random network of the SWCNTs in spin coated/drop casted film. The improved performance can be related to ordering in the LB film which may facilitate the nucleation followed by the growth of domains of the analytes. Graphene is another class of carbon nanomaterials which is gaining tremendous scientific attention due to its unique physicochemical properties such as high surface area [241], excellent thermal and electrical properties [242, 243], strong mechanical strength [244]. The honeycomb structure can be used for trapping and holding the gas molecules [91]. Graphene as well as their functionalized form have been utilized for various applications in optoelectronics [92], sensors [93, 94], and electrochemistry [245, 246]. In addition to numerous electrical, optical and mechanical devices, graphene can be employed for sensing applications. The delocalized π electrons of the graphene can attract and trap the molecules (analytes) through π–π interaction. The graphene can be functionlized organically so as to establish molecular–specific interaction. This is the most important underlying principle for the development of a sensor specific to a particular analyte. Graphene can interact with wide variety of organic molecules by noncovalent forces (hydrogen bonding, electrostatic force, van der Waals force and hydrophobic interaction) [247–250]. Because of its interesting properties, a thin film of carboxylated graphene has found its way into a wide variety of electrochemical biosensors [96]. In this chapter, we discuss our studies on Langmuir film (LF) of functionalized (carboxylated) graphene (G–COOH). The study on interaction of G–COOH with urea at the air–water (A/W) interface suggests that the LB film of G–COOH can be a potential functional layer for sensing urea in the liquid phase. Using quartz crystal microbalance (QCM), we studied the urea sensing application of LB films of G–COOH. The sensing performance of LB film is found to be better compared to that of spin coated film of G–COOH. The sensing of urea in milk sample is also studied using the LB and spin coated film of G–COOH.

The possible synthesis strategies of edge–carboxylated graphene (ECG) through a high energy ball mill and ECG nanoflakes from nitric acid oxidized arc–discharge material has been reported [251, 252]. Myung *et al.* [253] have reported the ECG nanoplatelets as oxygen–rich metal–free cathodes for organic dye–sensitized solar cells. Urea is an organic compound present in the urine of mammals and is synthesized from the metabolism of nitrogen containing compounds like proteins, etc. Presence of a high concentration of urea in the body is a major indicator of kidney failure. On the other hand, urea is also one of the main adulterants found in synthetic milk [254, 255]. A cut off limit for urea concentration in milk is normally accepted at 70 mg/dl ($\sim$12 mM). The presence of urea above this cut off limit in milk can cause severe health problems for human beings, such as, indigestion, acidity, ulcers, cancer and malfunctioning of kidneys [256, 257]. Exploiting new materials like graphene, which has been reported as highly efficient for ballistic conductance and amperometeric sensing, can give a unique platform for sensitive and specific sensors. Therefore, the development of a urea sensing platform with better accuracy and precision is of utmost importance. Various methods have been reported for the determination of urea. Amperometric sensing of urea using edge activated graphene nanoplatelets has been proposed by Kumar *et al.* [258] in 2015. On the other hand Verma *et al.* [259] have showed the fabrication and characterization of SPR probes on a single optical fiber for the parallel sensing of urea and glucose using wavelength interrogation method.

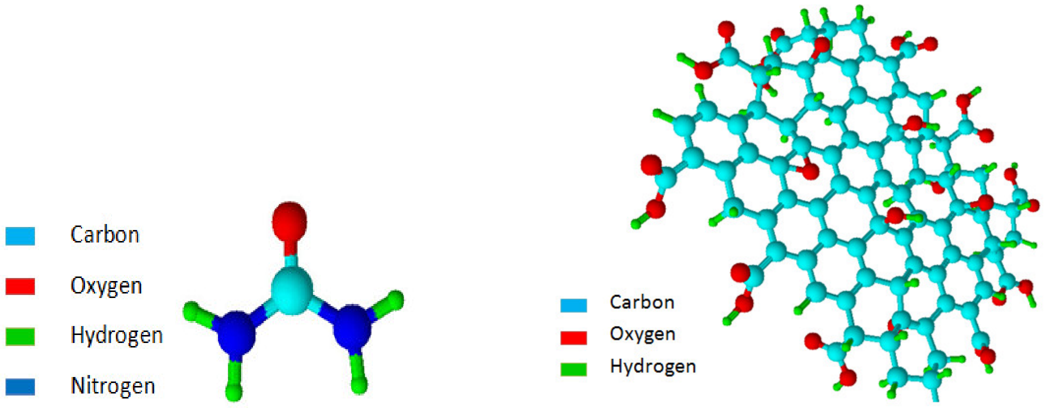

(a) (b)

FIGURE 6.1: Molecular structure of (a) Urea and (b) Carboxylated graphene (G–COOH).

In our studies, we obtained a stable and reversible LF of G–COOH at the A/W interface. We fabricated a single layer of LB film of the G–COOH onto hydrophilically treated silicon substrates at target surface pressure (π_t) of 5mN/m and surface morphology was studied using field emission scanning electron microscope (FESEM). The charge–transfer mechanism in the LB film was found to be of the Arrhenius type where the current flows due to hopping of charges between the nearest–neighbor sites. The presence of urea in aqueous subphase affect the LF of G–COOH at the A/W interface. This indicates that the functional layer of G–COOH can be employed for sensing urea in a liquid phase. Recently, in a study Yao *et al.* [123] have demonstrated the chemically derived graphene oxide thin film as humidity sensitive coating deposited on quartz crystal electrodes for humidity detection in the range of 6.4–93.5%. In this chapter, we present studies on LB film of G–COOH employed for urea sensing and the sensing performance of LB film is compared to that of spin coated film of G–COOH.

6.2 Experimental methods

6.2.1 Langmuir and Langmuir–Blodgett Film

The carboxylated graphene (G–COOH) and urea were purchased commercially from Redex Technologies Pvt. Ltd. and S D Fine–Chem Ltd., respectively and were used without any further purification. Fig.6.1 represents the chemical structure of urea and G–COOH. A solution of concentration of 0.05 mg/ml of G–COOH is formed in high–performance liquid chromatography (HPLC) grade chloroform. Uniformly dispersed solution of G–COOH is obtained by ultrasonicating the G–COOH solution for 30 minutes. The solution is then filtered using a filter paper. The water used in experiments was ultrapure ion–free having the resistivity greater than 18 MΩ–cm (Millipore, DQ–5). The concentration of the urea solution was 9.5 μM in water subphase. The pH of the subphase was altered by the addition of ammonia solution. The pH of the subphase was monitored continuously using a pH meter. The average pH value was 8.2. The average pH value of ultrapure water was 5.7. This is due to the absorption of atmospheric CO_2 by the ultrapure water and the formation of weak carbonic acid. The LF of G–COOH was formed by spreading 4 ml of the filtered solution very slowly using a micropipette (Tarsons) onto ion–free water subphase between the two barriers of the LB trough. About 30 minutes time was allowed for the solvent to evaporate from the surface of the water leaving behind the dispersed G–COOH. The surface pressure (π) – area (A) isotherm is recorded by compressing the monolayer of G–COOH symmetrically using the two barriers of the LB trough and recording the surface pressure simultaneously using an integrated balance. Here, the area refers to area of the film at the A/W interface enclosed between the two barriers of the LB trough. The LF of G–COOH is transferred onto different solid substrates by the vertically dipping mechanism of LB technique. The LB films were deposited at target surface pressure

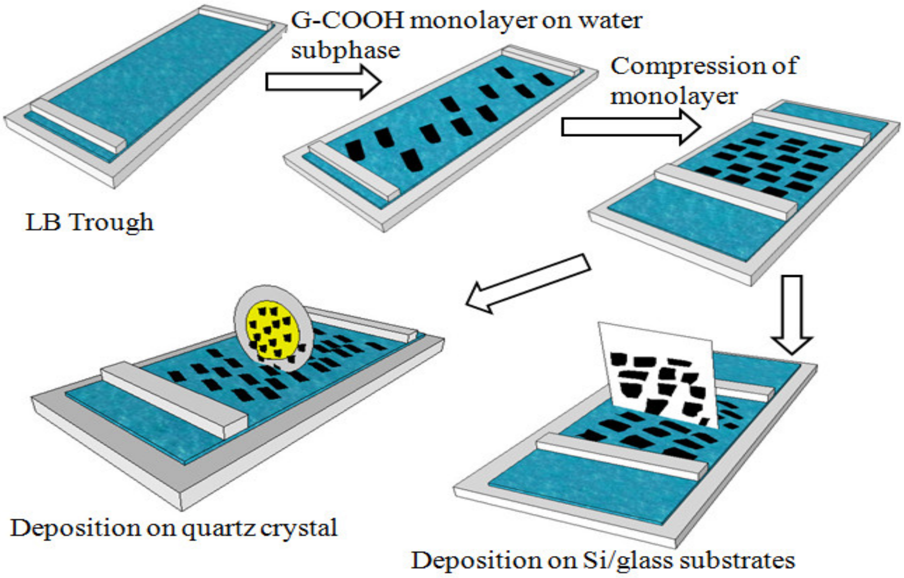

FIGURE 6.2: Schematic diagram for the formation of LB of G–COOH on gold–coated quartz crystal, Si/SiO_2 and glass substrates.

(π_t) = 5 mN/m corresponding to liquid–like phase of the LF of G–COOH. The spin coating was done by spreading 200 μl of filtered G–COOH solution in the HPLC grade chloroform solvent onto Si substrate. Deposition was done at spinning rate of 2500 rotations per minute. The experiments were carried out at room temperature ($\sim 22^o$ C). Fig.6.2 represents a schematic diagram for the formation of LF of G–COOH on gold–coated quartz crystal and other solid substrates.

6.2.2 Atomic Force Microscopy

The surface topography of the LB films of G–COOH deposited on substrates was obtained by scanning the films using an atomic force microscope (AFM) in the contact mode. The films were scanned using silicon tips having the spring constant 0.1 N/m.

6.2.3 Field Emission Scanning Electron Microscopy

The surface morphology of the LB film was obtained using a field emission scanning electron microscope (FESEM). The extra high tension (EHT) voltage was maintained at 1–2 kV.

6.2.4 Raman Spectroscopy

The LB film of G–COOH deposited onto glass substrate at $\pi_t = 5$ mN/m was scanned using a Laser Raman Spectrometer (STR250). The sample was excited with a 532 nm diode–pumped solid–state (DPSS) laser.

6.2.5 Fourier Transform Infrared (FTIR) Spectroscopy

The FTIR spectra of LB film of G–COOH/urea deposited onto Si/SiO_2 substrate at $\pi_t = 5$ mN/m were recorded using FTIR system (Perkin Elmer).

6.2.6 X–Ray Diffraction

The X–ray diffraction (XRD) technique was used to study the crystallinity of the LB films of G–COOH. The thin film of the G–COOH deposited onto Si/SiO_2 substrate was placed in powder X–ray diffractometer (PANalytical XPERT– PRO). The diffraction data was acquired by exposing samples to Cu–K_α X–Ray radiation, which has a characteristic wavelength (λ) of 1.54Å, with an operating voltage and current maintained at 40kV and 40mA. The data was collected between scattering angles (2θ) 5–60^o at a scanning rate of 2^o min^{-1}.

6.2.7 Current–Voltage Measurement

The in–plane charge–transport mechanism in the LB film and spin coated film of G–COOH was studied by recording current – voltage (I–V) curves at different temperatures using a source meter (Keithley, model No. 2400). For the I–V measurements, the films were deposited onto interdigitated electrodes (IDE) fabricated by a process as discussed in chapter 1. The temperature was regulated using a home–built proportional integral derivative (PID) controlled heater with an accuracy of 0.01^{o}C.

6.2.8 Quartz Crystal Microbalance Measurements

We have investigated the interaction of urea with a highly ordered ultrathin LB film and spin coated film of G–COOH using quartz crystal microbalance (QCM200, SRS, USA). The AT–cut gold–coated quartz crystals exhibiting a resonance frequency of 5 MHz were employed as the sensing element. The quartz crystals were deposited with G–COOH film by LB and spin coating techniques. Prior to deposition the quartz wafers were cleaned in cold piranha solution (conc. H_2SO_4:H_2O_2 as 3:1) and rinsed successively with plenty of ion–free water, alcohol and acetone thoroughly. The functionalized quartz wafer was immersed into the beaker filled with 200 ml aqueous medium. A 166.5 mM concentration of stock solution of urea was prepared in ultrapure water. The urea solution was injected into the beaker through a micropipette and the change in frequency (Δf) due to the adsorption of urea was recorded as a function of concentration of urea in the aqueous medium. We have successfully sensed variable ranges of urea concentrations from 8.32 μM to 249.72 μM.

6.3 Results and discussion

6.3.1 Surface Manometry

The surface manometry on the G–COOH was performed by forming its LF at A/W interface. The $\pi - A$ isotherms of LF of G–COOH at A/W water interface with and without urea at various pH values in the aqueous subphase are shown in Fig.6.3. The isotherm of the LF of G–COOH on the ultrapure water subphase (Fig.6.3(a)) shows negligible π at large A until the film is compressed at 400 cm^2 . This is the gas phase of LF of G–COOH. The surface pressure rises sharply thereafter until the film is compressed completely in the trough. The sharp rise in π indicates the onset of a liquid–like phase of the G–COOH. The isotherm indicates a maximum π of about 17mN/m. The signature of collapse is not evident from the isotherm. On increasing the pH of the subphase to 8.2, the film expanded and the isotherm (Fig.6.3(b)) shifts

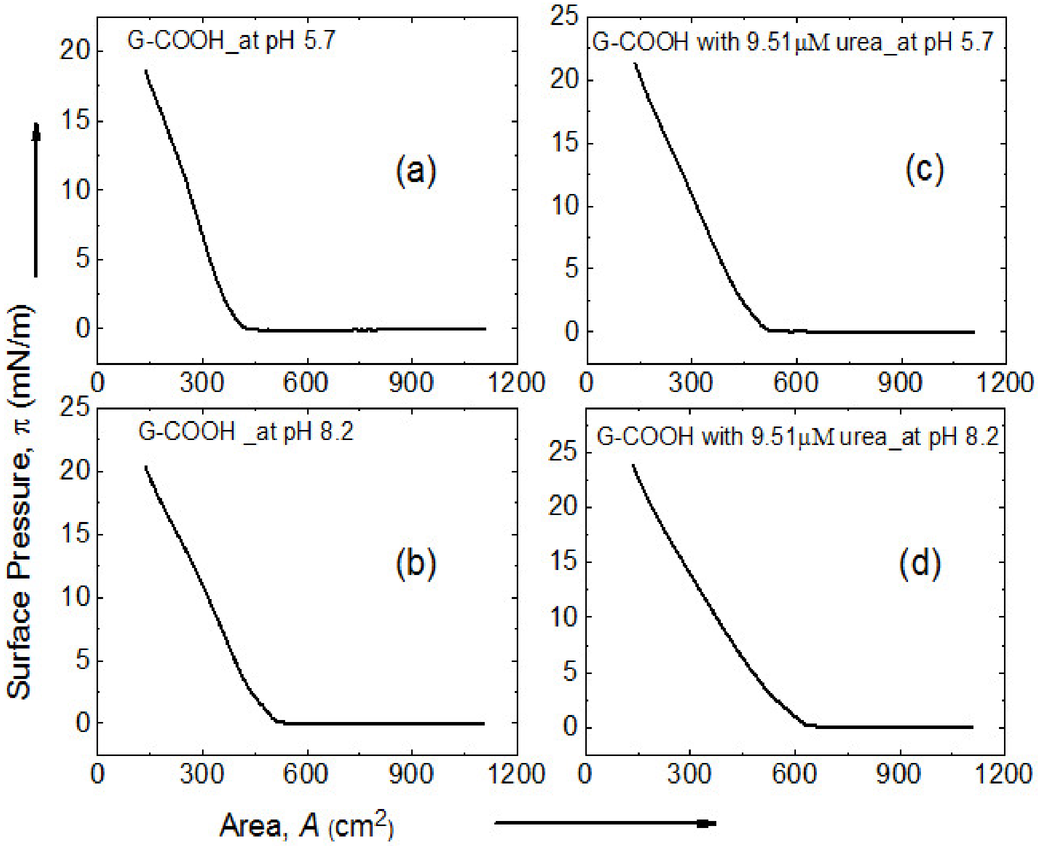

Figure 6.3: Surface pressure (π) – area (A) isotherms of LF of G–COOH (a and b) and G–COOH/urea (c and d) at different pH value of water subphase.

towards higher value of A. The lift off area of the isotherm is increased to 500cm^2 with increase in pH value of water subphase by 8.2. The –COOH group of graphene tend to ionize in the basic medium. The monolayer is expanded due to electrostatic repulsion between such ionized –COOH group of the graphene.

To study the interaction of urea dispersed in the aqueous subphase with the LF of G–COOH, 9.51 μM concentration of urea was added to the ultrapure water subphase (Fig.6.3(c)) and to the aqueous subphase with pH 8.2 (Fig.6.3(d)). The trend of the isotherms appear similar to that of subphase without urea. However, the lift–off area increases to higher values due to the incorporation of urea in the subphase. The lift–off areas estimated from the isotherms are found to be 520 cm^2 and 630 cm^2 in the case of urea in ultrapure water subphase and urea in water subphase with pH 8.2, respectively. The enhanced values of lift–off area indicate a strong interaction of urea with that of LF of G–COOH. The amine group (NH_2) of urea may interact with –COOH group of the G–COOH to form a complex. This leads to shifting of the isotherms towards higher values of A. The shifting of the isotherm of LF of G–COOH on urea containing aqueous subphase of pH 8.2 is largest. This is due to ionization of carboxylic group of the G–COOH leading to a enhanced interaction between urea and the graphene.

The variation of the in–plane elastic modulus (E) of LF as a function of A of the LF of G–COOH and G–COOH/urea at different pH values are shown in Fig.6.4. The variation of E as the function of A shows a peak corrpesponding to the liquid–like phase of the LF of G–COOH over the aqueous subphases with and without urea. The maximum value of E in the liquid–like phase lies in the range of 21 to 25 mN/m which is comparable to the liquid–like phase of LF of some reported hydrophobic polymers [136]. This indicates that the elasticity of the LF of G–COOH does not vary much due its interaction with urea even in the basic pH. The liquid like phase destabilizes upon further compression, leading to a decrease in the value of E. Such a destabilization of E is an indication of the initiation of the collapse of the film. Though the collapse of the LF of G–COOH was not evident from the isotherm, the indication of the collapse can be seen from the elastic modulus curves.

The stability of the LF of G–COOH is studied by compressing and expanding the film repeatedly and recording corresponding surface pressure (known as isocycles). Fig.6.5 shows the isocycles of the LF of G–COOH at the A/W interface. The isocycle measurement shows negligible hysteresis in the compression and expansion curves. In the isocycle measurement, the expansion curve almost follows the compression curve.

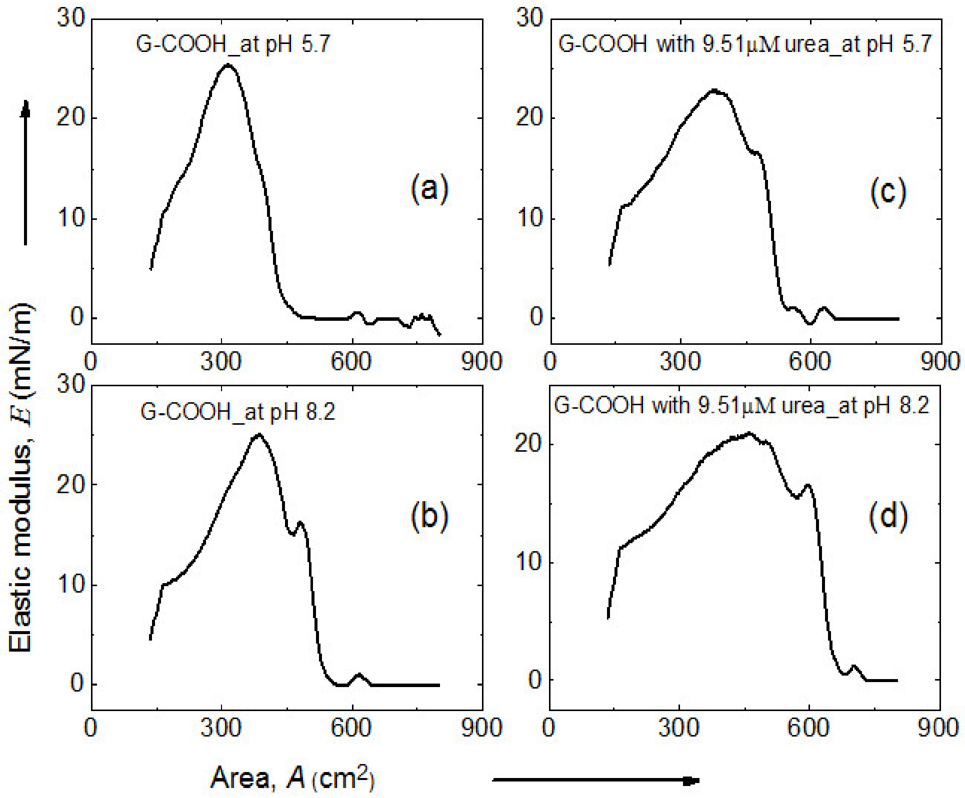

FIGURE 6.4: The isothermal in–plane elastic modulus (E) as a function of A of (a and b) LF of G–COOH and (c and d) G–COOH/urea at different pH value of water subphase.

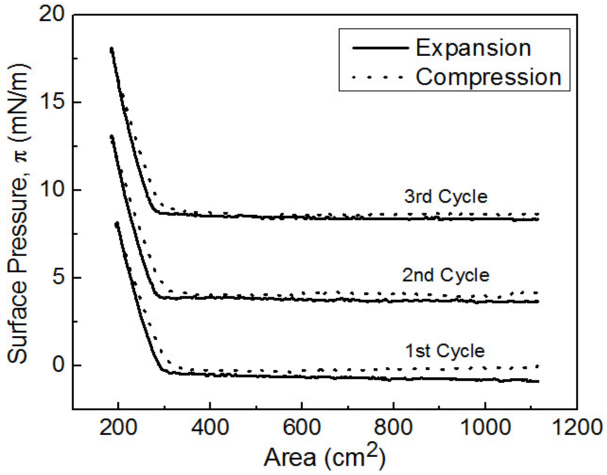

FIGURE 6.5: Isocycles of LF of filtered graphene at the A/W interface. The film was compressed to maximum surface pressure of 8 mN/m. The curves for second and third cycles are shifted vertically by 5 mN/m relative to each other for visual clarity.

This indicates that the liquid–like phase is completely reversible. The isocycle curves indicate that the film of G–COOH at the A/W interface is stable and reversible. The stability of LF of G–COOH at the A/W interface might be due to amphiphilic nature of G–COOH. The presence of –COOH group provides sufficient hydrophilicity to the hydrophobic graphene sheet.

6.3.2 FESEM and AFM Characterization

The surface morphology of LB film and spin coated film of G–COOH was studied using FESEM. The LB films of G–COOH are deposited in the liquid–like phase at $\pi_t = 5$ mN/m onto Si/SiO$_2$ substrates. The surface morphology of LB film and spin coated film of G–COOH is shown in Fig.6.6. Functionalized graphene is found to aggregate in spin coated sample as shown in Fig.6.6(a).

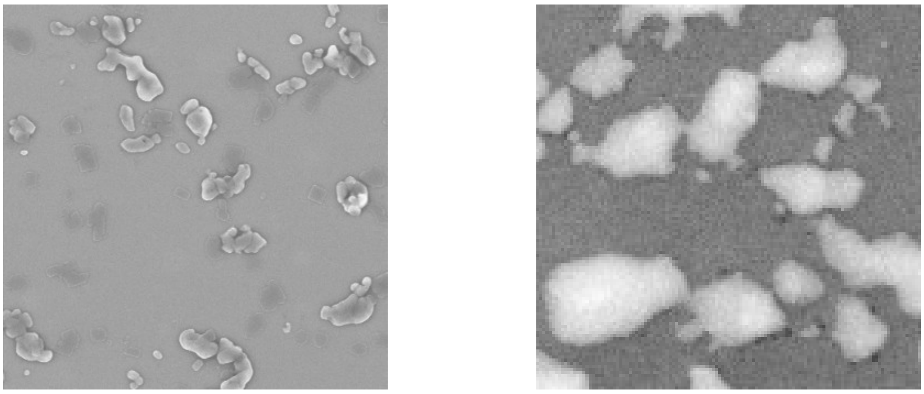

(a) (b)

FIGURE 6.6: FESEM images of (a) spin coated film (b) LB film of filtered G–COOH deposited $\pi_t = 5$mN/m onto Si/SiO$_2$ substrate. The size of each image is 10x10 μm^2.

In the LB film of G–COOH, the graphene sheets are mostly lying flat over the Si/SiO$_2$ substrate without any aggregation as can be clearly seen in Fig.6.6(b). The flat graphene flakes over the entire area of substrate help to improve the interaction between functional group of graphene and urea.

In order to study the morphology at lower length scale, the surface topography of the LB films of G–COOH was obtained by scanning the films using AFM in contact mode. The LB films of G–COOH are deposited at $\pi_t = 5$ mN/m onto Si/SiO$_2$ substrates. Fig.6.7 shows the AFM image depicting the surface topography of the single layer

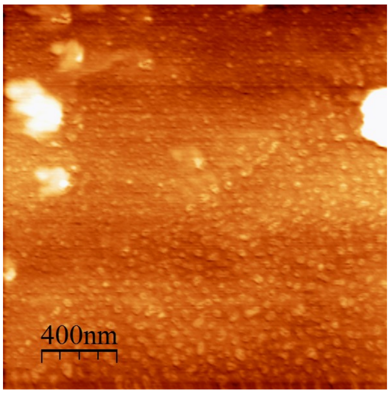

Figure 6.7: AFM images of LB film of G–COOH deposited onto Si/SiO$_2$ substrate in the liquid–like phase at $\pi_t = 5$mN/m. The size of image is 2x2 μm^2.

LB film of G–COOH deposited onto Si/SiO$_2$ substrate. The AFM images reveal the stacking of the graphene flakes onto solid substrates. In addition, small domains of graphene sheets (∼20–30nm) are observed all over the Si/SiO$_2$ substrate. Fig.6.8 shows the surface topography of the single layer LB film of G–COOH with different concentration of urea in the ultrapure water subphase deposited onto the Si/SiO$_2$ substrate.

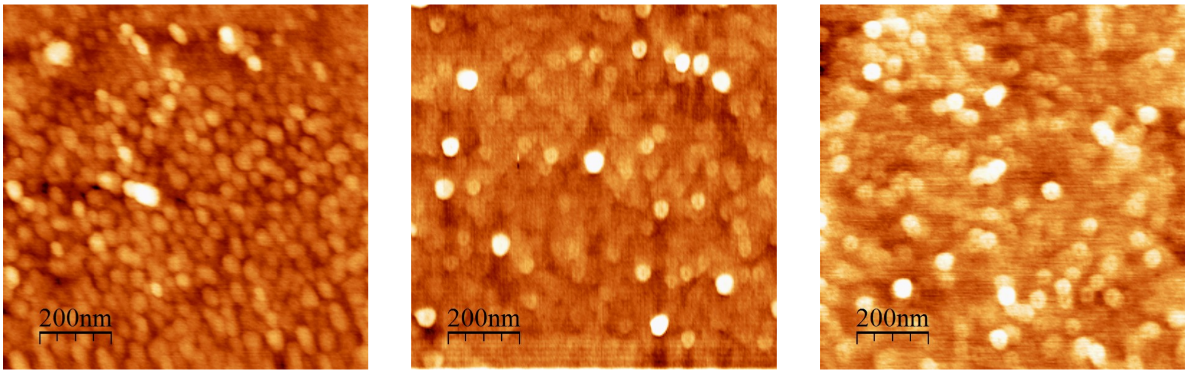

(a) (b) (c)

Figure 6.8: AFM images of LB film of G–COOH with (a) 4.75 μM urea (b) 9.51 μM urea and (c) 95.14 μM urea in ultrapure water subphase deposited onto Si/SiO$_2$ substrate. The size of each image is 1x1 μm^2.

The AFM images reveal the circular patches of small domains distributed over the substrate. These circular patches are representing the stacking of graphene sheets. The brightness of some domains are significantly large due to adsorption of urea over the G–COOH. Density of such domains as a function of concentration of urea increases. At lower concentration of urea, a few domains are observed in Fig.6.8(a). Further increase in concentration of urea enhances the number of bright domains over stacked domains of G–COOH (image b and c of Fig.6.8). The images were obtained in 8–bit grayscale having the dimension 256×256 pixels. The images were thresholded to segment the brighter domains representing the urea adsorbed domains. Such domains are counted for a set of images of different concentrations of urea to plot a bar diagram as shown in Fig.6.9. The bar diagram shows a dependence of number of bright domains representing the urea domains with concentration of urea. It can be seen that average number of bright domains increases by increasing concentration of urea from 4.75 – 95.14 μM.

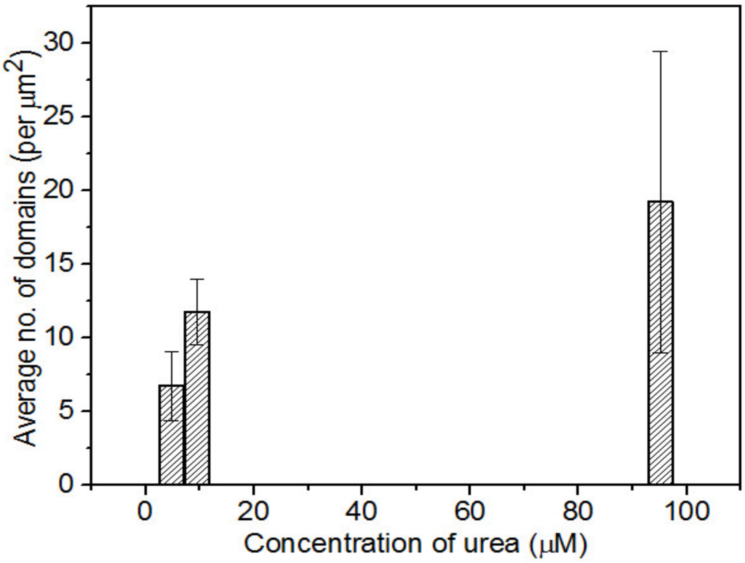

FIGURE 6.9: Average number of bright domains as a function of urea concentration.

6.3.3 Fourier Transform Infrared Spectroscopy

FTIR is used to further investigate the interaction of urea with G–COOH. The FTIR spectra of urea powder and LB films of G–COOH with 9.5 μM concentration of urea in water subphase deposited onto Si/SiO$_2$ substrates at π_t= 5mN/m are shown in Fig.6.10. In urea powder (Fig.6.10(a)) the absorbance band corresponding to N–H stretching (γ(N–H)) and N–H rocking (ρ(N–H)) are observed at 3430 and 1146 cm^{-1}. In Fig.6.10(b), the absorbance band corresponding to O–H stretching (γ(O–H)) and O–H bending(δ(O–H)) vibrations in G–COOH are observed at 2930 and 1382 cm^{-1} respectively. Due to the binding of amine groups of urea and carboxylic groups of

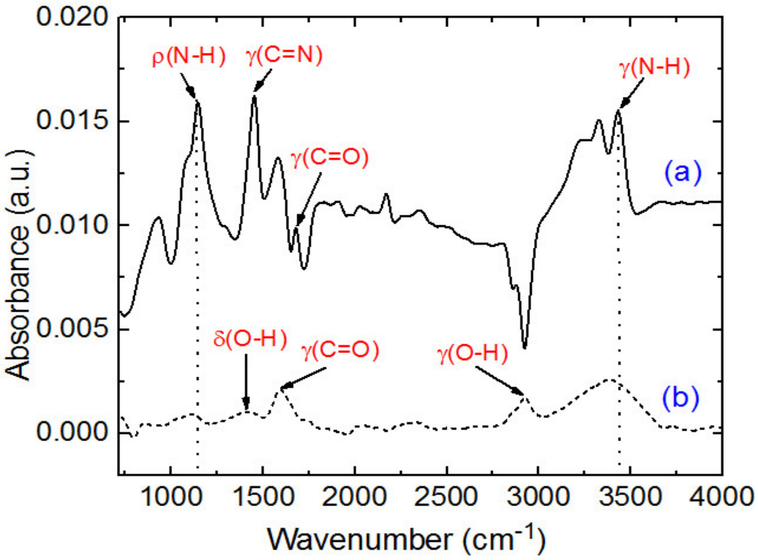

FIGURE 6.10: FTIR spectrum for (a) urea powder and (b) LB film of G–COOH/urea deposited at π_t = 5 mN/m. Concentration of urea in water subphase is 9.51μM.

G–COOH, the high wavenumbers γ (N–H) and ρ (N–H) absorption band in urea 3430 cm^{-1} and 1146 cm^{-1} are shifted to lower wavenumbers 3387 and 1113 cm^{-1} in the LB film of G–COOH/urea. The FTIR peak at 1592 cm^{-1} (γ(C=O)) clearly indicates the presence of carboxylic group in graphene. FTIR spectra thus indicate a strong binding of amine group from urea to carboxylic groups of the G–COOH.

6.3.4 Raman Spectroscopy

Raman spectroscopy is a powerful technique for obtaining an indication of the structure and quality of carbon nanomaterials. Therefore, Raman spectroscopy was utilized to examine the structure of the LB film of G–COOH. Fig.6.11 shows the Raman spectrum for LB film of single layer of G–COOH deposited onto glass substrate at π_t = 5 mN/m. The Raman spectrum contains the prominent peaks at 1590 and 1356 cm^{-1} corresponding to the well documented G and D bands. It is well known that the G band is a primary in–plane vibrational mode [251]. G–band arises from the stretching of the C–C bond in graphitic materials, and is common to all sp^2 carbon systems. The D–band in carbon materials is generally associated with the presence of disorder such as defects [252]. The calculated intensity ratio of D to G (I_D/I_G) for LB film of G–COOH is approximately 0.55, suggesting significant edge functionalization.

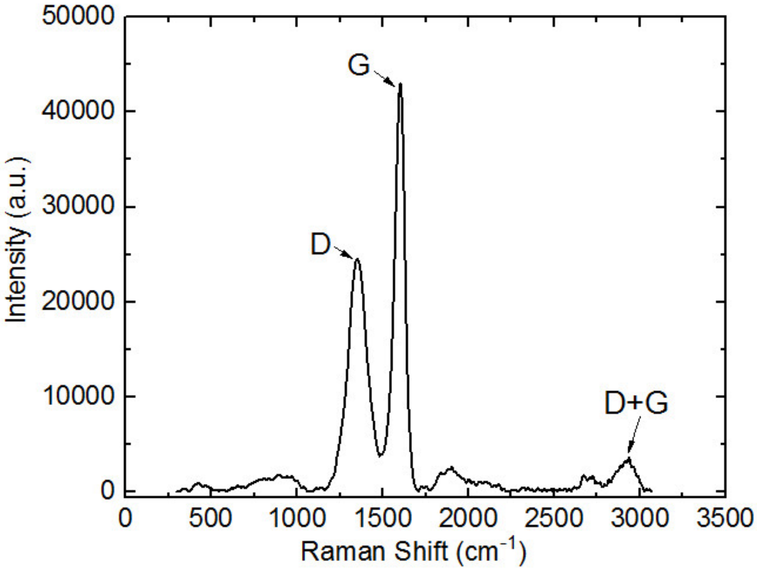

FIGURE 6.11: Raman spectrum of LB film of G–COOH deposited on glass substrate at $\pi_t = 5\text{mN/m}$.

The frequency peak at 2926 cm^{-1} corresponding to D+G band can be observed in Raman spectrum of LB film of G–COOH. The D+G band is a defect activated process of the D–band.

6.3.5 X–Ray Diffraction

The crystalline property of the LB film of G–COOH was studied using X–ray diffraction. Fig.6.12 shows the XRD profile of the films of G–COOH grown by the LB technique and spin coating method. The intense peak position at the 24.8° (002) is characteristic of the LB film of G–COOH [260]. The sharp peaks indicate the highly crystalline nature of the LB film of G–COOH. The crystallite size is calculated from full width at half maximum of the peaks using the Scherrer equation [261].

$$D = \frac{K\lambda}{\beta \cos\theta} \tag{6.1}$$

The intense peak position at the 28.4° (100) is characteristic of the urea, (Fig.6.12 (b)). The average crystallite size of graphene sheets was calculated using Eq.6.1 and found to be around 10.7 nm for spin coated and LB film of G–COOH. The average crystallite size for LB film of G–COOH/urea was found to be about 8.1 nm. The (311) peak around 56° is corresponding to the silicon substrate.

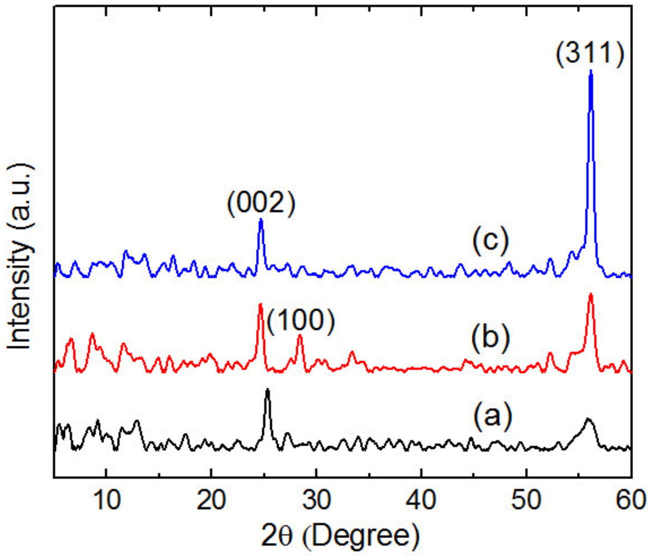

FIGURE 6.12: The XRD patterns for the (a) LB films of G–COOH, (b) G–COOH/urea and (c) spin coated film of G–COOH.

6.3.6 I–V Measurement

The charge–transport mechanism in the LB film of G–COOH was investigated by current–voltage (I–V) measurement in current–in–plane (CIP) geometry. The LB and spin coated films were deposited onto the IDEs with an interelectrode separation of 100 μm. The I–V curves of LB film and spin coated film of G–COOH (Fig.6.13a and 6.13b) show the nonlinear behavior of the current as a function of applied voltage. The trend remains the same, however the slope increases with increasing temperature (T). The differential conductance (G = dI/dV) was calculated at different temperatures, and $ln(G)$ versus $1/T$ is plotted in Fig.6.14. We found a linear fit to the data corresponding to the both films indicating the Arrhenius behavior of the charge transport, *i.e.*, classical hopping of individual charges between nearest neighbor sites. The activation energy is found to be 1.23 eV and 0.78 eV for LB film and spin coated film of G–COOH. Due to ultrathin nature, the perforation and hence the number of defects in LB film of G–COOH are expected to be more. Therefore, hopping phenomena is predominant in LB film compared to that of spin coated film of G–COOH.

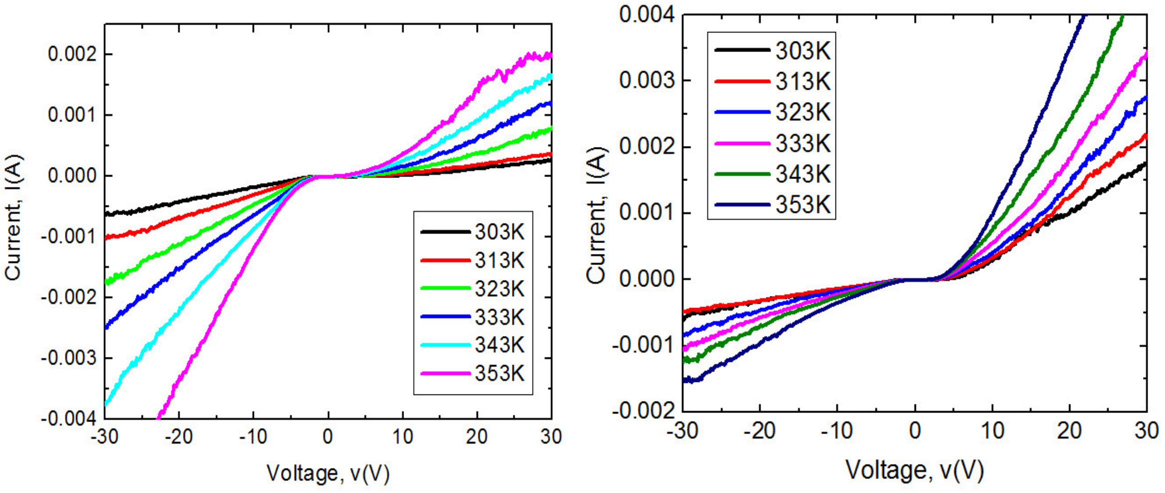

(a) (b)

Figure 6.13: Current – voltage (I–V) curves of the (a) LB films of G–COOH and (b) spin coated film of G–COOH at different temperature.

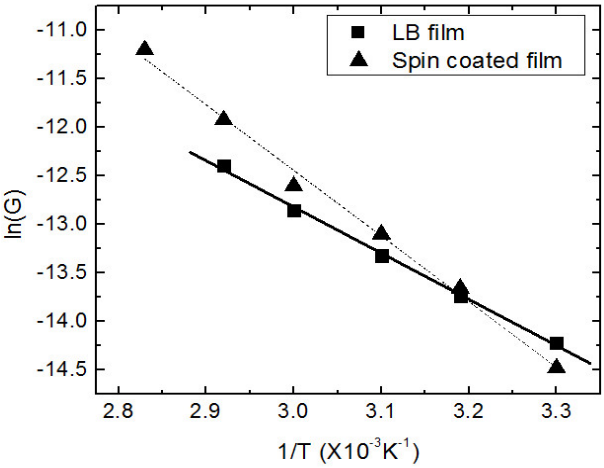

Figure 6.14: Arrhenius plot for spin coated film and LB film of G–COOH.

6.3.7 Quartz Crystal Microbalance Measurements

In order to study the sensing application of the films of G–COOH using a QCM, the LB and spin coated films of G–COOH were deposited onto the quartz crystal wafers. Any change in the mass in the liquid phase due to adsorption of molecules on the surface of crystal is sensed as the change in the resonance frequency (Δf) relative to the pure aqueous medium. The change in mass per unit area on the surface of crystal is calculated using the Sauerbrey relation (Eq.1.4). The G–COOH functionalized gold–coated quartz wafer was immersed into the urea solution of known concentration and the change in mass due to adsorption of urea is recorded. The variation in change is mass of adsorbed urea onto the LB film (Fig.6.15(a)) and spin coated film (Fig.6.15(b)) as a function of concentration of urea in the ultrapure water medium is studied. Both the curves (Fig.6.15) show a linear trend in the concetration range of 8.325 μM to 249.72 μM which is a good indication for the development of a urea sensor. The lowest detectable concentration of urea by the LB film and spin coated film of G–COOH is around 8.32 μM and 41.62 μM, respectively. Assuming linear dependency of the mass adsorbed vs concentration of urea, the calculated slope values of the data for LB film and spin coated film of G–COOH are 42.5 and 12.9 $ng/cm^2/\mu$M, respectively. The sensitivity of a sensor towards an analyte is proportional to the slope of such curves [185]. Therefore, the sensitivity of LB film of G–COOH towards urea sensing is more than 3 times as compared to that of spin coated film of G–COOH. This study clearly highlights the potential of LB film of G–COOH as a sensitive and low concentration detectable urea sensor.

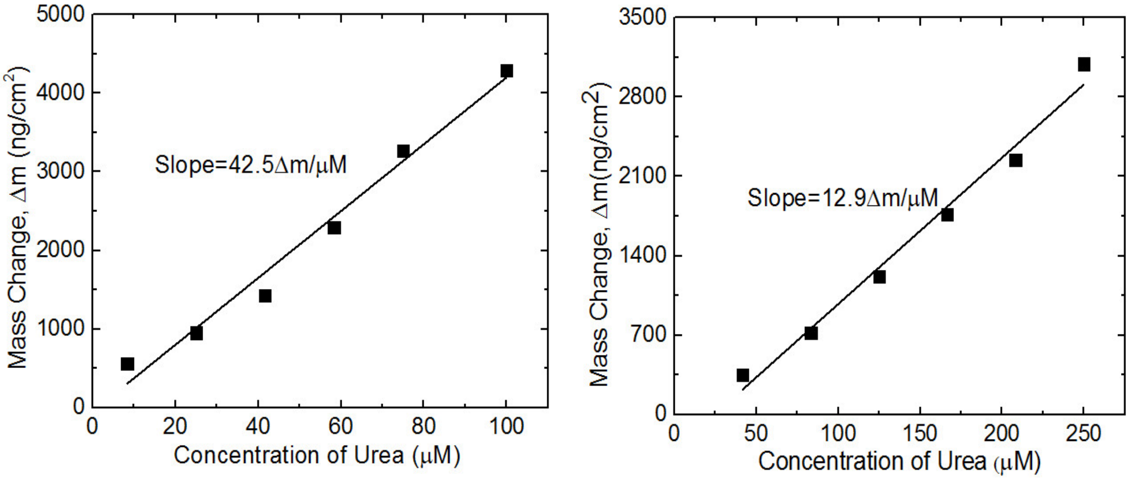

(a) (b)

FIGURE 6.15: Adsorption of urea onto gold–coated quartz crystal deposited with (a) LB film of G–COOH at $\pi_t = 5mN/m$ and (b) spin coated film of G–COOH.

In order to study the sensing of urea in milk sample using the films G–COOH as the functional layer on the gold–coated quartz crystal wafer, the milk samples with urea as additive were investigated. The milk sample was prepared by adding 500 μl volume of less concentrated milk into 200 ml ion–free ultrapure water. The concentration of urea in such diluted milk is varied systematically and the change in mass is recorded.

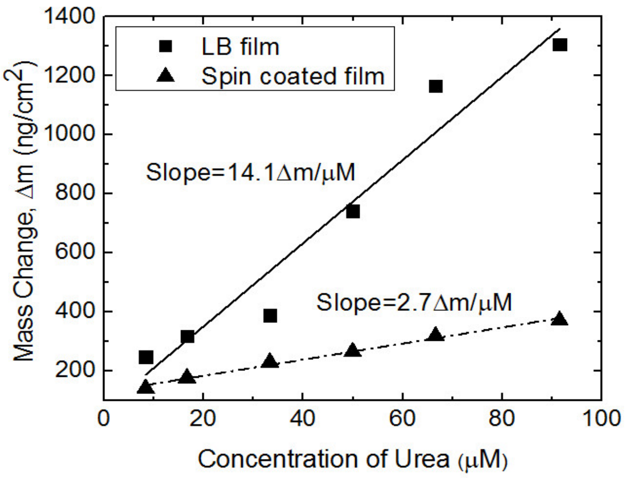

FIGURE 6.16: Mass change vs urea concentration curves for LB film and spin coated film of G–COOH over gold–coated quartz crystal. 500μl milk was added to 200ml ion–free Millipore water.

Fig.6.16 shows the mass adsorption of urea onto ultrathin LB film and spin coated film of G–COOH when exposed to the urea containing diluted milk sample. The lowest detectable concentration of urea by the LB film and spin coated film of G–COOH is around 8.32 μM. The calculated slope values for mass adsorption curves of LB film and spin coated film of G–COOH are 14.08 and 2.73 $ng/cm^2/\mu$M, respectively. Our studies indicate the functional layer of G–COOH deposited through LB technique can be employed for the detection of urea of very low concentration. We have demonstrated that even in the presence of other species (*e.g.* milk proteins and minerals), the presence of urea can be detected.

6.4 Conclusion

Graphene is one of the extraordinary carbon based nanomaterials which can be employed for numerous device applications. Graphene can be oraganically functionalized for ease of device processability and dispersion in a host. The G–COOH is one of the important chemically modified graphene which has a potential for chemical and biological sensing. The –COOH group of the graphene can form complex with different proteins and biologically relevant molecules. In this chapter, we discuss the formation and characterization of LF and LB films of G–COOH. The LF of G–COOH at the A/W interface is found to be very stable and reversible. The urea in aqueous subphase is found to interact strongly with LF of G–COOH at the A/W interface indicating that the LB film of G–COOH can be employed as functional layer for urea sensing. The functional layers of G–COOH were formed over the quartz crystal wafers by LB and spin coating techniques, and employed for sensing urea in aqueous medium. The response is found to be linear in the given concentration range. The lowest detectable concentration of urea in water by LB film was found to be very low (8.32 μM). The sensing performance of LB film of G–COOH is found to be better than that of spin coated film of G–COOH. The detection of urea in milk sample using the functional layers of G–COOH is also studied. The study on sensing of urea in milk sample indicate that the LB film of G–COOH can be employed for sensing urea even in the presence of differnt other species in the aqueous medium.

Chapter 7

Conclusions and Future Scope of Our Studies

7.1 Conclusions

Thin films science and technology is one of the important fields of research and development. The reduction in the dimension of bulk material and approaching to a limit of two–dimensional (2D) system by fabricating ultrathin films of the material provides a remarkable increase in surface–to–volume ratio as compared to the bulk material. Such huge increase in surface–to–volume ratio increases the activities of the material enormously and thereby the material properties like catalysis, reactivity, adhesion, etc enhances remarkably. Such changes in the material properties in the state of ultrathin films promises a wide range of applications starting from the basic science research to various device fabrication. The ultrathin films can be fabricated either top–down or bottom–up mechanism. In this thesis, we discuss bottom–up mechanism for the fabrication of the ultrathin films. In the bottom–up mechanism, the films are fabricated by arranging the molecules in the defined molecular states in a single layer onto some substrates. It has been realized that the field of ultrathin films has a close association with nanoscience and nanotechnology, and therefore due to such multidimensional application, the field is strengthening everyday. This thesis discusses the studies on ultrathin films of carbon based nanomaterials e.g. single–walled carbon nanotubes and graphene. The films were formed at different interfaces viz. air–water (A/W) and air–solid (A/S) and characterized by different techniques. The ultrathin film of the nanomaterials were fabricated using Langmuir–Blodgett (LB) technique and the sensing application of the LB film was compared with that of spin coated/drop casted thin films. We report that the sensing performance of LB films of the nanomaterials is better than that of spin coated/drop casted thin films.

The introduction to the systems like Langmiur monolayer (LM) and LB films and their characterization techniques are discussed. The materials forming LM and LB films are illustrated. The recent development in the field and the identified research gap are also discussed. This is discussed in chapter 1.

In chapter 2, we report the formation of a stable and reversible LM of bundles of single–walled carbon nanotubes (SWCNTs) at the A/W interface. LB film of single layer of SWCNTs deposited onto chemically treated silicon (Si/SiO_2) substrates is characterized by Raman spectroscopy. We transferred the LB films on conducting indium tin oxide deposited glass (ITO) substrates at different target surface pressures and characterized the films using an atomic force microscope (AFM) in spreading resistance imaging (SRI) mode. The films deposited at target surface pressure ≥ 2 mN/m shows SWCNTs forming a supramolecular donut structure. We obtained a supramolecular assembly of the SWCNTs in the LB films deposited in the liquid–like phase of the LM. The current–voltage (I–V) characteristic reveals metallic nanopores inside the semi–metallic donut. Such surface pressure–induced assemblies of SWCNTs on substrates have not been observed earlier. We have demonstrated that SWCNTs can form interesting mophologies onto solid substrates as a function of target surface pressure of LB deposition.

In chapter 3, we demonstrated a control on the alignment of SWCNTs on the solid substrate during the ultrathin film fabrication by LB technique. During LB deposition if the substrate plane is made parallel or perpendicular to the compression direction, the SWCNTs on the Si/SiO_2 substrates will align with their long axis parallel or perpendicular to the dipping direction, respectively. The LB films with different orientation of SWCNTs are characterized by AFM and I–V measurements. Assuming Poole–Frenkel (P–F) type of conduction, we estimated the relative permittivity for the two different orientations of SWCNTs with respect to the applied electric field. In the case of SWCNTs aligned parallel and perpendicular to the electric field, the value of relative permittivity is obtained to be around 39 and 2.4, respectively. We have demonstrated the methane (CH_4) gas sensing capability of the aligned SWCNTs in the LB film using an in–house assembled Kelvin Probe (KP) based gas sensor characterization setup. The KP technique measures the change in work function in terms of change in contact potential difference between the oscillating gold grid and the sensing layer. The sensing capability of the aligned SWCNTs in single layer of LB film of SWCNTs is compared with that of randomly oriented SWCNTs in the film grown by drop cast method. We found that the gas sensing capability of the LB film of SWCNTs is more efficient than that of the drop cast film. Furthermore, the sensitivity of the LB film is higher in humid condition as compared to that of dry environment. Such a behavior makes LB films of SWCNTs more viable for CH_4 gas sensing in the normal atmospheric condition which in general possesses finite humidity.

The functionalized SWCNTs offers not only the ease of device processability but also functional layer for attracting specific analytes in the sensing application. In chapter 4, we report formation of a stable Langmiur film (LF) of octadecylamine functionalized SWCNTs (ODA–SWCNTs). The LB films of ODA–SWCNTs are fabricated onto the quartz crystal wafers of a quartz crystal microbalance and are employed for sensing the biological analytes *viz.* L-aspartic (L–asp) acid and bovine serum albumin (BSA) protein. The sensing performance of the LB films of ODA–SWCNTs is compared with that of thin film of randomly oriented ODA–SWCNTs obtained through spin coating technique. The sensitivity towards the analytes using LB film is found to be far better than that of spin coated film of ODA–SWCNTs. The highly oriented ODA–SWCNTs in the LB films may create large surface density of adsorption sites which support the further growth of the nucleation sites into bigger domains. This in turn yield better performance and high sensitivity of the analytes by the LB films. The surface morphology study also reveals large number of adsorbed domains of L–asp acid and BSA protein by the LB film than that of spin coated film of ODA–SWCNTs.

The LM and LB films of cationic surfactants is very interesting not only for understanding the fundamental science involving the molecular interactions at the interfaces but also its application for attracting and trapping of anionic analytes during sensing process. In chapter 5, we report our studies on the LM and LB films of the cationic surfactants. We formed the LB films of dioctadecyl ammonium bromide (DOAB) and studied the DNA sensing application. The lowest detectable concentration of DNA in the liquid is found to be 20 fM. The kinetic study indicate the characteristic time for DNA adsorption over the LB film of DOAB is $\sim$ 162 seconds. The effect of polyethylene glycol functionalized SWCNTs (PEG–SWCNTs) in the aqueous subphase on the

LM of dioctadecylamine (DODA) is studied as the function of pH of the subphase. We found that the association of PEG–SWCNTs with LM of DODA is better at the ultrapure water subphase than that compared with aqueous basic subphase. We formed the LB film of DODA and DODA/PEG–SWCNTs at $\pi_t = 10$ mN/m from the ultrapure water subphase and characterize it using field emission scanning electron microscope (FESEM). The FESEM image clearly shows the formation of liquid condensed domains in form of small domains and big dendritic domains. The LB film of DODA/PEG–SWCNTs also reveals the presence of nanotubes on the monolayer matrix of DODA. The DNA sensing studies of LB films of DODA/PEG–SWCNTs indicate that the lowest detectable concentration of DNA in aqueous medium is $\sim$3 fM which is far lower than that of the LB film of DOAB. The piezoresponse signal obtained from CNTs incorporated film are much stable than that of pure organic surfactant layer. The presence of SWCNTs in the functional layer for sensing may provide mechanical strength to the film against any dissolution of the surfactant in the fluid medium. Our studies indicate that presence of SWCNTs in the functional layer for sensing can provide several advantages including sensitivity, stability and reproducibility.

Graphene is one of the extraordinary carbon based nanomaterials which can be employed for numerous device applications. Graphene can be oraganically functionalized for ease of device processability and dispersion in a host. The carboxylic group functionalized graphene (G–COOH) is one of the important chemically modified graphene which has a potential for chemical and biological sensing. The –COOH group of the graphene can form complex with different proteins and biologically relevant molecules. In chapter 6, we discuss the formation and characterization of LF and LB films of G–COOH. The LF of G–COOH at the A/W interface is found to be very stable and reversible. The urea in aqueous subphase is found to interact strongly with LF of G–COOH at the A/W interface indicating that the LB film of G–COOH can be employed as functional layer for urea sensing. The functional layers of G–COOH were formed over the quartz crystal wafers by LB and spin coating techniques, and employed for sensing of urea in aqueous medium. The response is found to be linear in the given concentration range. The lowest detectable concentration of urea in water by LB film was found to be very low (8.32 μM). The sensing performance of LB film of G–COOH is found to be better than that of spin coated film of G–COOH. The detection of urea in milk sample using the functional layers of G–COOH is also studied. The study on sensing of urea in milk sample indicate that the LB film of G–COOH can be employed for sensing urea even in the presence of differnt other species in the aqueous medium.

7.2 Future Scope

In our studies, we found that SWCNTs can form interesting morphologies onto solid substrates as a function of target surface pressure (π_t) of LB deposition. Future works will deal with studying the role of external parameters like temperature, nature of substrates and role of functional groups on CNTs for controlling the assembly of SWCNTs and functionalized CNTs on the substrates. The formation of donut structure of SWCNTs onto ITO substrate can be employed for the development of selective trapping of analytes. It can also be used for the fabrication of array of nanoelectrodes. We have demonstrated the methane (CH_4) gas sensing capability of the ultrathin films of SWCNTs deposited by LB technique. Interestingly, the sensing performance improves in the presence of humidity even in the room temperature. This study can be conceived for the development of professional methane gas sensor. The LF of octadecylamine functionalized SWCNTs (ODA–SWCNTs) at the A/W interface is found to be stable and therefore, it was possible to form a well organized LB films onto solid substrates. It will be interesting to study the morphology of the LB film of ODA–SWCNTs onto different substrates. The LB films of ODA–SWCNTs showed a strong affinity towards the biologically relevant molecules *e.g* L–asp acid and BSA protein. The LB film of ODA–SWCNTs can be employed for the development of specific biosensors which may find large biomedical application. We studied the surface behavior of a unique nanocomposite comprised of cationic surfactant and PEG–SWCNTs. The LB film of such nanocomposites can be employed for the DNA sensing and the performance of the device can be studied under the influence of various physical parameters. The sensing of other analytes can be studied using the LB film of nanocomposites of the surfactant and PEG–SWCNTs. The the LF of functionalized graphene (G–COOH) at the A/W interface is found to be stable. The surface behavior of G–COOH can be studied as a function of temperature, pH and ion contents in the subphase. The urea sensing of LB film of G–COOH indicates that such functional layers can be employed for immobilization of ligands for a specific biosensing. The sensors developed using LB film of carbon nanomaterials may be easily processable, room temperature operatable, stable and of low cost.

Appendix A

Dimensions of BSA protein

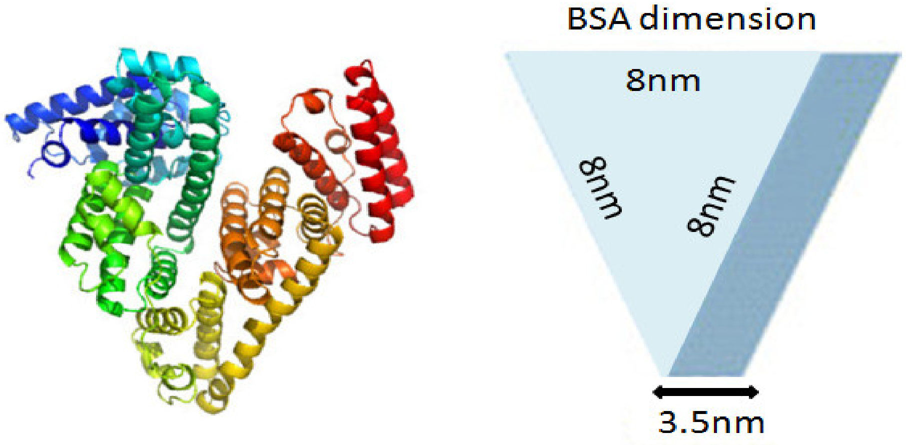

Figure A.1: Dimensions of BSA protein [184].

Bibliography

[1] R. K. Gupta and M. V., *Molecular Interactions at Interfaces* (INTECH Open Access Publisher, 2012).

[2] Glocker and I. Shah, editors, *Handbook of Thin Film Process Technology, Vol.1 & 2* (Institute of Physics, 2002).

[3] S. Mohan, *Proc. Advanced Course on Thin Film Processing* (Instrumentation and services unit, I.I.Sc. Banglore, India, 1994).

[4] H. Bach and D. Krause, editors, *Thin Films on Glass (Schott Series on Glass and Glass Ceramics)* (Springer, 2010).

[5] C. W. Tang and S. A. VanSlyke, Applied Physics Letters **51** (1987).

[6] J. Cui, Q. Huang, Q. Wang, and T. J. Marks, Langmuir **17**, 2051 (2001).

[7] S. Miao, H. Leeman, S. De Feyter, and R. A. Schoonheydt, Chemistry - A European Journal **16**, 2461 (2010).

[8] Y. Hirano, A. Maio, and Y. Ozaki, Langmuir **24**, 3317 (2008).

[9] M. Hitrik, V. Gutkin, O. Lev, and D. Mandler, Langmuir **27**, 11889 (2011).

[10] K. Rajesh, K. Rajendra, and T. P. Radhakrishnan, The Journal of Physical Chemistry B **114**, 849 (2010).

[11] A. Ghosh, S. Choudhury, and A. Das, Chemistry – An Asian Journal **5**, 352 (2010).

[12] P. Sun *et al.*, Langmuir **21**, 3413 (2005).

[13] A. A.-M. Santafé, L. J. Blum, C. A. Marquette, and A. P. Girard-Egrot, Langmuir **26**, 2160 (2010).

[14] S. Choudhury, C. A. Betty, K. G. Girija, and S. K. Kulshreshtha, Applied Physics Letters **89**, (2006).

[15] D. R. Talham, Chemical Reviews **104**, 5479 (2004).

[16] J. Yoshida *et al.*, Langmuir **22**, 9591 (2006).

[17] J. N. Israelachvili, *Intermolecular and Surface Forces, Revised Third Edition* (Academic Press, 2011).

[18] D. F. Evans and H. Wennerström, *The Colloidal Domain*, 2^{nd} ed. (Wiley-VCH, 1999).

[19] K. Holmberg, B. Jönsson, B. Kronberg, and B. Lindman, *Surfactants and Polymers in Aqueous Solution*, 2^{nd} ed. (Wiley, 2002).

[20] J. N. Israelachvili, *Intermolecular and Surface Forces : With Applications to Colloidal and Biological Systems*, Seventh printing ed. (Academic Press, 1991).

[21] G. L. Gaines, *Insoluble Monolayers at Liquid-gas Interfaces*, 1^{st} ed. (John Wiley & Sons Inc, 1966).

[22] S. Kundu and D. Langevin, Colloids and Surfaces A: Physicochemical and Engineering Aspects **325**, 81 (2008).

[23] R. E. Heikkila, D. W. Deamer, and D. G. Cornwell, Journal of Lipid Research **11**, 195 (1970).

[24] G. Gompper, M. Schick, C. Domb, and J. L. Lebowitz, editors, *Self-Assembling Amphiphilic Systems, Volume 16 (Phase Transitions and Critical Phenomena)* (Academic Press, 1994).

[25] H. Mohwald, Annual Review of Physical Chemistry **41**, 441 (1990).

[26] H. M. McConnell, Annual Review of Physical Chemistry **42**, 171 (1991).

[27] R. Seoane *et al.*, The Journal of Physical Chemistry B **104**, 7735 (2000).

[28] A. Datta, M. K. Sanyal, A. Dhanabalan, and S. S. Major, The Journal of Physical Chemistry B **101**, 9280 (1997).

[29] M.-J. Hwang and K. Kim, Langmuir **15**, 3563 (1999).

[30] S. Siegel, D. Hoenig, D. Vollhardt, and D. Moebius, The Journal of Physical Chemistry **96**, 8157 (1992).

[31] C. McFate, D. Ward, and J. O. III, Langmuir **9**, 1036 (1993).

[32] K. S. Birdi and D. T. Vu, Langmuir **10**, 623 (1994).

[33] K. B. Blodgett, Journal of the American Chemical Society **57**, 1007 (1935).

[34] M. C. Petty, *Langmuir-Blodgett Films: An Introduction*, 1^{st} ed. (Cambridge University Press, 1996).

[35] G. Roberts, editor, *Langmuir-Blodgett Films* (Springer, 1990).

[36] I. Langmuir, Trans. Faraday Soc. **15**, 62 (1920).

[37] I. Langmuir, The Journal of Chemical Physics **1** (1933).

[38] J. Zasadzinski, R. Viswanathan, L. Madsen, J. Garnaes, and D. Schwartz, Science **263**, 1726 (1994).

[39] D. K. Schwartz, Surface Science Reports **27**, 245 (1997).

[40] W. Reichert, C. Bruckner, and J. Joseph, Thin Solid Films **152**, 345 (1987).

[41] J.-i. Anzai, S. Lee, and T. Osa, Bull. Chem. Soc. Jpn. **62**, 3018 (1989).

[42] Y. Okahata, T. Tsuruta, K. Ijiro, and K. Ariga, Langmuir **4**, 1373 (1988).

[43] A. Arya, U. Krull, M. Thompson, and H. Wong, Analytica Chimica Acta **173**, 331 (1985).

[44] M. Sriyudthsak, H. Yamagishi, and T. Moriizumi, Thin Solid Films **160**, 463 (1988).

[45] D. Zhu, M. Petty, H. Ancelin, and J. Yarwood, Thin Solid Films **176**, 151 (1989).

[46] S. Lee, J. ichi Anzai, and T. Osa, Sensors and Actuators B: Chemical **12**, 153 (1993).

[47] M. Aizawa, M. Matsuzawa, and H. Shinohara, Thin Solid Films **160**, 477 (1988).

[48] J. ichi Anzai, J. ya Hashimoto, T. OSA, and T. Matsuo, Analytical Sciences **4**, 247 (1988).

[49] D. Grieshaber, R. MacKenzie, J. Vörös, and E. Reimhult, Sensors (Basel) **8**, 1400 (2008).

[50] A. G. Emslie, F. T. Bonner, and L. G. Peck, Journal of Applied Physics **29**, 858 (1958).

[51] T. Kato, Science **295**, 2414 (2002).

[52] T. Kato, N. Mizoshita, and K. Kishimoto, Angewandte Chemie International Edition **45**, 38 (2006).

[53] J. Peng, G. Barnes, and I. Gentle, Advances in Colloid and Interface Science **91**, 163 (2001).

[54] T. Kawai, J. Umemura, and T. Takenaka, Langmuir **5**, 1378 (1989).

[55] G. Veale, I. Girling, and I. Peterson, Thin Solid Films **127**, 293 (1985).

[56] S. Ye, H. Noda, S. Morita, K. Uosaki, and M. Osawa, Langmuir **19**, 2238 (2003).

[57] F. Kimura, J. Umemura, and T. Takenaka, Langmuir **2**, 96 (1986).

[58] S. Ye, H. Noda, T. Nishida, S. Morita, and M. Osawa, Langmuir **20**, 357 (2004).

[59] K. Birdi, *Lipid and Biopolymer Monolayers at Liquid Interfaces*, 1^{st} ed. (Springer, 1989).

[60] I. Fujiwara, M. Ohnishi, and J. Seto, Langmuir **8**, 2219 (1992).

[61] Y. Yasuda *et al.*, Bioelectrochemistry and Bioenergetics **34**, 135 (1994).

[62] B.-K. Oh *et al.*, Materials Science and Engineering: C **24**, 65 (2004).

[63] R. K. Gupta and K. A. Suresh, Eur. Phys. J. E **14**, 35 (2004).

[64] Z. Matharu *et al.*, Langmuir **23**, 13188 (2007).

[65] H. Ohnuki, R. Honjo, H. Endo, T. Imakubo, and M. Izumi, Thin Solid Films **518**, 596 (2009).

[66] T. Michinobu *et al.*, Journal of the American Chemical Society **128**, 14478 (2006).

[67] M. Achermann, M. A. Petruska, S. A. Crooker, and V. I. Klimov, The Journal of Physical Chemistry B **107**, 13782 (2003).

[68] B. O. Dabbousi, C. B. Murray, M. F. Rubner, and M. G. Bawendi, Chemistry of Materials **6**, 216 (1994).

[69] A. Milekhin, M. Friedrich, D. Zahn, L. Sveshnikova, and S. Repinsky, Applied Physics A **69**, 97 (1999).

[70] Y. Guo, J. Wu, and Y. Zhang, Chemical Physics Letters **362**, 314 (2002).

[71] V. Krstic, G. S. Duesberg, J. Muster, M. Burghard, and S. Roth, Chemistry of Materials **10**, 2338 (1998).

[72] Y. Kim *et al.*, Japanese Journal of Applied Physics **42**, 7629 (2003).

[73] D. Li, M. B. Muller, S. Gilje, R. B. Kaner, and G. G. Wallace, Nat Nano **3**, 101 (2008).

[74] Q. Zheng *et al.*, ACS Nano **5**, 6039 (2011).

[75] J. Kim *et al.*, Journal of the American Chemical Society **132**, 8180 (2010).

[76] G. B. Sukhorukov, M. M. Montrel, A. I. Petrov, L. I. Shabarchina, and B. I. Sukhorukov, Biosensors and Bioelectronics **11**, 913 (1996).

[77] S. Dai, X. Zhang, Z. Du, and H. Dang, Materials Letters **59**, 423 (2005).

[78] Y. Okahata, T. Kobayashi, and K. Tanaka, Langmuir **12**, 1326 (1996).

[79] J. Kim and T. M. Swager, Nature **411**, 1030 (2001).

[80] F. Monroy, H. M. Hilles, F. Ortega, and R. G. Rubio, Phys. Rev. Lett. **91**, 268302 (2003).

[81] J. Chen *et al.*, Science **282**, 95 (1998).

[82] M. A. Hamon *et al.*, Advanced Materials **11**, 834 (1999).

[83] M. S. Dresselhaus, G. Dresselhaus, P. Avouris, and R. Smalley, editors, *Carbon Nanotubes: Synthesis, Structure, Properties and Applications* (Springer, 2001).

[84] C. P. Collier, R. J. Saykally, J. J. Shiang, S. E. Henrichs, and J. R. Heath, Science **277**, 1978 (1997).

[85] B. Lin *et al.*, Thin Solid Films **515**, 5669 (2007).

[86] J. R. Heath, C. M. Knobler, and D. V. Leff, The Journal of Physical Chemistry B **101**, 189 (1997).

[87] G. Markovich, C. P. Collier, and J. R. Heath, Phys. Rev. Lett. **80**, 3807 (1998).

[88] R. P. Sear, S.-W. Chung, G. Markovich, W. M. Gelbart, and J. R. Heath, Phys. Rev. E **59**, R6255 (1999).

[89] B. Zhao, H. Hu, S. K. Mandal, and R. C. Haddon, Chemistry of Materials **17**, 3235 (2005).

[90] E. B. Malarkey, R. C. Reyes, B. Zhao, R. C. Haddon, and V. Parpura, Nano Letters **8**, 3538 (2008).

[91] K. S. Novoselov *et al.*, Nature **490**, 192 (2012).

[92] F. Bonaccorso, Z. Sun, T. Hasan, and A. C. Ferrari, Nat Photon **4**, 611 (2010).

[93] Y. Dan, Y. Lu, N. J. Kybert, Z. Luo, and A. T. C. Johnson, Nano Letters **9**, 1472 (2009).

[94] S. Borini *et al.*, ACS Nano **7**, 11166 (2013).

[95] I.-Y. Jeon *et al.*, Proceedings of the National Academy of Sciences **109**, 5588 (2012).

[96] V. A. Chhabra, A. Deep, R. Kaur, and R. Kumar, International Journal for Science and Emerging Technologies with Latest Trends **4**, 13 (2012).

[97] C.-S. Cho, I.-K. Park, J.-W. Nah, and T. Akaike, Macromolecular Research **11**, 2 (2013).

[98] P. M. Ferreira, A. B. Timmons, M. C. Neves, P. Dynarowicz, and T. Trindade, Thin Solid Films **389**, 272 (2001).

[99] F. Babudri *et al.*, Materials Science and Engineering: C **22**, 445 (2002).

[100] G. Binnig and H. Rohrer, IBM J. Res. Dev. **44**, 279 (2000).

[101] G. Binnig, C. F. Quate, and C. Gerber, Phys. Rev. Lett. **56**, 930 (1986).

[102] P. Eyben *et al.*, Journal of Vacuum Science & Technology B **20** (2002).

[103] G. Lawes, *Scanning Electron Microscopy and X-Ray Microanalysis (Analytical Chemistry by Open Learning)*, 1^{st} ed. (Wiley, 1987).

[104] P. R. G. J. A. D. Haseth, *Fourier Transform Infrared Spectrometry* (Wiley-Interscience (1986-03-28), 1656).

[105] L. Kavan *et al.*, The Journal of Physical Chemistry B **105**, 10764 (2001).

[106] L. Alvarez *et al.*, Chemical Physics Letters **316**, 186 (2000).

[107] Y. Saito, T. Yoshikawa, S. Bandow, M. Tomita, and T. Hayashi, Phys. Rev. B **48**, 1907 (1993).

[108] O. Zhou *et al.*, Science **263**, 1744 (1994).

[109] D. Reznik, C. H. Olk, D. A. Neumann, and J. R. D. Copley, Phys. Rev. B **52**, 116 (1995).

[110] J. Curie and P. Curie, Rendu **91**, 294 (1880).

[111] G. Sauerbrey, J. Physik **155**, 206 (1959).

[112] T. T. Nguyen, S. U. Nguyen, D. T. Phuong, D. C. Nguyen, and A. T. Mai, Advances in Natural Sciences: Nanoscience and Nanotechnology **2**, 035015 (2011).

[113] Y. Yan, M. Chan-Park, and Q. Zhang, Small **3**, 24 (2007).

[114] Z. Liu, L. Jiao, Y. Yao, X. Xian, and J. Zhang, Advanced Materials **22**, 2285 (2010).

[115] L. Jia, Y. Zhang, J. Li, C. You, and E. Xie, Journal of Applied Physics **104** (2008).

[116] Y. Guo *et al.*, Physica B: Condensed Matter **323**, 235 (2002).

[117] C. Venet *et al.*, Colloids and Surfaces A: Physicochemical and Engineering Aspects **354**, 113 (2010).

[118] J. Kong *et al.*, Science **287**, 622 (2000).

[119] M. Bienfait, B. Asmussen, M. Johnson, and P. Zeppenfeld, Surface Science **460**, 243 (2000).

[120] K. G. Ong, K. Zeng, and C. A. Grimes, IEEE Sensors Journal **2**, 82 (2002).

[121] S. Rumyantsev, G. Liu, M. S. Shur, R. A. Potyrailo, and A. A. Balandin, Nano Letters **12**, 2294 (2012).

[122] J. D. Fowler *et al.*, ACS Nano **3**, 301 (2009).

[123] Y. Yao, X. Chen, H. Guo, and Z. Wu, Applied Surface Science **257**, 7778 (2011).

[124] D.-H. Fan, D.-J. Niu, and K.-J. Huang, Sensors and Actuators B: Chemical , (2010).

[125] R. Saito, *Physical Properties of Carbon Nanotubes* (Imperial College Press, 1998).

[126] C. Dekker, Physics Today **52**, 22 (1999).

[127] S. Iijima, Nature **354**, 56 (1991).

[128] H. Park *et al.*, Nat Nano **7**, 787 (2012).

[129] M. Engel *et al.*, ACS Nano **2**, 2445 (2008).

[130] G. S. Tulevski *et al.*, Journal of the American Chemical Society **129**, 11964 (2007).

[131] C. Klinke, J. B. Hannon, A. Afzali, and P. Avouris, Nano Letters **6**, 906 (2006).

[132] A. Ulman, *An Introduction to Ultrathin Organic Films: From Langmuir–Blodgett to Self–Assembly*, 1^{st} ed. (Academic Press, 1991).

[133] M. Li, A. A. Acero, Z. Huang, and S. A. Rice, Nature **367**, 151 (1994).

[134] Y. Tabe *et al.*, The Journal of Physical Chemistry B **106**, 12089 (2002).

[135] A. V. Tkachenko and Y. Rabin, Phys. Rev. Lett. **76**, 2527 (1996).

[136] D. Langevin and F. Monroy, Current Opinion in Colloid & Interface Science **15**, 283 (2010).

[137] F. Monroy, F. Ortega, R. G. Rubio, and M. G. Velarde, Advances in colloid and interface science **134-135**, 175—189 (2007).

[138] L. Feng, H. Li, F. Li, Z. Shi, and Z. Gu, Carbon **41**, 2385 (2003).

[139] X. Li *et al.*, Journal of the American Chemical Society **129**, 4890 (2007).

[140] M. K. Massey, C. Pearson, D. A. Zeze, B. G. Mendis, and M. C. Petty, Carbon **49**, 2424 (2011).

[141] K. D. Ausman, R. Piner, O. Lourie, R. S. Ruoff, and M. Korobov, The Journal of Physical Chemistry B **104**, 8911 (2000).

[142] X. Wang, X. Ma, and D. Zang, Soft Matter **9**, 443 (2013).

[143] R. K. Gupta and V. Manjuladevi, Israel Journal of Chemistry **52**, 809 (2012).

[144] J. W. Ding *et al.*, Journal of Physics: Condensed Matter **15**, L439 (2003).

[145] R. Martel, H. R. Shea, and P. Avouris, Nature **398**, 299 (1999).

[146] A. L. Parga and R. Miranda, *Scanning Tunneling Spectroscopy* (Springer Netherlands, Dordrecht, 2012).

[147] G. Che, B. B. Lakshmi, E. R. Fisher, and C. R. Martin, Nature **393**, 346 (1998).

[148] Q. H. Wang *et al.*, Applied Physics Letters **72** (1998).

[149] E. S. Snow, J. P. Novak, P. M. Campbell, and D. Park, Applied Physics Letters **82** (2003).

[150] C. Liu *et al.*, Science **286**, 1127 (1999).

[151] Y. Wei *et al.*, Applied Physics Letters **89**, 063101 (2006).

[152] H. Dai, Accounts of Chemical Research **35**, 1035 (2002).

[153] N. Sinha, J. Ma, and J. T. W. Yeow, Journal of Nanoscience and Nanotechnology **6**, 573 (2006).

[154] P. Bondavalli, P. Legagneux, and D. Pribat, Sensors and Actuators B: Chemical **140**, 304 (2009).

[155] Q. Cao and J. A. Rogers, Advanced Materials **21**, 29 (2009).

[156] B. Lewis and G. von Elbe, *Combustion, Flames and Explosions of Gases*, 1^{st} ed. (ACADEMIC PRESS INC, 1951).

[157] H. Tai, T. Yoshino, and H. Tanaka, Opt. Lett. **12**, 437 (1987).

[158] E. Kress-Rogers, *Handbook of Biosensors and Electronic Noses: Medicine, Food, and the Environment*, 1^{st} ed. (CRC Press, 1996).

[159] V. Pentyala, P. Davydovskaya, R. Pohle, G. Urban, and O. Yurchenko, Procedia Engineering **87**, 1071 (2014).

[160] P. Davydovskaya, R. Pohle, A. Tawil, and M. Fleischer, Sensors and Actuators B: Chemical **187**, 142 (2013).

[161] P. Liu *et al.*, Nano Letters **8**, 647 (2008), PMID: 18225940.

[162] J. Oh, S. Roh, W. Yi, H. Lee, and J. Yoo, Journal of Vacuum Science & Technology B **22**, 1416 (2004).

[163] A. Zahab, L. Spina, P. Poncharal, and C. Marlière, Phys. Rev. B **62**, 10000 (2000).

[164] R. Pati, Y. Zhang, S. K. Nayak, and P. M. Ajayan, Applied Physics Letters **81**, 2638 (2002).

[165] R. Roy, M. P. Chowdhury, and A. Pal, Vacuum **77**, 223 (2005).

[166] H. Dai, Surface Science **500**, 218 (2002).

[167] A. C. Dillon *et al.*, Nature **386**, 377 (1997).

[168] P. J. F. Harris, *Carbon Nanotubes and Related Structures* (Cambridge University Press, 1999), Cambridge Books Online.

[169] U. Yogeswaran and S. Chen, Analytical Letters **41**, 210 (2008).

[170] C. B. Jacobs, M. J. Peairs, and B. J. Venton, Analytica Chimica Acta **662**, 105 (2010).

[171] S. C. Tsang *et al.*, J. Chem. Soc., Chem. Commun. , 1803 (1995).

[172] B. Pérez-López and A. Merkoçi, Microchimica Acta **179**, 1 (2012).

[173] C. Nie *et al.*, Journal of Electroanalytical Chemistry **666**, 85 (2012).

[174] X. Dong, X. Lu, K. Zhang, and Y. Zhang, Microchimica Acta **180**, 101 (2012).

[175] C. Iancu *et al.*, Int J Nanomedicine **6**, 129 (2011).

[176] P. L. Konash and G. J. Bastiaans, Analytical Chemistry **52**, 1929 (1980).

[177] H.-H. Lu, Y. K. Rao, T.-Z. Wu, and Y.-M. Tzeng, Sensors and Actuators B: Chemical **137**, 741 (2009).

[178] A. Janshoff, H.-J. Galla, and C. Steinem, Angewandte Chemie International Edition **39**, 4004 (2000).

[179] W. Pang *et al.*, Lab Chip **12**, 29 (2012).

[180] E. D. Kaufman *et al.*, Langmuir **23**, 6053 (2007).

[181] P. G. Su and Y. P. Chang, Sensors and Actuators B: Chemical **129**, 915 (2008).

[182] L. Piao, Q. Liu, and Y. Li, The Journal of Physical Chemistry C **116**, 1724 (2012).

[183] R. J. Chen *et al.*, Journal of the American Chemical Society **126**, 1563 (2004).

[184] S. Yu *et al.*, Nanoscale **8**, 14393 (2016).

[185] V. Devanarayanan *et al.*, Journal of Molecular Structure **1103**, 281 (2016).

[186] R. Bandyopadhyaya, E. Nativ-Roth, O. Regev, and R. Yerushalmi-Rozen, Nano Letters **2**, 25 (2002).

[187] M. F. Islam, E. Rojas, D. M. Bergey, A. T. Johnson, and A. G. Yodh, Nano Letters **3**, 269 (2003).

[188] N. W. S. Kam, M. O'Connell, J. A. Wisdom, and H. Dai, Proceedings of the National Academy of Sciences of the United States of America **102**, 11600 (2005).

[189] A. Hirsch and O. Vostrowsky, *Functional Molecular Nanostructures* (Springer Berlin Heidelberg, Berlin, Heidelberg, 2005), chap. Functionalization of Carbon Nanotubes, pp. 193–237.

[190] H. Kuzmany *et al.*, Synthetic Metals **141**, 113 (2004).

[191] N. W. S. Kam and H. Dai, Journal of the American Chemical Society **127**, 6021 (2005).

[192] D. E. Hill, Y. Lin, A. M. Rao, L. F. Allard, and Y.-P. Sun, Macromolecules **35**, 9466 (2002).

[193] K. Fu *et al.*, Journal of Nanoscience and Nanotechnology **2**, 457 (2002).

[194] M. Zheng *et al.*, Nat Mater **2**, 338 (2003).

[195] K. A. S. Fernando, Y. Lin, and Y.-P. Sun, Langmuir **20**, 4777 (2004).

[196] J. Gao *et al.*, Journal of the American Chemical Society **128**, 7492 (2006).

[197] H.-J. Jin, H. J. Choi, S. H. Yoon, S. J. Myung, and S. E. Shim, Chemistry of Materials **17**, 4034 (2005).

[198] W.-F. Chen, J.-S. Wu, and P.-L. Kuo, Chemistry of Materials **20**, 5756 (2008).

[199] M. Alvaro *et al.*, The Journal of Physical Chemistry B **108**, 12691 (2004).

[200] N. Nakayama-Ratchford, S. Bangsaruntip, X. Sun, K. Welsher, and H. Dai, Journal of the American Chemical Society **129**, 2448 (2007).

[201] K. Welsher, Z. Liu, D. Daranciang, and H. Dai, Nano Letters **8**, 586 (2008).

[202] M. L. Schipper *et al.*, Nat Nano **3**, 216 (2008).

[203] J. M. Harris and R. B. Chess, Nat Rev Drug Discov **2**, 214 (2003).

[204] J. M. Harris, N. E. Martin, and M. Modi, Clinical Pharmacokinetics **40**, 539 (2012).

[205] Z. Liu, J. T. Robinson, X. Sun, and H. Dai, Journal of the American Chemical Society **130**, 10876 (2008).

[206] N. Karousis, N. Tagmatarchis, and D. Tasis, Chemical Reviews **110**, 5366 (2010).

[207] Z. Liu, S. M. Tabakman, Z. Chen, and H. Dai, Nat. Protocols **4**, 1372 (2009).

[208] S. Brahmachari, D. Das, A. Shome, and P. K. Das, Angewandte Chemie International Edition **50**, 11243 (2011).

[209] M. Shim, N. W. S. Kam, R. J. Chen, Y. Li, and H. Dai, Nano Letters **2**, 285 (2002).

[210] M. Bottini, N. Rosato, and N. Bottini, Biomacromolecules **12**, 3381 (2011).

[211] J. E. Riggs, Z. Guo, D. L. Carroll, and Y.-P. Sun, Journal of the American Chemical Society **122**, 5879 (2000).

[212] B. Zhao, H. Hu, A. Yu, D. Perea, and R. C. Haddon, Journal of the American Chemical Society **127**, 8197 (2005).

[213] L. P. Zanello, B. Zhao, H. Hu, and R. C. Haddon, Nano Letters **6**, 562 (2006).

[214] H. Hu, Y. Ni, V. Montana, R. C. Haddon, and V. Parpura, Nano Letters **4**, 507 (2004).

[215] H. Hu *et al.*, The Journal of Physical Chemistry B **109**, 4285 (2005).

[216] Y. Ni *et al.*, Journal of Nanoscience and Nanotechnology **5**, 1707 (2005).

[217] E. B. Malarkey *et al.*, Nano Letters **9**, 264 (2009).

[218] B. Byrne, E. Stack, N. Gilmartin, and R. O'Kennedy, Sensors **9**, 4407 (2009).

[219] M. S. Ozdemir *et al.*, Analytical Chemistry **85**, 4770 (2013).

[220] D.-M. Zhu, , and R. K. Evans, Langmuir **22**, 3735 (2006).

[221] K. Hayakawa, J. Santerre, and J. C. Kwak, Biophysical Chemistry **17**, 175 (1983).

[222] M. Slutsky and L. A. Mirny, Biophysical Journal **87**, 4021 (2004).

[223] C. R. Safinya, Current Opinion in Structural Biology **11**, 440 (2001).

[224] V. Karachevtsev, A. Glamazda, V. Leontiev, O. Lytvyn, and U. Dettlaff-Weglikowska, Chemical Physics Letters **435**, 104 (2007).

[225] Y. Xu *et al.*, The Journal of Physical Chemistry C **111**, 8638 (2007).

[226] Z. Wu, Z. Zhen, J.-H. Jiang, G.-L. Shen, and R.-Q. Yu, Journal of the American Chemical Society **131**, 12325 (2009).

[227] S. Viswanathan, H. Radecka, and J. Radecki, Biosensors and Bioelectronics **24**, 2772 (2009).

[228] Z. Liang *et al.*, International Journal of Molecular Sciences **8**, 705 (2007).

[229] C. Hu *et al.*, The Journal of Physical Chemistry B **109**, 20072 (2005).

[230] M. Dresselhaus, G. Dresselhaus, A. Jorio, A. S. Filho, and R. Saito, Carbon **40**, 2043 (2002).

[231] F. Tuinstra and J. L. Koenig, The Journal of Chemical Physics **53** (1970).

[232] A. Jorio *et al.*, Phys. Rev. Lett. **86**, 1118 (2001).

[233] M. S. Dresselhaus and P. C. Eklund, Advances in Physics **49**, 705 (2000).

[234] K. ichi Iimura, Y. Yamauchi, Y. Tsuchiya, T. Kato, and M. Suzuki, Langmuir **17**, 4602 (2001).

[235] A. Miller and H. Möhwald, The Journal of Chemical Physics **86** (1987).

[236] G. Weidemann and D. Vollhardt, Langmuir **13**, 1623 (1997).

[237] V. Sanz *et al.*, Carbon **49**, 1775 (2011).

[238] J. Rajendra, M. Baxendale, L. G. D. Rap, , and A. Rodger, Journal of the American Chemical Society **126**, 11182 (2004).

[239] A. N. Enyashin, S. Gemming, and G. Seifert, Nanotechnology **18**, 245702 (2007).

[240] H. Gao and Y. Kong, Annual Review of Materials Research **34**, 123 (2004).

[241] A. K. Geim and K. S. Novoselov, Nat Mater **6**, 183 (2007).

[242] R. F. Service, Science **324**, 875 (2009).

[243] A. A. Balandin *et al.*, Nano Letters **8**, 902 (2008).

[244] C. Lee, X. Wei, J. W. Kysar, and J. Hone, Science **321**, 385 (2008).

[245] Y. Yang *et al.*, ACS Applied Materials & Interfaces **5**, 4350 (2013).

[246] B. Wang, D. Su, J. Park, H. Ahn, and G. Wang, Nanoscale Research Letters **7**, 215 (2012).

[247] J. Shen, N. Li, M. Shi, Y. Hu, and M. Ye, Journal of Colloid and Interface Science **348**, 377 (2010).

[248] T. Kuila *et al.*, Progress in Materials Science **57**, 1061 (2012).

[249] Y.-K. Yang *et al.*, J. Mater. Chem. **22**, 5666 (2012).

[250] V. Singh *et al.*, Progress in Materials Science **56**, 1178 (2011).

[251] G. Bharath *et al.*, RSC Adv. **5**, 13392 (2015).

[252] C. G. Salzmann, V. Nicolosi, and M. L. H. Green, J. Mater. Chem. **20**, 314 (2010).

[253] M. J. Ju *et al.*, Energy Environ. Sci. **7**, 1044 (2014).

[254] T. W. Meyer and T. H. Hostetter, New England Journal of Medicine **357**, 1316 (2007).

[255] M. M. Paradkar, R. S. Singhal, and P. R. Kulkarni, International Journal of Dairy Technology **53**, 87 (2000).

[256] U. Trivedi *et al.*, Sensors and Actuators B: Chemical **140**, 260 (2009).

[257] K. M. Khan, H. Krishna, S. K. Majumder, and P. K. Gupta, Food Analytical Methods **8**, 93 (2015).

[258] V. Kumar *et al.*, RSC Adv. **5**, 13278 (2015).

[259] R. Verma and B. D. Gupta, Analyst **139**, 1449 (2014).

[260] C. M. Willemse, K. Tlhomelang, N. Jahed, P. G. Baker, and E. I. Iwuoha, Sensors (Basel) **11**, 3970 (2011).

[261] E. Dervishi *et al.*, Chem. Commun. **27**, 4061 (2009).

List of Publications and Presentations

International Journals:

- *"Measurement of optical anisotropy in ultrathin films using surface plasmon resonance"* Devanarayanan VP, Manjuladevi V., **Monika Poonia**, RK Gupta, SK Gupta, and J. Akhtar, Journal of Molecular Structure (Elsevier), **1103** (2016) 281.
- *"Ultrathin films of Single–Walled Carbon nanotubes: A potential methane gas sensor"* **Monika Poonia**, V. Manjuladevi, R. K. Gupta, S. K. Gupta, J. Singh, P. B. Agarwal, and J. Akhtar, Sci. Adv. Mater., (American Scientific Publishers), **7** (2015) 455.
- *"Supramolecular assembly of single–walled carbon nanotubes at air–solid interface"* **Monika Poonia**, R. K. Gupta, V. Manjuladevi, S. K. Gupta, and J. Akhtar, J. Nanoparticle Res. (Springer), **16** (2014) 2572.
- *"Studies on adsorption of DNA on functional ultrathin films of cationic surfactant"* **Monika Poonia**, Anagh Pathak, V. Manjuladevi, R. K. Gupta, Ind. J. Mat. Sci. (Hindawi), **2014** (2014) 502429.
- *"Sensing of urea in milk by Langmuir–Blodgett film of carboxylated graphene"* **Monika Poonia**, V. Manjuladevi, R. K. Gupta, (in communication)
- *"Interaction of PEG–SWCNTs with cationic surfactants at air–water and air–solid interfaces"* **Monika Poonia**, V. Manjuladevi, R. K. Gupta, (in communication)

Conference proceedings in International Journals:

- *"Interaction of bovine serum albumin protein with self assembled monolayer of mercaptoundecanoic acid"* **Monika Poonia**, Hitesh Agarwal, Manjuladevi V., R K Gupta American Institute of Physics Conf. Proc., **1728** (2016) 020145.
- *"Sensing of contaminants in potable water using TiO_2 functional film"* Akshatha N., **Monika Poonia**, R. K. Gupta, V. Manjuladevi, P. Shukla and Rajiv Gupta American Institute of Physics Conf. Proc., **1724** (2016) 020081.
- *"Scanning tunneling spectroscopy of thin films of carbon nanotubes"* **Monika Poonia**, Manjuladevi V, Raj Kumar Gupta, American Institute of Physics Conf. Proc., **1536** (2013) 171.
- *"Interaction of octadecanoic acid monolayer with a divalent Cd^{2+} ion at an air–water interface"* **Monika Poonia**, Keerti Choudhary, Raj Kumar Gupta, Manjuladevi V, Int. J Phy. Math. Sc., **2** (S1) (2012) 36.

List of conferences/schools attended/participated:

- *"International Conference on Condensed Matter and Applied Physics (ICC 2015)"*, October 30–31, 2015, GEC, Bikaner, INDIA.
- *"International Conference on Emerging Technologies: Micro to Nano (ETMN 2015)"*, October 24–25, 2015, Manipal University, Jaipur, INDIA.
- *MNIT–Usask workshop on "Characterization Techniques for the High Performance materials"*, May 25–29, 2015, MNIT, Jaipur, INDIA.
- *"National Conference on Nano and Functional Material–2014"*, November 7–8, 2014, BITS Pilani, INDIA.
- *Workshop and training on "Current Research Trends in Condensed Matter–Material Science"* March 7–8, 2014, BITS Pilani, INDIA.
- *"International Conference on Recent Trends in Applied Physics and Material Science"*, February 01–02, 2013, GEC, Bikaner, INDIA.
- *"National Conference on Condensed Matter Physics"*, February 24–25, 2012, BITS Pilani, INDIA.

Brief Biography of the Supervisor

Dr. R. K. Gupta is Associate Professor in Department of Physics at Birla Institute of Technology & Science Pilani, Pilani Campus. He received his Ph.D. degree from Raman Research Institute, Bengaluru in soft condensed matter physics in the year of 2005. He joined Physics Department of BITS Pilani, Pilani Campus in August 2005. Dr. R. K. Gupta is an experimental soft condensed matter physicist. His research interests are in the area of thin films of mesogenic molecules, carbon based nanomaterials and their nanocomposites.

Currently, his research interests are focused on understanding the change in properties of materials in the ultrathin film regime and its application for device fabrication. He and his team comprising Prof. Manjuladevi V. and Mr. Devanarayanan V. P. in BITS Pilani have developed a low cost portable surface plasmon resonance instrument with the financial support from DST, India. The instrument is ready for any sensing application. He has also successfully completed a research project funded by DST, India. He has published several highly cited research articles in reputed international journals and authored few book chapters in the field of his research interest.

Brief Biography of the Student

Ms. Monika Poonia is a full time research scholar in Department of Physics, BITS Pilani, Pilani campus since August 2011. She obtained her Masters degree in Physics from Banasthali University, Rajasthan in May 2011. She worked as a project trainee for her M.Sc. project in MEMS technology at CSIR-CEERI, Pilani. She is currently pursuing Ph.D. in the area of soft condensed matter physics (experimental). Her research interests include the study of ultrathin films of carbon based nanomaterials. She has published several papers in international journals and few are under review. In addition to this, she has participated and presented her work in several national and international conferences of high repute.